Title

Morphometric disparities between grouped Drosophila olfactory receptor neurons revealed using a novel electron microscopy method

Author

Tsang, Tin Ki

Publication Date

2018

UNIVERSITY OF CALIFORNIA SAN DIEGO

Morphometric disparities between grouped *Drosophila* olfactory receptor neurons revealed using a novel electron microscopy method

A dissertation submitted in partial satisfaction of the
requirements for the degree Doctor of Philosophy

in

Biology

by

Tin Ki Tsang

Committee in charge:

Professor Chih-Ying Su, Chair
Professor Mark H. Ellisman
Professor Jeffry S. Isaacson
Professor Nicholas C. Spitzer
Professor Steven A. Wasserman

2018

The Dissertation of Tin Ki Tsang is approved, and it is acceptable in quality and form for publication on microfilm and electronically:

Chair

University of California San Diego

2018

EPIGRAPH

People have many ways to love each other, some of which can sometimes be called unconventional…until the ways become familiar to everyone. The same applies for neurons. They possess several means to relate with each other, some of which are still unfamiliar to us and some others which are probably unknown.

Henri Korn and Donald S. Faber

TABLE OF CONTENTS

LIST OF FIGURES

LIST OF TABLES

ACKNOWLEDGEMENTS

I thank Chih-Ying for guidance in the projects and for helping me grow into a better scientist. I am truly grateful for the graduate school experience that she provided me because it encouraged me to think critically and gave me the opportunity to work with many phenomenal scientists both within and outside of the Su lab. She has also taught me many invaluable presentation and writing skills that will continuously benefit me. Most of all, I am grateful for the support that she gave me during a very trying time in my personal life. I would also like to thank my committee members, Mark Ellisman, Jeff Isaacson, Nick Spitzer and Steve Wasserman, for useful discussions, scientific insights and generous support throughout my graduate career. In particular, I want to thank Mark for making our electron microscopy collaboration possible. Also, I am grateful to Steve for his kindness, for demonstrating his commitment to teaching, and for his comments on our CryoChem manuscript.

I thank the Su lab members for being my friends and supporting me throughout this journey. Their kindness and support have helped foster a camaraderie amongst us. In particular, I want to thank Ye for working so hard together on our project. In addition, this thesis would not have been possible without the neuronal tracing efforts from our undergraduate students and some of the Su lab members: Szu-Ying Chen, Ben Damasco, Cesar Nava-gonzales, Renny Ng, Vivian Nguyen, Martin Orden, Uma Talagadadivi, Tiffany Tsai, and Edie Zhang. I am deeply grateful to all of their hard work. I also want to thank Jürgen Reingruber for his modeling work presented in Chapter 3 and Varoth Lilascharoen for his help with the dye fill experiment included in Appendix 2.

I thank all the NCMIR members who helped develop the CryoChem method, helped train me to use their equipment and provided me invaluable technical advice.

Particularly, I want to thank Eric for laboring with me on this project for four years and for going through all the ups and downs together. He taught me electron microscopy and the CryoChem project simply would not have been successful without him.

I thank my family for their love and unyielding support throughout my life and for their trust in me. I also want to thank all of my friends, both within and outside UCSD. I would not have been able to persevere without your support and love. Although this acknowledgement shows up later in the context of this thesis, in life, it is friends and family for which I am most thankful. Last but not least, I want to give my deepest gratitude to Chuck Anderson. He taught me what unconditional love is and what a blessing it is to be able to love someone. There is simply nothing more important in life.

Chapter 2, in part, is a reprint of the material as it appears in High-quality ultrastructural preservation using cryofixation for 3D electron microscopy of genetically labeled tissues 2018. Tsang, Tin Ki; Bushong, Eric A.; Boassa, Daniela; Hu, Junru; Romoli, Benedetto; Phan, Sabastien; Dulcis, Davide; Su, Chih-Ying; Ellisman, Mark H., eLife, 7, e35524, 2018. The dissertation author and Eric A. Bushong contributed equally to this paper as primary investigators and authors.

Chapter 2 is used under CC BY 4.0 (https://creativecommons.org/licenses/by/4.0/). The content of Chapter 2 does not include the supplemental materials that are in the eLife publication (https://elifesciences.org/articles/35524).

Chapter 3, in part, has been submitted for publication of the material as it may appear in Asymmetric ephaptic interactions in the initial stage of olfactory processing, 2017. Zhang, Ye; Tsang, Tin Ki; Bushong, Eric A.; Chu, Li-An; Chiang, Ann-Shyn; Ellisman, Mark H.; Reingruber, Jürgen; Su, Chih-Ying, Neuron, 2017. The dissertation author and Ye Zhang contributed equally as primary investigators and authors of this material.

VITA

2013	Bachelor of Science, Arizona State University
2018	Doctor of Philosophy, University of California San Diego

ABSTRACT OF THE DISSERTATION

Morphometric disparities between grouped *Drosophila* olfactory receptor neurons revealed using a novel electron microscopy method

by

Tin Ki Tsang

Doctor of Philosophy in Biology

University of California San Diego, 2018

Professor Chih-Ying Su, Chair

Olfactory receptor neurons (ORNs) housed in the same sensory hair in *Drosophila* can inhibit each other through direct electrical interactions, termed ephaptic interactions. A systematic electrophysiological survey conducted in our lab showed that neighboring ORNs have different electrotonic properties in most sensilla, indicating that ephaptic interactions between these neurons are asymmetric. We hypothesized that the asymmetry arises from the size differences between grouped ORNs. To test the hypothesis, we developed a versatile and widely applicable method, termed CryoChem, to enable genetically labeled cellular structures to be faithfully preserved using cryofixation and then imaged with 3D electron microscopy (EM) techniques. By combining CryoChem and serial block-face scanning electron microscopy (SBEM), we imaged and generated 3D reconstructions of genetically identified ORNs and their neighboring neurons housed in the same sensory hair. Our morphometric analysis reveals that the sizes of neighboring ORNs are indeed different. The physically larger ORN in a pair is the dominant neuron in ephaptic interactions. In addition, our electric circuit model suggests that the size difference between compartmentalized ORNs is a key factor driving the asymmetry observed empirically. The findings of this study provide insight into how morphometric features of a neuron can directly impact circuit interactions in other ephaptic environments.

Chapter 1: Introduction

1.1 Ephaptic interactions in the nervous system

Most efforts aimed at dissecting how neurons communicate with each other have been focused on mechanisms involving chemical synapses and gap junctions. However, uninsulated neurons in close apposition can also communicate via direct electrical interactions (Arvanitaki, 1942; Faber and Korn, 1989; Jasper and Monnier, 1938; Jefferys, 1995; Katz and Schmitt, 1940). Such interactions are termed *ephaptic* (Arvanitaki, 1942). Depending on the direction of the current flow and the relative orientation of the neurons, ephaptic interactions could lead to either excitation or inhibition of the affected neurons (Faber and Korn, 1989; Jefferys, 1995; Korn and Faber, 1980; Ramón and Moore, 1978). There are two general prerequisites for ephaptic interactions to take place. First, uninsulated neuronal processes should be in close proximity to each other, such that current can flow across the membranes of neighboring neurons (Faber and Korn, 1989; Jefferys, 1995). Secondly, the neuronal processes involved in ephaptic interactions should be in an environment of high extracellular resistivity, such that a large portion of current from one neuron is directed into the adjacent neurons instead of into the extracellular space (Faber and Korn, 1989; Jefferys, 1995).

When the concept of ephaptic interactions first emerged in the 1930's (Faber and Korn, 1989; Jasper and Monnier, 1938), most researchers regarded it as an epiphenomenon because it had only been demonstrated in excised neuronal processes that were artificially brought together (Arvanitaki, 1942; Faber and Korn, 1989; Jasper and Monnier, 1938; Katz and Schmitt, 1940). However, evidence of ephaptic interactions has since been discovered in multiple central and peripheral nervous systems. Importantly, the neuronal communication mediated by ephaptic interactions has been implicated to be functionally significant (see below).

In the central nervous system (CNS), ephaptic interactions are best known in the Mauthner (M)-cell of the fish hindbrain (Faber and Korn, 1973, 1989; Furukawa and Furshpan, 1963; Jefferys, 1995; Weiss et al., 2008). The M-cells are a bilaterally symmetrical pair of neurons that integrate visual and auditory inputs to initiate the C-start escape response in teleosts (Weiss et al., 2008). A region of high extracellular resistivity, called the axon cap, is found around the unmyelinated axon hillock of the M-cells (Faber and Korn, 1973, 1989; Furukawa and Furshpan, 1963; Jefferys, 1995; Weiss et al., 2008). The axon cap (≈90 μm in diameter) is formed by a neuropil that consists of unmyelinated axons of inhibitory interneurons (Nakajima, 1974; Triller and Korn, 1981; Zottoli and Faber, 1980). Inward currents originating from the action potentials of the interneurons passively flow out of the unmyelinated axons in the axon cap, thereby hyperpolarizing and inhibiting the M-cell at its axon hillock (Faber and Korn, 1973; Furukawa and Furshpan, 1963; Korn and Faber, 1980; Weiss et al., 2008). It has been proposed that the ephaptic inhibition of the M-cell is important for setting the neuron’s acoustic threshold, and by extension, the threshold for the C-start escape response (Weiss et al., 2008). Evidence of ephaptic interactions has also been reported in other regions of the CNS, including the ephaptic inhibition of Purkinje cells by basket cells in the cerebellum (Blot and Barbour, 2014) and the ephaptic excitation of cones by horizontal cells in the retina (J. Klaassen et al., 2012; Vroman et al., 2013). Beyond the CNS, neurons in the peripheral nervous system can also interact ephaptically. For example, several studies showed that the neighboring color photoreceptors in insects can ephaptically inhibit each other (Horridge et al., 1983; Matić, 1983; Menzel and Blakers, 1976; Shaw, 1975; Yang and Osorio, 1991). Furthermore, a computational model based on the geometric and physiological properties of the mammalian olfactory nerve showed that ephaptic interactions likely exist between the unmyelinated and tightly bundled axons (Bokil et al., 2001).

Neuronal communication via ephaptic interactions likely has several advantages over chemical synaptic transmission. First, it does not require complex developmental processes for forming synaptic connections between neurons. Second, the electrical nature of ephaptic interactions greatly minimizes synaptic delay. Interestingly, when ephaptic interaction is coupled with synaptic transmission (e.g. M-cell (Faber and Korn, 1973, 1989; Furukawa and Furshpan, 1963; Jefferys, 1995; Weiss et al., 2008) and Purkinje cells (Blot and Barbour, 2014)), the temporal features of these two mechanisms complement each other, such that the fast ephaptic effect is sustained by the slower but longer-lasting transmembrane potential change resulted from synaptic transmission (Faber and Korn, 1989). Thirdly, ephaptic interaction is likely less energetically expensive than synaptic transmission, as it does not depend on any active cellular processes.

In principle, ephaptic interactions can occur between any unmyelinated neuronal processes that are packed together in an environment of high extracellular resistivity. Therefore, it is reasonable to predict that ephaptic interactions are more prevalent in the nervous system than currently appreciated. Why does ephaptic interaction remain an underexplored mechanism of neuronal communication? One of the reasons is that neurons that interact ephaptically are often connected via chemical synapses as well (Blot and Barbour, 2014; Chapot et al., 2017; Faber and Korn, 1973, 1989; Furukawa and Furshpan, 1963; J. Klaassen et al., 2012; Jefferys, 1995; Vroman et al., 2013; Weiss et al., 2008), making it challenging to completely isolate the ephaptic effects. It is also experimentally difficult to manipulate ephaptic interactions *in vivo*. Furthermore, the long-established view that chemical synapses and gap junctions are the main mechanisms of neuronal communication may have made the investigation of ephaptic interactions seem irrelevant and outside the purview of a typical neuroscience study.

1.2 Lateral inhibition between grouped olfactory receptor neurons in *Drosophila*

Like many other insects, *Drosophila* olfactory receptor neurons (ORNs) are housed in sensory hairs, or sensilla, that cover the surfaces of the two olfactory organs, antenna and the maxillary palp (Shanbhag et al., 1999, 2000). There are 22 functional types of olfactory sensilla on the antenna and 3 types on the maxillary palp (Benton et al., 2009; de Bruyne et al., 1999, 2001; Couto et al., 2005; Kwon et al., 2010; Lin and Potter, 2015; Prieto-Godino et al., 2017). In each type of sensillum, ORNs are compartmentalized in stereotyped combinations. Even though the stereotyped grouping of ORNs has been known a long time, ORNs were always assumed to function in a cell-autonomous manner. In a set of elegant experiments, *Su et al.* challenged this assumption, showing that grouped ORNs in *Drosophila* can directly inhibit each other (Su et al., 2012). Specifically, transient activation of an ORN can inhibit the chronic spike activity of its neighbor. This direct lateral inhibition was found not only across diverse types of fly sensilla, but also in a mosquito sensillum. *Su et al.* further showed that ephaptic inhibition between ORNs is dose-dependent; stronger activation of one ORN causes an increased inhibition of its neighbor. Critically, lateral inhibition between grouped ORNs can modulate fly's behavioral response towards odor mixture.

Surprisingly, lateral inhibition between ORNs does not depend on a synapse or gap junction (Shanbhag et al., 1999, 2000; Su et al., 2012). Instead, using an electric circuit model of the sensillum (Vermeulen and Rospars, 2004), *Su et al.* showed that lateral inhibition between ORNs is consistent with ephaptic inhibition. The insect sensillum environment favors ephaptic interactions, as the cuticle of the sensillum encapsulates the outer (sensory) dendrites of ORNs in a well-insulated and confined space of high extracellular resistivity (Kramer, 1985; Redkozubov, 1995). Outer dendrites of neighboring olfactory receptor neurons are also uninsulated and housed together in close proximity (Shanbhag et al., 1999, 2000).

In an insect sensillum, the outer dendrites and the soma of ORNs are bathed in the sensillum lymph and the hemolymph, respectively. These two compartments across the epithelium have different ionic compositions (Kaissling and Thorson, 1980; Kaissling, 1986). The large electrochemical gradient between the two compartments results in a significant transepithelial potential, with the sensillum lymph 30 mV more positive relative to the hemolymph (Kaissling and Thorson, 1980; Kaissling, 1986). Unlike a typical neuron, the transduction current of an ORN is primarily driven by the transepithelial potential, instead of the transmembrane ionic gradients (Vermeulen and Rospars, 2004). Based on a published circuit model of the sensillum, ORNs housed in the same sensillum share the same transepithelial potential (Vermeulen and Rospars, 2004). Since grouped ORNs share the same driving force for neuronal activity, *Su et al.* proposed that lateral inhibition results from the current diverted away from an ORN when its neighbor is also active (Su et al., 2012). The level of inhibition of the each ORN depends on both its activity level and the activity level of its neighboring ORNs. Thus, this form of lateral inhibition enables the odor responses of an ORN to be computed in the context of the activity of its neighbor.

Lateral inhibition is considered a hallmark of sensory processing. First proposed by Ernst Mach in the 1860s (Mach, 1865), lateral inhibition serves to compare inputs of different sensory channels in order to enhance the contrast of stimuli (Clarke et al., 2015; Dacey and Packer, 2003; Olsen and Wilson, 2008; Sagi and Hochstein, 1985;

Schnaitmann et al., 2018). Lateral inhibition is widespread amongst sensory systems, including the visual (Hartline et al., 1956; Kramer and Davenport, 2015; Kuffler, 1953), olfactory (Olsen and Wilson, 2008; Su et al., 2009, 2012; Wilson and Mainen, 2006), gustatory (Chapman et al., 1991; Miriyala et al., 2018), and mechanosensory systems (von Békésy, 1967). Lateral inhibition is commonly known to be mediated by the second order neurons. In contrast, the first layer of lateral inhibition in the *Drosophila* peripheral olfactory system is achieved by direct interactions of the primary sensory neurons (Su et al., 2012). Direct lateral inhibition between sensory neurons has also been reported between photoreceptors of the fruit fly, dragonfly, butterfly, locust, and honeybee (Horridge et al., 1983; Matić, 1983; Menzel and Blakers, 1976; Schnaitmann et al., 2018; Shaw, 1975; Yang and Osorio, 1991), and between gustatory receptor neurons in the bumblebee (Miriyala et al., 2018). Interestingly, like in the *Drosophila* ORNs, ephaptic interactions are also thought to mediate the lateral inhibition observed in photoreceptors of dragonfly, butterfly, locust, and honeybee (Menzel and Blakers, 1976; Shaw, 1975; Horridge et al., 1983; Matic, 1983; Yang and Osorio; 1991). Together, the examples of direct lateral inhibition between primary sensory neurons in the three sensory modalities suggest that it may be common for sensory information processing to begin in the first neurons of a sensory system. In addition, these studies show that sensory neurons are not limited to functioning as passive detectors.

On the other hand, lateral inhibition between *Drosophila* ORNs provides a powerful system to study ephaptic interactions because of the diverse genetic tools available in fly and its well-characterized and tractable peripheral olfactory system. In *Drosophila*, approximately 50 types of ORNs are identified (Benton et al., 2009; de Bruyne et al., 1999, 2001; Couto et al., 2005; Kwon et al., 2010; Lin and Potter, 2015; Prieto-Godino et al.,

2017) and the majority of individual ORNs express one odorant receptor that confers ligand binding specificity and defines the odor response profile (de Bruyne et al., 1999; Couto et al., 2005; Hallem and Carlson, 2006; Hallem et al., 2004). Based on the molecular map of the peripheral olfactory system, genetic tools (e.g. promoter-driven GAL4 and LexA lines, knock-in GAL4 lines) have been generated in the majority of ORN types to allow genetic targeting of a specific type of ORN (Benton et al., 2009; Couto et al., 2005; Lin et al., 2015; Silbering et al., 2011). In addition, the odor response profiles of many types of ORN have been characterized (Benton et al., 2009; Dweck et al., 2016, 2015; Hallem and Carlson, 2006; Hallem et al., 2004; Lin and Potter, 2015; Lin et al., 2016; Lucia L. Prieto-Godino et al., 2017; Ronderos et al., 2014; Silbering et al., 2011; Stensmyr et al., 2012; Yao et al., 2005), enabling researchers to choose the appropriate odorants to manipulate the activity level of a specific ORN in a sensillum. Using single sensillum recording, an extracellular electrode can be placed in a sensillum to record the spike activity of each ORN. Interestingly, compartmentalized ORNs exhibit stereotypical differences in extracellular spike amplitudes; the ORNs are named “A”, “B”, “C” or “D” based on their relative spike amplitudes in descending order (de Bruyne et al., 2001; Su et al., 2009). This feature allows the activity of each ORN in the sensillum to be distinguished and identified in the recording. Additionally, the change in the transepithelial potential, a key parameter in measuring the ephaptic inhibition in the sensillum (Vermeulen and Rospars, 2004), can be measured in single sensillum recordings as the change in the local field potential. Lastly, unlike most of the well-studied ephaptically coupled neurons (e.g. M-cell, Purkinje cells and basket cells, cones and horizontal cells), grouped ORNs do not form synaptic connection with each other (Shanbhag et al., 1999, 2000), making it experimentally simpler to study their ephaptic interactions.

It is important to note that lateral inhibition only takes place when both ORNs in the same sensillum are co-activated by an odor mixture (Su et al., 2012). This mutual lateral inhibition then alters the spike activity of each ORN and results in a combinatorial output from the dyad. The key distinction is that this output would be different from one resulting from activating ORNs housed in separate sensilla, since there is no opportunity for interaction in this latter scenario. As mentioned above, the compartmentalization of insect ORNs in the sensilla is highly stereotyped. For example, in *Drosophila*, the ORN that detects apple cider vinegar, a fruit odor, is always grouped with the neuron that responds to CO_2, a volatile emitted by ripe fruit (Barnett, 2003; Faucher et al., 2006; Jones et al., 2007; Kwon et al., 2007; Montet et al., 2014; Semmelhack and Wang, 2009; Suh et al., 2004). This stereotyped pairing rule suggests that it is biologically significant for certain odors to be detected in the context of each other.

Decades of pheromone research in moths shed light onto the organization principle of ORNs in the sensilla. Moths are most attracted to the complete pheromone blend that often consists of not only the attractive major components, but also the antagonistic minor components at a species-specific ratio (Baker, 2008; Baker and Heath, 2005; Cardé and Baker, 1984; Connell, 1985; Cork et al., 1992; Kaissling et al., 1978). The full significance of including antagonistic pheromone components in the blend has not been elaborated. Co-compartmentalized ORNs in moths also exhibit stereotypical differences in extracellular spike amplitudes. Curiously, the large-spike ORN often detects the attractive pheromones, while the small-spike neighbor frequently detects the antagonistic components (Baker, 2008; Cardé and Baker, 1984; Connell, 1985; Cork et al., 1992; Cossé et al., 1998; Kaissling, 1996; Kaissling et al., 1978; Nikonov and Leal, 2002; Witzgall et al., 1999). We notice that this type of neuronal arrangement is not unique to pheromone-sensing sensilla in moths. A growing amount of evidence in *Drosophila* also supports a general pattern that the large-spike ORNs mediate behavior of positive valence, while the small-spike neighbor mediates negative-valence behavior (Chen et al, unpublished data). These observations suggest that the varying ORN spike amplitudes indicate functional differences between the grouped ORNs in a sensillum. Moreover, ephaptic interactions between the grouped ORNs enables each sensillum to serve as a functional unit for processing olfactory information that is relevant to the animal's behavior.

1.3 Findings of the current thesis

Recently, Ye Zhang, a graduate student in our lab, showed that ephaptic interaction is sufficient to drive lateral inhibition between grouped ORNs. She also found that ephaptic interactions in the *Drosophila* olfactory sensilla are asymmetrical and the grouped ORNs of different spike amplitudes are indeed functionally distinct in the context of ephaptic interactions. Specifically, she found that the large-spike "A" neurons in most sensilla types are dominant in ephaptic interactions. However, the mechanistic underpinning of this asymmetry remained elusive.

In the research presented in this thesis, we hypothesized that the asymmetry of ephaptic interactions in a sensillum arises from the distinct electrotonic properties of the grouped ORNs due to their morphometric differences. Our goal was to generate accurate 3D reconstructions of grouped ORNs based on image volumes acquired using serial block-face scanning electron microscopy (SBEM), so as to measure and compare the morphometric features of the neurons. In order to unambiguously assign neuronal identity, we used APEX2 (Lam et al., 2015; Martell et al., 2012), a genetically encoded EM marker, to label one of the ORNs in a sensillum type of interest for 3D reconstructions.

At the time our study started, there was no EM method that could enable genetic labeling of optimally preserved ORNs for SBEM. To overcome this obstacle, we developed a highly versatile and broadly applicable EM method, termed CryoChem (Tsang et al., 2018). Using this method, we generated accurate 3D reconstructions of grouped ORNs from five diverse sensilla types. Our morphometric analysis confirmed that the sizes of neighboring ORNs are indeed different. The physically larger ORN in a pair is the dominant neuron in ephaptic interactions. Furthermore, we revised the published electric circuit model of the sensillum (Vermeulen and Rospars, 2004) to reflect the morphometric differences between grouped ORNs. Our electric circuit model suggests that the size difference between compartmentalized ORNs is a key factor driving the asymmetry observed empirically. The findings of this study provide insight into how morphometric features of a neuron can directly impact circuit interactions in other ephaptic environments.

1.4 References

Arvanitaki, A. (1942). Effects evoked in an axon by the activity of a contiguous one. J. Neurophysiol. *5*, 89–108.

Baker, T.C. (2008). Balanced olfactory antagonism as a concept for understanding evolutionary shifts in moth sex pheromone blends. J. Chem. Ecol. *34*, 971–981.

Baker, T.C., and Heath, J.J. (2005). Pheromones: Function and Use in Insect Control (Elsevier).

Barnett, J.A. (2003). A history of research on yeasts 5: The fermentation pathway. Yeast *20*, 509–543.

von Békésy, G. (1967). Mach band type lateral inhibition in different sense organs. J. Gen. Physiol. *50*, 519–532.

Benton, R., Vannice, K.S., Gomez-Diaz, C., Vosshall, L.B. (2009). Variant ionotropic glutamate receptors as chemosensory receptors in Drosophila. Cell *136*, 149–162.

Blot, A., and Barbour, B. (2014). Ultra-rapid axon-axon ephaptic inhibition of cerebellar Purkinje cells by the pinceau. Nat. Neurosci. *17*, 289–295.

Bokil, H., Laaris, N., Blinder, K., Ennis, M., Keller, A. (2001). Ephaptic interactions in the mammalian olfactory system. J. Neurosci. *21*, RC173.

de Bruyne, M., Clyne, P.J., Carlson, J.R. (1999). Odor coding in a model olfactory organ: the Drosophila maxillary palp. J. Neurosci. *19*, 4520–4532.

de Bruyne, M., Foster, K., Carlson, J.R. (2001). Odor coding in the Drosophila antenna. Neuron *30*, 537–552.

Cardé, R.T., Baker, T.C. (1984). Sexual communication with pheromones. In Chemical Ecology of Insects, (Springer), pp. 355–383.

Chapman, R.F., Ascoli-Christensen, A., White, P.R. (1991). Sensory coding for feeding deterrence in the grasshopper Schistocerca americana. J. Exp. Biol. *158*, 241–259.

Chapot, C.A., Euler, T., Schubert, T. (2017). How do horizontal cells ‘talk’ to cone photoreceptors? Different levels of complexity at the cone–horizontal cell synapse. J. Physiol. *595*, 5495–5506.

Clarke, S.E., Longtin, A., Maler, L. (2015). Contrast coding in the electrosensory system: Parallels with visual computation. Nat. Rev. Neurosci. *16*, 733–744.

Connell, R.J.O. (1985). Responses to pheromone blends in insect olfactory receptor neurons. J. Comp. Physiol. A *156*, 747–761.

Cork, a., Boo, K.S., Dunkelblum, E., Hall, D.R., Jee-Rajunga, K., Kehat, M., Kong JIE, E., Park, K.C., Tepgidagarn, P., Xun, L. (1992). Female sex pheromone of oriental tobacco budworm, Helicoverpa assulta (Guenee) (Lepidoptera: Noctuidae): Identification and field testing. J. Chem. Ecol. *18*, 403–418.

Cossé, a. a., Todd, J.L., Baker, T.C. (1998). Neurons discovered in male Helicoverpa zea antennae that correlate with pheromone-mediated attraction and interspecific antagonism. J. Comp. Physiol. *182*, 585–594.

Couto, A., Alenius, M., Dickson, B.J. (2005). Molecular, anatomical, and functional organization of the Drosophila olfactory system. Curr. Biol. *15*, 1535–1547.

Dacey, D.M., Packer, O.S. (2003). Colour coding in the primate retina: Diverse cell types and cone-specific circuitry. Curr. Opin. Neurobiol. *13*, 421–427.

Dweck, H.K., Ebrahim, S.A., Khallaf, M.A., Koenig, C., Farhan, A., Stieber, R., Weißflog, J., Svatoš, A., Grosse-Wilde, E., Knaden, M., Hansson, B. S. (2016). Olfactory channels associated with the Drosophila maxillary palp mediate short- and long-range attraction. eLife *5*, e14925.

Faber, D., Korn, H. (1973). A neuronal inhibition mediated electrically. Science *179*, 577–578.

Faber, D.S., Korn, H. (1989). Electrical field effects: their relevance in central neural networks. Physiol. Rev. *69*, 821–863.

Faucher, C., Forstreuter, M., Hilker, M., de Bruyne, M. (2006). Behavioral responses of Drosophila to biogenic levels of carbon dioxide depend on life-stage, sex and olfactory context. J. Exp. Biol. *209*, 2739–2748.

Furukawa, T., Furshpan, E.J. (1963). Two inhibitory mechanisms in the mauthner neurons of goldfish. J. Neurophysiol. *26*, 140–176.

Hallem, E., Carlson, J. (2006). Coding of odors by a receptor repertoire. Cell *125*, 143–160.

Hallem, E., Ho, M.G., Carlson, J.. (2004). The molecular basis of odor coding in the Drosophila antenna. Cell *117*, 965–979.

Hartline, H.K., Wagner, H.G., Ratliff, F. (1956). Inhibition in the eye of Limulus. J. Gen. Physiol. *39*, 651–673.

Horridge, G.A., Marčelja, L., Jahnke, R., Matič, T. (1983). Single electrode studies on the retina of the butterfly Papilio. J. Comp. Physiol. *150*, 271–294.

Jasper, H.H., Monnier, A.M. (1938). Transmission of excitation between excised non-myelinated nerves. An artificial synapse. J. Cell. Comp. Physiol. *11*, 259–277.

Jefferys, J.G. (1995). Nonsynaptic modulation of neuronal activity in the brain: electric currents and extracellular ions. Physiol. Rev. *75*, 689–723.

Jones, W.D., Cayirlioglu, P., Kadow, I.G., Vosshall, L.B. (2007). Two chemosensory receptors together mediate carbon dioxide detection in Drosophila. Nature *445*, 86–90.

Kaissling, K.E., Thorson, J. (1980). Insect olfactory sensilla: structure, chemical and electrical aspect of the functional organization. In D. B. Sattelle, L. M. Hall, J. G. Hildebarnd (Eds.), Receptors for Neurotransmitters, Hormones and Pheromones in Insects. (Elsevier/North-Holland Biomedical Press). 261-282.

Klaassen, L., Fahrenfort, I., Kamermans, M. (2012). Connexin hemichannel mediated ephaptic inhibition in the retina. Brain Res. *1487*, 25–38.

Kaissling, K. (1996). Peripheral mechanisms of pheromone reception in moths. Chem. Senses *21*, 257–268.

Kaissling, K.E. (1986). Chemo-electrical transduction in insect olfactory receptors. Annu. Rev. Neurosci. *9*, 121–145.

Kaissling, K.E., Kasang, G., Bestmann, H.J., Stransky, W., Vostrowsky, O. (1978). A new pheromone of the silkworm moth Bombyx mori - Sensory pathway and behavioral effect. Naturwissenschaften *65*, 382–384.

Katz, B.Y.B., Schmitt, O.H. (1940). Electric interaction between two adjacent nerve fibres. J. Physiol. *97*, 471–488.

Korn, H., Faber, D.S. (1980). Electrical field effect interactions in the vertebrate brain. Trends Neurosci. *3*, 6–9.

Kramer, J. De (1985). The electrical circuitry of an olfactory sensillum in Antheraea polyphemus. J. Neurosci. *5*, 2484–2493.

Kramer, R.H., Davenport, C.M. (2015). Lateral inhibition in the vertebrate retina: The case of the missing neurotransmitter. PLoS Biol. *13*, 1–8.

Kuffler, S.W. (1953). Discharge patterns and functional organization of mammalian retina. J. Neurophysiol. *16*, 37–68.

Kwon, J.Y., Dahanukar, A., Weiss, L. a, Carlson, J.R. (2007). The molecular basis of CO2 reception in Drosophila. Proc. Natl. Acad. Sci. U. S. A. *104*, 3574–3578.

Kwon, Y., Kim, S.H., Ronderos, D.S., Lee, Y., Akitake, B., Woodward, O.M., Guggino, W.B., Smith, D.P., Montell, C. (2010). Drosophila TRPA1 channel is required to avoid the naturally occurring insect repellent citronellal. Curr. Biol. *20*, 1672–1678.

Lam, S.S., Martell, J.D., Kamer, K.J., Deerinck, T.J., Ellisman, M.H., Mootha, V.K., Ting, A.Y. (2015). Directed evolution of APEX2 for electron microscopy and proximity labeling.

Nat. Methods *12*, 51–54.

Lin, C.C., Potter, C.J. (2015). Re-classification of Drosophila melanogaster trichoid and intermediate sensilla using fluorescence-guided single sensillum recording. PLoS One *10*, 1–14.

Lin, C.-C., Prokop-Prigge, K.A., Preti, G., Potter, C.J. (2015). Food odors trigger *Drosophila* males to deposit a pheromone that guides aggregation and female oviposition decisions. Elife *4*, 1–26.

Lin, H., Cao, D., Sethi, S., Zeng, Z., Chin, J.S.R., Chakraborty, T.S., Shepherd, A.K., Nguyen, C.A., Yew, J.Y., Su, C., et al. (2016). Hormonal modulation of pheromone detection enhances male courtship success. Neuron *90*, 1272–1285.

Prieto-Godino, L.L., Rytz, R., Cruchet, S., Bargeton, B., Abuin, L., Silbering, A.F., Ruta, V., Dal Peraro, M., Benton R. (2017). Evolution of acid-sensing olfactory circuits in Drosophilids. Neuron *93*, 661–676.

Mach, E. (1865). Qber die Wirkung der riiumlichen Vertheflung des Lichtreizes auf die Netzhau. Sitzungsberichte Der Math. Chnaturwissenschajlichen Klasse Der Kais. Akad. Der Wissenschaften *5*, 303–322.

Martell, J.D., Deerinck, T.J., Sancak, Y., Poulos, T.L., Mootha, V.K., Sosinsky, G.E., Ellisman, M.H., Ting, A.Y. (2012). Engineered ascorbate peroxidase as a genetically encoded reporter for electron microscopy. Nat. Biotechnol. *30*, 1143–1148.

Matić, T. (1983). Electrical inhibition in the retina of the butterfly Papilio - I. Four spectral types of photoreceptors. J. Comp. Physiol. *152*, 169–182.

Menzel, R., Blakers, M. (1976). Colour receptors in the bee eye-morphology and spectral sensitivity. J. Comp. Physiol. A *108*, 11–33.

Miriyala, A., Kessler, S., Rind, F.C., Wright, G.A. (2018). Burst firing in bee gustatory neurons prevents adaptation. Curr. Biol. *28*, 1585–1594.e3.

Montet, D., Ray, R.C., Zakhia-Rozis, N. (2014). Lactic acid fermentation of vegetables and fruits. Microorg. Ferment. Tradit. Foods 108–140.

Nakajima, Y. (1974). Fine structure of the synaptic endings on the Mauthner cell of the goldfish. J. Comp. Neurol. *156*, 375–402.

Nikonov, A. a, Leal, W.S. (2002). Peripheral coding of sex pheromone and a behavioral antagonist in the Japanese beetle, Popillia japonica. J. Chem. Ecol. *28*, 1075–1089.

Olsen, S.R., Wilson, R.I. (2008). Lateral presynaptic inhibition mediates gain control in an olfactory circuit. Nature *452*, 956–960.

Ramón, F., Moore, J.W. (1978). Ephaptic transmission in squid giant axons. Am. J. Physiol.

234, C162–C169.

Redkozubov, A. (1995). High electrical resistance of the bombykol cell in an olfactory sensillum of Bombyx mori: Voltage- and current-clamp analysis. J. Insect Physiol. *41*, 451–455.

Ronderos, D.S., Lin, C.-C., Potter, C.J., Smith, D.P. (2014). Farnesol-detecting olfactory neurons in Drosophila. J. Neurosci. *34*, 3959–3968.

Sagi, D., Hochstein, S. (1985). Lateral inhibition between spatially adjacent spatial-frequency channels? Percept. Psychophys. *37*, 315–322.

Schnaitmann, C., Haikala, V., Abraham, E., Oberhauser, V., Thestrup, T., Griesbeck, O., Reiff, D.F. (2018). Color processing in the early visual system of Drosophila. Cell. *172*, 318–330.

Semmelhack, J.L., Wang, J.W. (2009). Select Drosophila glomeruli mediate innate olfactory attraction and aversion. Nature *459*, 218–223.

Shanbhag, S.R., Müller, B., Steinbrecht, R.A. (1999). Atlas of olfactory organs of Drosophila melanogaster 1. Types, external organization, innervation and distribution of olfactory sensilla. Int. J. Insect Morphol. Embryol. *28*, 377–397.

Shanbhag, S.R., Müller, B., Steinbrecht, R.A. (2000). Atlas of olfactory organs of Drosophila melanogaster 2. Internal organization and cellular architecture of olfactory sensilla. Arthropod Struct. Dev. *29*, 211–229.

Shaw, S.R. (1975). Retinal resistance barriers and electrical lateral inhibition. Nature *255*, 480–483.

Silbering, a. F., Rytz, R., Grosjean, Y., Abuin, L., Ramdya, P., Jefferis, G.S.X.E., Benton, R. (2011). Complementary function and integrated wiring of the evolutionarily distinct Drosophila olfactory subsystems. J. Neurosci. *31*, 13357–13375.

Su, C.-Y., Menuz, K., Carlson, J.R. (2009). Olfactory perception: receptors, cells, and circuits. Cell *139*, 45–59.

Su, C.-Y., Menuz, K., Reisert, J., Carlson, J.R. (2012). Non-synaptic inhibition between grouped neurons in an olfactory circuit. Nature *492*, 66–71.

Suh, G.S.B., Wong, A.M., Hergarden, A.C., Wang, J.W., Simon, A.F., Benzer, S., Axel, R., Anderson, D.J. (2004). A single population of olfactory sensory neurons mediates an innate avoidance behaviour in Drosophila. Nature *431*, 854–859.

Triller, A., Korn, H. (1981). Morphologically distinct classes of inhibitory synapses arise from the same neurons: Ultrastructural identification from crossed vestibular interneurons intracellularly stained with HRP. J. Comp. Neurol. *203*, 131–155.

Tsang, T.K., Bushong, E.A., Boassa, D., Hu, J., Romoli, B., Phan, S., Dulcis, D., Su, C.-Y., Ellisman, M.H. (2018). High-quality ultrastructural preservation using cryofixation for 3D electron microscopy of genetically labeled tissues. eLife *7*, e35524.

Vermeulen, A., Rospars, J.-P. (2004). Why are insect olfactory receptor neurons grouped into sensilla? The teachings of a model investigating the effects of the electrical interaction between neurons on the transepithelial potential and the neuronal transmembrane potential. Eur. Biophys. J. *33*, 633–643.

Vroman, R., Klaassen, L.J., Kamermans, M. (2013). Ephaptic communication in the vertebrate retina. Front. Hum. Neurosci. *7*, 612.

Weiss, S. a, Preuss, T., Faber, D.S. (2008). A role of electrical inhibition in sensorimotor integration. Proc. Natl. Acad. Sci. U. S. A. *105*, 18047–18052.

Wilson, R.I., Mainen, Z.F. (2006). Early events in olfactory processing. Annu. Rev. Neurosci. *29*, 163–201.

Witzgall, P., Backman, a C., Svensson, M., Koch, U., Rama, F., El-Sayed, a, Brauchli, J., Arn, H., Bengtsson, M., Lofqvist, J. (1999). Behavioral observations of codling moth, Cydia pomonella, in orchards permeated with synthetic pheromone. Biocontrol *44*, 211–237.

Yang, E.C., Osorio, D. (1991). Spectral sensitivities of photoreceptors and lamina monopolar cells in the dragonfly, Hemicordulia tau. J. Comp. Physiol. A *169*, 663–669.

Yao, C.A., Ignell, R., Carlson, J.R. (2005). Chemosensory coding by neurons in the coeloconic sensilla of the Drosophila antenna. J. Neurosci. *25*, 8359–8367.

Zottoli, S.J., Faber, D.S. (1980). An identifiable class of statoacoustic interneurons with bilateral projections in the goldfish medulla. Neuroscience *5*, 1287–1302.

Chapter 2: High-quality ultrastructural preservation using cryofixation for 3D electron microscopy of genetically labeled tissues

2.1 Abstract

Electron microscopy (EM) offers unparalleled power to study cell substructures at the nanoscale. Cryofixation by high-pressure freezing offers optimal morphological preservation, as it captures cellular structures instantaneously in their near-native state. However, the applicability of cryofixation is limited by its incompatibility with diaminobenzidine labeling using genetic EM tags and the high-contrast *en bloc* staining required for serial block-face scanning electron microscopy (SBEM). In addition, it is challenging to perform correlated light and electron microscopy (CLEM) with cryofixed samples. Consequently, these powerful methods cannot be applied to address questions requiring optimal morphological preservation. Here we developed an approach that overcomes these limitations; it enables genetically labeled, cryofixed samples to be characterized with SBEM and 3D CLEM. Our approach is broadly applicable, as demonstrated in cultured cells, *Drosophila* olfactory organ and mouse brain. This optimization exploits the potential of cryofixation, allowing for quality ultrastructural preservation for diverse EM applications.

2.2 Introduction

The answers to many questions in biology lie in the ability to examine the relevant biological structures accurately at high resolution. Electron microscopy (EM) offers the unparalleled power to study cellular morphology and structure at nanoscale resolution (Leapman, 2004). Cryofixation by high-pressure freezing (hereafter referred to as cryofixation) is the optimal fixation method for samples of thicknesses up to approximately 500 µm (Dahl and Staehelin, 1989; McDonald, 1999; Moor, 1987; Shimoni et al., 1998). By rapidly freezing the samples in liquid nitrogen (-196 °C) under high pressure (~2100 bar), cryofixation immobilizes cellular structures within milliseconds and preserves them in their near-native state. In contrast, cross-linking based chemical fixation takes place at higher temperatures (≥4 °C) and depends on the infiltration of aldehyde fixatives, a process which takes seconds to minutes to complete. During chemical fixation, cellular structures may deteriorate or undergo rearrangement (Korogod et al., 2015; Steinbrecht and Müller, 1987; Szczesny et al., 1996) and enzymatic reactions can proceed (Kellenberger et al., 1992; Sabatini, 1963), potentially resulting in significant morphological artefacts.

Cryofixation is especially critical, and often necessary, for properly fixing tissues with cell walls or cuticles that are impermeable to chemical fixatives, such as samples from yeast, plant, *C. elegans*, and *Drosophila* (Ding, 1993; Doroquez et al., 2014; Kaeser et al., 1989; Kiss et al., 1990; McDonald, 2007; Müller-Reichert et al., 2003; Shanbhag et al., 1999, 2000; Winey et al., 1995). As cryofixation instantaneously halts all cellular processes, it also provides the temporal control needed to capture fleeting biological events in a dynamic process (Hess et al., 2000; Watanabe et al., 2013; Watanabe et al., 2013; Watanabe et al., 2014).

Despite the clear benefits of cryofixation, it is incompatible with diaminobenzidine (DAB) labeling reactions by genetic EM tags. For example, APEX2 (enhanced ascorbate peroxidase) is an engineered peroxidase that catalyzes DAB reaction to render target structures electron dense (Lam et al., 2015; Martell et al., 2012). Despite the successful applications of APEX2 to three-dimensional (3D) EM (Joesch et al., 2016), there has been no demonstration that APEX2 or other genetic EM tags can be activated following cryofixation. Conventionally, cryofixation is followed by freeze-substitution (Steinbrecht and Müller, 1987), during which water in the sample is replaced by organic solvents.

However, the resulting dehydrated environment is incompatible with the aqueous enzymatic reactions required for DAB labeling by genetic EM tags.

EM structures can also be genetically labeled with fluorescent markers through correlated light and electron microscopy (CLEM). Yet, performing CLEM with cryofixed samples also presents challenges. Fluorescence microscopy commonly takes place either before cryofixation (Brown et al., 2009; Kolotuev et al., 2010; McDonald, 2009) or at a later stage after the sample is embedded (Kukulski et al., 2011; Nixon et al., 2009; Schwarz and Humbel, 2009). However, if the specimen is dissected from live animals, the time taken to acquire fluorescence images delays cryofixation and could cause ultrastructural deterioration. In order for fluorescence microscopy to take place after embedding, special acrylic resins need to be used (Kukulski et al., 2011; Nixon et al., 2009; Schwarz and Humbel, 2009) and only a low concentration of osmium tetroxide stain can be tolerated (De Boer et al., 2015; Watanabe et al., 2011). Although one can in principle perform fluorescence microscopy in cryofixed samples after rehydration, fluorescence images have only been acquired in sucrose-infiltrated cryosections (300-500 nm) (Ripper et al., 2008; Stierhof and El Kasmi, 2010). Moreover, no protocol has been developed to prepare large cryofixed tissues expressing genetic CLEM markers for high-contrast EM imaging. These constraints limit the applicability of CLEM for cryofixed samples.

Another disadvantage of cryofixation is that *en bloc* staining during freeze-substitution is often inadequate. As a result, post-staining of ultramicrotomy sections is frequently needed for cryofixed samples (Shanbhag et al., 1999, 2000; Takemura et al., 2013). However, post-staining could be labor-intensive and time-consuming, especially for volume EM (Ryan et al., 2016; Zheng et al., 2017). Critically, on-section staining is impossible for samples imaged with block-face volume EM techniques (Briggman and

Bock, 2012), such as serial block-face scanning electron microscopy (SBEM) (Denk and Horstmann, 2004). A large amount of heavy metal staining is necessary for SBEM to generate sufficient back-scatter electron signal and to prevent specimen charging (Deerinck et al., 2010; Kelley et al., 1973; Tapia et al., 2012). Therefore, it remains impossible to image cryofixed samples with SBEM or other techniques that require high-contrast staining.

To overcome these limitations of cryofixation, here we present a robust approach, named the CryoChem Method (CCM), which combines key advantages of cryofixation and chemical fixation. This technique enables labeling of target structures by genetically encoded EM tags or fluorescent markers in cryofixed samples, and permits high-contrast *en bloc* heavy metal staining sufficient for SBEM. Specifically, we rehydrate cryofixed samples after freeze-substitution to make the specimen suitable for subsequent aqueous reactions and fluorescence imaging. We successfully apply CCM to multiple biologically significant systems with distinct ultrastructural morphology, including cultured mammalian cells, *Drosophila* olfactory organ (antenna) and mouse brain. By overcoming critical technical barriers, our method exploits the potential of cryofixation, making it compatible with genetically encoded EM tags and any EM techniques that require substantial heavy metal staining. Furthermore, the versatility of CCM allows us to achieve 3D CLEM in a well-preserved mouse brain by permitting SBEM after fluorescent imaging of a frozen-rehydrated specimen.

2.3 Results

Given that a key limitation of cryofixation arises from the dehydrated state of the samples after freeze-substitution (Table 2.1), it is imperative that our approach delivers a cryofixed specimen that is fully hydrated and can then be processed at higher temperatures (4 °C or room temperature) for enzymatic reactions and/or high-contrast *en bloc* heavy metal staining. It has been demonstrated that cryofixed samples can be rehydrated for immunogold labeling or fluorescence imaging following cryosectioning (Dhonukshe et al., 2007; Ripper et al., 2008; Stierhof and El Kasmi, 2010; van Donselaar et al., 2007), but these approaches only yield modest EM contrast. In addition, the methods are incompatible with volume EM techniques and have yet to be successfully combined with genetic labeling using APEX2.

2.3.1. The CryoChem Method

To achieve the ultrastructural preservation of cryofixation and the versatility of chemical fixation, we developed a hybrid protocol which we refer to hereafter as the CryoChem Method (CCM) (Table 2.1). Importantly, we devised a freeze-substitution cocktail (see below) that allows preservation of APEX2 enzymatic activity and signals from fluorescent proteins. CCM begins with high-pressure freezing of a sample, followed by freeze-substitution in an acetone solution with glutaraldehyde (0.2%), uranyl acetate (0.1%), methanol (2%) and water (1%), to further stabilize the cryo-preserved structures at low temperatures. After freeze-substitution, the sample is rehydrated gradually on ice with a series of acetone solutions containing an increasing amount of water or 0.1M HEPES. Once completely rehydrated, the cryofixed sample is amenable for imaging with fluorescence microscopy, DAB labeling reactions using genetically encoded tags, and the high-contrast *en bloc* staining (e.g. osmium-thiocarbohydrazide-osmium and uranyl acetate) normally reserved only for chemically fixed samples. Afterwards, the sample is dehydrated through a series of ethanol solutions and acetone, then infiltrated with epoxy resin and cured using standard EM procedures. To minimize volume artefact, epoxy resin is chosen because it causes minimal tissue shrinkage during embedding (<2%) compared to other embedding media (Kushida, 1962). The resin embedded samples can be sectioned or imaged directly with any desired EM technique (Figure 2.1, see *Materials and Methods* for details).

2.3.2 CryoChem Method offers high-quality ultrastructural preservation and sufficient *en bloc* staining for SBEM

To determine whether CCM provides high-quality ultrastructural preservation, we first tested the method in a mammalian cell line. Using transmission electron microscopy (TEM), well-preserved mitochondria and nuclear membrane were observed in the CCM-processed cells (data not shown). Given that cryofixation is often necessary for properly fixing tissues surrounded by a barrier to chemical fixatives (Steinbrecht, 1980; Steinbrecht and Müller, 1987), we next tested CCM in a *Drosophila* olfactory organ, the antenna, which is encased in a waxy cuticle (Figure 2.2A and 2.2B). A hallmark of optimally preserved antennal tissues prepared by cryofixation is the smooth appearance of membrane structures (Shanbhag et al., 1999, 2000; Steinbrecht, 1980; Steinbrecht and Müller, 1987). In the insect antenna, auxiliary cells extend microlamellae to surround the olfactory receptor neurons (ORNs), forming the most membrane-rich regions in the antenna. We therefore focused on this structure to evaluate the quality of morphological preservation afforded by our method. In the CCM-processed antennal tissues, we found that the delicate structures of the microlamellae were well-preserved (Figure 2.2B), unlike the chemically fixed counterparts in which microlamellae were disorganized and distorted (Figure 2.2A) (Steinbrecht, 1980). Furthermore, there were numerous signs of extraction of cellular materials in the chemically fixed antenna (Figure 2.2A1, arrows), but not in the CCM-processed specimen (Figure 2.2B). Importantly, the overall ultrastructural preservation achieved through CCM resembles that obtained by standard cryofixation and freeze-substitution protocols (Shanbhag et al., 1999, 2000). This observation also suggests that the rehydration step in CCM leads to little, if any, swelling in the antenna tissue.

In contrast to fly antennae, which can be dissected expeditiously and frozen in the live state, certain tissues (e.g., mouse brain) are difficult to cryofix from life without tissue damage caused by anoxia or mechanical stress associated with dissection. In these cases, cryofixation can be performed after aldehyde perfusion and still produce quality morphological preservation (Sosinsky et al., 2008). To test whether CCM can improve morphological preservation of aldehyde-perfused samples, we cryofixed vibratome sections (100 µm) from an aldehyde-perfused mouse brain and processed the sample with CCM. Compared to specimens processed by a standard EM preparation method that involved dehydration on ice (Figure 2.2C), the CCM-processed samples, which were initially dehydrated through freeze-substitution, showed smoother membranes and an increase in cytoplasmic density (Figure 2.2D). This result indicates an improvement in morphological preservation and agrees with our previous observation that cellular morphology can be markedly improved even when cryofixation is performed after aldehyde perfusion (Sosinsky et al., 2008).

Of note, we adopted a high-contrast *en bloc* staining protocol (Deerinck et al., 2010; Tapia et al., 2012; West et al., 2010; Williams et al., 2011) when processing *Drosophila* antennae and mouse brain. An adequate level of heavy metals was incorporated into these cryofixed samples to allow for successful imaging by SBEM (Figure 2.2B and 3), even without nitrogen gas injection to dissipate any charge build-up that often occurs on samples of low conductivity (Deerinck et al., 2017) (Figure 2.3D). This *en bloc* staining protocol is normally reserved only for chemically fixed tissues, but is now made compatible with cryofixed samples by CCM.

2.3.3 CryoChem Method enables DAB labeling in cryofixed samples expressing APEX2

Next we determined if DAB labeling reaction can be performed in cryofixed samples with CCM (Figure 2.3A). Using the CCM-processed cultured cells expressing APEX2, we observed DAB labeling in the targeted organelles (mitochondria) in the transfected cells, compared to the untransfected controls (Figure 2.3B). We further validated this approach in the CCM-processed *Drosophila* antenna; successful DAB labeling was also detected in genetically identified ORNs expressing APEX2 with X-ray microscopy (data not shown). This imaging technique facilitates the identification of the region of interest for SBEM (Figure 2.3C), as we and others reported previously (Bushong et al., 2015; Ng et al., 2016). Crucially, we demonstrated that an EM volume of a genetically labeled, cryofixed ORN can be acquired with SBEM, which allowed for an accurate 3D reconstruction of the ORN through semi-automated segmentation (Figure 2.3D). Taken together, these results demonstrate that CCM can reliably generate DAB labeling by genetically encoded EM tags in cryofixed samples.

2.3.4 Fluorescence is well-preserved in CryoChem-processed samples

To determine whether CCM is compatible with fluorescence microscopy, we first evaluated the degree to which fluorescence level is affected after CCM processing. Using confocal microscopy, we quantified GFP fluorescence in the soma of unfixed *Drosophila* ORNs and that from the CCM-processed samples after rehydration (Figure 2.4). Remarkably, GFP fluorescence intensities of the fresh and the CCM-processed ORNs are essentially indistinguishable with respect to their distributions (Figure 2.4A) and average levels (Figure 2.4B). This result indicates that CCM processing has little effect on GFP fluorescence in fly ORNs, likely due to the use of mild fixatives during freeze-substitution in our protocol. Similarly, we observed strong GFP signals in the mouse brain after the cryofixed sample was rehydrated (data not shown). Together, our results indicate that CCM-processed sample can serve as a robust substrate for fluorescence imaging. As such, CCM allows fluorescence imaging to be combined with DAB labeling and high-contrast *en bloc* staining in the same cryofixed sample, a critical advance to cryofixation-rehydration methods (Dhonukshe et al., 2007; Ripper et al., 2008; Stierhof and El Kasmi, 2010; van Donselaar et al., 2007).

2.3.5 3D correlative light and electron microscopy (CLEM) in CCM-processed samples expressing fluorescent markers

Finally, we took advantage of the fact that fluorescence microscopy can take place in a cryofixed sample before resin embedding to develop a protocol for 3D CLEM in CCM-processed specimens (Figure 2.5A, see *Materials and Methods* for details), so that the correlation can be achieved in optimally preserved tissues. The protocol first uses the core CCM steps to deliver a frozen-rehydrated sample. Subsequently, DRAQ5 DNA stain is introduced to the sample to label the nuclei, which can then serve as fiducial markers for CLEM. Next, the region containing target cells expressing fluorescent markers is imaged with confocal microscopy, during which signals from DRAQ5 and fluorescent markers are both acquired. After confocal microscopy, the sample is *en bloc* stained with multiple layers of heavy metals (Deerinck et al., 2010; Tapia et al., 2012; West et al., 2010; Williams et al., 2011), then dehydrated and embedded as in a typical CCM protocol. Subsequently, the embedded sample is imaged with X-ray microscopy. The resulting micro-computed tomography volume can be registered to the confocal volume using the nuclei as fiducial markers, so that the region of interest (ROI) for SBEM can be identified. After SBEM imaging, the EM volume can be registered to the confocal volume in a similar fashion for 3D CLEM.

As a proof of principle, we performed 3D CLEM in an aldehyde-perfused, CCM-processed mouse brain expressing tdTomato in a subset of neurons. To this end, we first determined if DRAQ5 staining can be performed in a frozen-rehydrated specimen. Using confocal microscopy, we were able to observe DRAQ5 labeling of the nuclei in a cryofixed brain slice after rehydration (Figure 2.5B). We used the labeled nuclei as fiducial markers to register the X-ray volume with the confocal data (Figure 2.5B) and thereby target a ROI with tdTomato-expressing neurons for SBEM imaging.

Similarly, we were able to register the confocal volume to the SBEM volume (Figure 2.5C). Of note, the CLEM accuracy was ensured by using a subset of DRAQ5-labeled heterochromatin structures and their corresponding counterparts in EM as finer fiducial points (Figure 2.5C). Furthermore, the fluorescent markers made it possible to identify the target cell bodies (Figure 2.5D) and the fine neuronal processes (Figure 2.5E) in the SBEM volume. Lastly, we note that with CCM, fluorescence microscopy in cryofixed specimens takes place before *en bloc* EM staining. Therefore, our protocol does not require special resins for embedding and permits high-contrast staining with high concentrations of osmium tetroxide.

2.4 Discussion

We described here a hybrid method, named CryoChem, which combines key advantages of cryofixation and chemical fixation to substantially broaden the applicability of the optimal fixation technique. With CCM, it is now possible to label target structures with DAB by a genetically encoded EM tag and deposit high-contrast *en bloc* staining in cryofixed tissues. In addition, with CCM, one can image cells expressing fluorescent markers before resin embedding and perform 3D CLEM in cryofixed specimens. Our method thereby provides an alternative to conventional cryofixation and chemical fixation methods.

The modular nature of CCM (Figure 2.1) makes it highly versatile as researchers can modify the modules to best suit their needs. For instance, to prevent over-staining, one can replace the high-contrast *en bloc* staining step (osmium-thiocarbohydrazide-osmium and uranyl acetate) (Deerinck et al., 2010; Tapia et al., 2012; West et al., 2010; Williams et al., 2011) with a single round of osmium tetroxide staining for thin section TEM (Figure 2.2C, 2.2D and 2.3B) or electron tomography. In addition, CCM is essentially compatible with a wide range of reactions catalyzed by EM tags other than APEX2 (Ellisman et al., 2015). For example, the protein labeling reactions mediated by miniSOG (Shu et al., 2011) and the tetracysteine-based methods using FIAsH and ReAsH (Gaietta et al., 2002), or the non-protein biomolecule labeling reactions using Click-EM (Ngo et al., 2016) or ChromEM (Ou et al., 2017). The versatility of CCM will likely expand the breath of biological questions that can be addressed using cryofixed samples.

In addition to using EM tags, we have also developed a 3D CLEM protocol (Figure 2.5A) that allows optimally preserved EM structures to be genetically labeled with fluorescent markers in CCM-processed tissues. In contrast to EM tags, fluorescent markers do not generate electron-dense products (e.g. DAB polymers) that can obscure the subcellular structures. Moreover, with multicolor CLEM, one can utilize multiple readily available genetically encoded fluorescent markers to label different target structures or cells. Using the 3D CLEM protocol, one could also pinpoint labeled subcellular structures (e.g., microtubules) or proteins (e.g., ion channels) in an EM volume with super-resolution microscopy. Furthermore, the ability to genetically label target neurons with fluorescent markers or EM tags in CCM-processed tissues can facilitate circuit reconstructions of identified neurons in optimally preserved specimens.

The advantages of CCM makes it particularly suited for addressing biological questions that require optimal and rapid preservation of a genetically labeled structure. For example, to construct an accurate model to describe the biophysical properties of a neuron, it is essential to acquire morphological measurements based on faithfully preserved ultrastructures. CCM processing provides such an opportunity; we were able to obtain a 3D reconstruction of a genetically labeled *Drosophila* ORN at nanoscale resolution with quality morphological preservation (Figure 2.3D). In addition, by combining CCM with Flash-and-Freeze EM (Watanabe et al., 2014a, 2014b) and electron tomography, it is possible to capture the fast morphological changes of genetically labeled vesicles in 3D during synaptic transmission.

Despite its versatility, multiple factors could potentially limit the applicability of CCM. First, given that the core fixation step of CCM is cryofixation, the size of the sample is constrained by the vitrification limit of up to approximately 500 µm (Dahl and Staehelin, 1989; McDonald, 1999; Moor, 1987; Shimoni et al., 1998). In addition, freeze damage due to ice crystal formation can occur (Korogod et al., 2015; Ripper et al., 2008; Shanbhag et al., 2000). Therefore, one should be mindful of freeze damage when performing ultrastructural analysis. Moreover, CCM can only improve the temporal resolution of biological events captured if the specimen is frozen in the live state, but not when the sample was first chemically fixed (e.g. aldehyde-perfused mouse brain). Finally, there are also concerns that some molecules may be lost during rehydration if they are not properly fixed during freeze-substitution (Ripper et al., 2008).

In conclusion, CCM is applicable to addressing questions in diverse tissue types, as demonstrated here with cultured mammalian cells or tissues of *Drosophila* antennae and mouse brains. Notably, identical solutions and experimental conditions were used for these different tissues in all core steps (Figure 2.1). Thus, the protocol described here can likely be readily adapted to cells and tissues of other biological systems. In addition, we demonstrated that CCM can further improve the ultrastructure of an aldehyde-perfused brain (Figure 2.2C and 2.2D). Given that aldehyde perfusion is often required for the dissection of deeply embedded or fragile tissues, the compatibility of CCM with aldehyde fixation further broadens the applicability of the method.

2.5 Materials and methods

Cultured cells preparation

HEK 293T cells (ATCC, Gaithersburg, MD) were grown on 1.2 mm diameter punches of Aclar (2 mil thick; Electron Microscopy Sciences, Hatfield, PA) for 48 hours, in a humidified cell culture incubator with 5% CO_2 at 37 °C. Authentication was guaranteed by ATCC, including STR profiling. The cells were negative for mycoplasma, as confirmed by using the Universal Mycoplasma Detection Kit (ATCC, Gaithersburg, MD). The culture medium used was DMEM (Mediatech Inc., Manassas, VA) supplemented with 10% fetal bovine serum (Gemini Bio-Products, West Sacramento, CA). The cells were transfected with Lipofectamine 2000 (Invitrogen, Carlsbad, CA) with a plasmid carrying APEX2 targeted to mitochondria (pcDNA3-Mito-V5-APEX2, Addgene #72480; Lam et al., 2015). At 24 hours after transfection, the cells were used for CCM processing.

DNA constructs and *Drosophil*a transgenesis

Orco cDNA was a gift from Dr. Aidan Kiely, and APEX2 DNA was acquired from Addgene (APEX2-NES, #49386). Membrane targeting of APEX2 was achieved by fusing the marker protein to the C-terminus of mCD8GFP or to the N-terminus of Orco. Briefly, gel-purified PCR fragments of mCD8GFP, APEX2, and/or Orco were pieced together with Gibson Assembly following manufacturer's instructions (New England Biolabs, Ipswich, MA). A linker (SGGGG) was added between APEX2 and its respective fusion partner. In the APEX2-Orco construct, a myc tag was included in the primer and added to the N-terminus of APEX2 to enable the detection of the fusion protein by immunostaining. To facilitate Gateway Cloning (ThermoFisher Scientific, Waltham, MA), the attB1 and attB2 sites were included in the primers and added to the ends of the Gibson assembly product by PCR amplification. The PCR products were then purified and cloned into pDONR221 vectors via BP Clonase II (Life Technologies, Carlsbad, CA). The entry clones were recombined into the pBID-UASC-G destination vector (Wang et al., 2012) using LR Clonases II (Life Technologies, Carlsbad, CA).

Drosophila transgenic lines were derived from germline transformations using the ΦC31 integration systems (Groth et al., 2004; Markstein et al., 2008). All transgenes described in this study were inserted into the attP40 landing site on the second chromosome (BestGene Inc., Chino Hills, CA). Target expression of APEX2 and mCD8GFP in the ORNs was driven by the Or47b-GAL4 driver (#9984, Bloomington Drosophila Stock Center; Fishilevich & Vosshall, 2005; Figure 2.2-2.4). Flies were raised on standard cornmeal food at 25°C in a 12:12 light-dark cycle.

***Drosophila* antennae preparation**

Six to eight days old flies were cold anesthetized and then pinned to a Sylgard dish. The third segments of the antennae were removed from the head of the fly with a pair of fine forceps and then immediately transferred to a drop of 1X PBS on the dish. With a sharp glass microelectrode, a hole was poked in the antenna to facilitate solution exchange. It is critical that the tissue remained in PBS at all times to prevent deflation. The antenna should remain plump and maintain its shape prior to cryofixation.

Chemical fixation of *Drosophila* antenna

Antennae were dissected as described above, and then incubated at 4 °C for 18 hours in Karnovsky fixatives: 2% paraformaldehyde (Fisher Scientific, Hampton, NH)/2.5% glutaraldehyde (Ted Pella, Redding, CA)/2 mM $CaCl_2$ (Sigma-Aldrich, St. Louis, MO) in 0.1 M sodium cacodylate (Ted Pella, Redding, CA). Next, samples were washed in 0.1 M sodium cacodylate for 10 minutes and in a solution of 100 mM glycine (Bio-Rad Laboratories, Hercules, CA) in 0.1 M sodium cacodylate for another 10 minutes, and twice more in 0.1 M sodium cacodylate. All washing steps were performed on ice. The following *en bloc* heavy metal staining, dehydration and resin embedding steps were carried out as described in the CryoChem Method section below.

Transgenic mice and virus-mediated gene transfer

Animals were handled in accordance with the guidelines established by the *Guide for Care and Use of Laboratory Animals* and approved by UCSD Animal Care and Use Committee. To introduce GFP and tdTomato fluorescent markers in a mouse brain, GFP was expressed in the tyrosine hydroxylase (TH)-expressing neurons and tdTomato in the corticotropin releasing factor (CRF)-expressing neurons. A CRF driver mouse line (B6.Cg-Crh$^{tm1(cre)Zjh}$/J, Jackson laboratory) expressing CRE recombinase under the control of the Crh promoter/enhancer elements was first crossed to a tdTomato reporter line (B6.Cg-Gt.ROSA.26Sor$^{tm14(CAG\text{-}tdTomato)Hze}$/J, Jackson Laboratory). The progeny was then crossed to a TH-GFP mouse line (Kessler et al., 2003), obtaining a transgenic model stably expressing GFP in dopaminergic (TH^{+}) neurons and CRE/tdTomato in CRF-releasing neurons. To test the 3D CLEM protocol and the morphological preservation offered by CCM (Figure 2.2C, 2.2D and 2.5), a similar strategy was used to generate a mouse expressing CRE/tdTomato in CRF-releasing neurons.

Mouse brain preparation

Mice were anesthetized with ketamine/xylazine and then transcardially perfused with Ringer's solution followed by 0.5% (Figure 2.2C, 2.2D and 2.5) glutaraldehyde/2 mM $CaCl_2$. The animal was perfused for 10 minutes with the fixatives and then the brain was removed and placed in ice-cold fixative for 1 hour. The brain was then cut into 100-μm thick slices using a vibrating microtome. Slices were either processed for chemical fixation (Figure 2.2C) or stored in ice-cold 0.15 M sodium cacodylate for around 4 hours until used for high-pressure freezing (Figure 2.2D, Figure 2.5).

Chemical fixation of mouse brain

The aldehyde-perfused mouse brain slices were post-fixed in 2.5% glutaraldehyde for 20 minutes, then washed with 0.15 M sodium cacodylate five times for 5 minutes on ice. Next, the samples were incubated in 0.15 M sodium cacodylate with 100 mM glycine for 5 minutes on ice, then washed in 0.15 M sodium cacodylate similarly. The following *en bloc* heavy metal staining, dehydration and resin embedding steps were carried out as described in the CryoChem Method section below.

CryoChem Method:

(I) Cryofixation by high-pressure freezing

Cultured cells: Aclar disks were placed within the well of a 100 □m-deep membrane carrier. The cells were covered with the culture medium and then high-pressure frozen with a Leica EM Pact 2 unit.

Drosophila antennae: The third antennal segment was dissected as described above. Antennae from the same fly were transferred into the 100 □m-deep well of a type A planchette filled with 20% BSA (Sigma-Aldrich, St. Louis, MO) in 0.15 M sodium cacodylate. The well of the type A planchette was then covered with the flat side of a type B planchette to secure the sample. The samples were immediately loaded into a freezing holder and frozen with a high-pressure freezing machine (Bal-Tec HPM 010). Planchettes used for cryofixation were pre-coated with 1-hexadecene (Sigma-Aldrich, St. Louis, MO) to prevent planchettes A and B from adhering to each other so as to allow solution to reach the samples during freeze-substitution.

Mouse brain slices: A 1.2 mm tissue puncher was used to cut a portion of hypothalamus expressing tdTomato (Figure 2.2D, Figure 2.5) from a tissue slice. The tissue punch was placed into a 100 μm-deep membrane carrier and surrounded with 20% BSA in 0.15 M sodium cacodylate. The specimen was high-pressure frozen as described for the *Drosophila* antennae.

All frozen samples were stored in liquid nitrogen until further processing.

(II) Freeze-substitution

Frozen samples in planchettes were transferred in a liquid nitrogen bath to cryo-vials containing the freeze-substitution solution. To prepare the freeze-substitution solution of 0.2% glutaraldehyde, 0.1% uranyl acetate, 2% methanol and 1% water in acetone, a 10 mL solution was prepared by adding 80 μL of 25% aqueous glutaraldehyde, 200 μL of 5% uranyl acetate (Electron Microscopy Sciences, Hatfield, PA) dissolved in methanol, and 20 μL of water to acetone (ACROS Organics, USA). Next, the sample vials were transferred to a freeze-substitution device (Leica EM AFS2) at -90 °C for 58 hours, from -90 °C to -60 °C for 15 hours (with the temperature raised at 2 °C/hr), at -60 °C for 15 hours, from -60 °C to -30 °C for 15 hours (at +2 °C/hr), and then at -30 °C for 15 hours. In the last hour at -30°C, samples were washed three times in an acetone solution with 0.2% glutaraldehyde and 1% water for 20 minutes. The cryo-tubes containing the last wash were then transferred on ice for an hour.

(III) Rehydration

The freeze-substituted samples were then rehydrated gradually in a series of nine rehydration solutions (see below). The samples were transferred from the freeze-substitution solution to the first rehydration solution (5% water, 0.2% glutaraldehyde in acetone) on ice for 10 minutes. The rehydration step was repeated in a stepwise manner until the samples were fully rehydrated in the final rehydration solution (0.1 M and 0.15 M sodium cacodylate for cells and antennae or mouse brain slices, respectively) (van Donselaar et al., 2007):

1) 5% water, 0.2% glutaraldehyde in acetone
2) 10% water, 0.2% glutaraldehyde in acetone
3) 20% water, 0.2% glutaraldehyde in acetone
4) 30% water, 0.2% glutaraldehyde in acetone
5) 50% 0.1M HEPES (Gibco, Taiwan), 0.2% glutaraldehyde in acetone
6) 70%, 0.1M HEPES, 0.2% glutaraldehyde in acetone
7) 0.1 M HEPES
8) 0.1 M / 0.15 M sodium cacodylate with 100 mM glycine
9) 0.1 M / 0.15 M sodium cacodylate

After rehydration, samples were removed from the planchettes using a pair of forceps under a stereo microscope to a 0.1 M (cells and antenna) / 0.15 M (brain) sodium cacodylate solution in a scintillation vial on ice. It is important that subsequent DAB labeling and *en bloc* heavy metal staining are carried out in scintillation vials instead of the planchettes because metal planchettes may react with the labeling or staining reagents.

(IV) DRAQ5 staining

Mouse brain slices were incubated in DRAQ5 (1:1000 in 0.15 M sodium cacodylate buffer; Cell Signaling Technology, Danvers, MA) on ice for 60 minutes. Then the samples were washed in 0.15 M sodium cacodylate three times for 10 minutes on ice before fluorescence imaging.

(V) Fluorescence imaging

Drosophila antennae: Freshly dissected or cryofixed-rehydrated antennae (*10x UAS-mCD8GFP-APEX2; Or47b-GAL4*) were mounted in FocusClear (Cedarlane Labs, Burlington, Canada) between two cover glasses (#1.5 thickness, 22 mm x 22 mm, Fisher Scientifiic, Hampton, NH) separated by two layers of spacer rings. Confocal images were collected on an Olympus FluoView 1000 confocal microscope with a 60X water-immersion objective lens. The 488 nm laser was used to excite GFP and all images were acquired at the same laser power and gain to enable comparison between the fresh vs cryofixed-rehydrated samples.

Mouse brain slices: After freeze-substitution and rehydration, the specimens were placed in ice-cold 0.15 M sodium cacodylate for imaging. Confocal volumes of DRAQ5 and tdTomato signals (Figure 2.5) were collected on an Olympus FluoView 1000 confocal microscope with a 20X air and 60X water objectives using 561 nm and 633 nm excitation.

(VI) DAB labeling of target structures by APEX2

Cultured cells: Samples were transferred to a 0.05% DAB (Sigma-Aldrich, St. Louis, MO) solution in 0.1 M sodium cacodylate for 5 minutes on ice to allow DAB to diffuse into the tissue. To label the mitochondria in the APEX2-expressing cells, samples were then transferred to a 0.05% DAB solution with 0.015% H_2O_2 (Fisher Scientific, Hampton, NH) in 0.1 M sodium cacodylate until DAB labeling was visible under a microscope (~5 minutes on ice). After the reaction, samples were washed three times with 0.1 M sodium cacodylate on ice for 10 minutes.

Drosophila antennae: Samples were first placed into a 0.05% DAB solution in 0.1 M sodium cacodylate for an hour on ice to allow DAB to access target neurons underneath the cuticle in the antenna. To label APEX2-expressing ORNs, antennae were then transferred into a 0.05% DAB solution with 0.015% H_2O_2 in 0.1 M sodium cacodylate for an hour on ice. After the reaction, samples were washed three times with 0.1 M sodium cacodylate on ice for 10 minutes.

(VII) *en bloc* heavy metal staining for TEM and SBEM

For TEM: Cultured cells and mouse brain slices were incubated in 2% OsO_4 (Electron Microscopy Sciences, Hatfield, PA)/1.5% potassium ferrocyanide (Mallinckrodt, Staines-Upon-Thames, UK)/2 mM $CaCl_2$ in 0.1 M (cells) or 0.15 M (brain) sodium cacodylate for an hour on ice. Then samples were washed in water five times for 5 minutes on ice prior to the dehydration step detailed below.

For SBEM: *Drosophila* antennae and mouse brain slices were incubated in 2% OsO_4/1.5% potassium ferrocyanide/2 mM $CaCl_2$ in 0.1 M (antennae) or 0.15 M (brain) sodium cacodylate for an hour at room temperature. Then samples were washed in water five times for 5 minutes and transferred to 0.5% thiocarbohydrazide (filtered with 0.22 µm filter before use; Electron Microscopy Sciences, Hatfield, PA) for 30 minutes at room temperature. Samples were washed in water similarly and incubated in 2% OsO_4 for 30 minutes at room temperature. Afterwards, samples were rinsed with water, then transferred to 2% aqueous uranyl acetate (filtered with 0.22 µm filter) at 4 °C overnight. In the next morning, samples were first washed in water five times for 5 minutes and then subjected to the dehydration steps detailed below.

(VIII) Dehydration

Samples were dehydrated with a series of ethanol solutions and acetone in six steps of 10 minutes each: 70% ethanol, 90% ethanol, 100% ethanol, 100% ethanol, 100% acetone, 100% acetone. All ethanol dehydration steps were carried out on ice, and the acetone steps at room temperature. The first acetone dehydration step was carried out with ice-cold acetone, and the second one was with acetone kept at room temperature.

(IX) Resin infiltration

Cultured cells: Samples were transferred to a Durcupan ACM resin/acetone (1:1) solution for an hour on a shaker at room temperature. The samples were then transferred to fresh 100% Durcupan ACM resin overnight and subsequently placed in fresh resin for four hours. While in 100% resin, samples were placed in a vacuum chamber on a rocker to facilitate the removal of residual acetone. Finally, the samples were embedded in fresh resin at 60 °C for two days.

Drosophila antennae and mouse brain slices: Samples were transferred to a Durcupan ACM resin/acetone (1:1) solution overnight on a shaker. The next day, samples were transferred into fresh 100% Durcupan ACM resin twice, with six to seven hours apart. While in 100% resin, samples were placed in a vacuum chamber on a rocker to facilitate the removal of residual acetone. After the overnight incubation in 100% resin, samples were embedded in fresh resin at 60 °C for at least two days.

Durcupan ACM resin (Sigma Aldrich, St. Louis, MO) composition was 11.4 g component A, 10 g component B, 0.3 g component C, and 0.1 g component D.

X-ray Microscopy (microcomputed tomography)

Drosophila antennae: Microcomputed tomography (microCT) was performed on resin-embedded specimens using a Versa 510 X-ray microscope (Zeiss). Flat-embedded specimens were glued to the end of an aluminum rod using cyanoacrylic glue. Imaging was performed with a 40X objective using a tube current of 40 kV and no source filter. Raw data consisted of 1601 projection images collected as the specimen was rotated 360 degrees. The voxel dimension of the final tomographic reconstruction was 0.4123 µm.

Mouse brain slices: X-ray microscopy scan was collected of a resin-embedded sample at 80 kVp with a voxel size of 0.664 µm prior to mounting for SBEM imaging. A second scan was collected of the mounted specimen at 80 kVp with 0.7894 µm voxels.

Transmission Electron Microscopy

Ultrathin sections (70 nm) were collected on 300 mesh copper grids. Samples were post-stained with either Sato's lead solution only (cultured cells) or with 2% uranyl acetate and Sato's lead solution (mouse brain slices). Sections were imaged on an FEI Spirit TEM at 80 kV equipped with a 2k x 2k Tietz CCD camera.

Serial Block-face Scanning Electron Microscopy

Drosophila antennae: Following microcomputed tomography to confirm proper orientation of region of interest, specimens were mounted on aluminum pins with conductive silver epoxy (Ted Pella, Redding, CA). The specimens were trimmed to remove excess resin above ROI and to remove silver epoxy from sides of specimen. The specimens were sputter coated with gold-palladium and then imaged using a Gemini scanning electron microscope (Zeiss) equipped with a 3View2XP and OnPoint backscatter detector (Gatan). Images were acquired at 2.5 kV accelerating voltage with a 30 µm condenser aperture and 1 µsec dwell time; Z step size was 50 nm; raster size was 12k x 9k and Z dimension was 1200 sections. Volumes were either collected in variable pressure mode with a chamber pressure of 30 Pa and a pixel size of 3.8 nm (Figure 2.3D) or using local gas injection (Deerinck et al., 2017) set to 85% and a pixel size of 6.5 nm (Figures 2.2A, 2.2B and 2.3C). Volumes were aligned using cross correlation, segmented, and visualized using IMOD (Kremer et al., 1996).

Mouse brain slices: SBEM was performed on a Merlin scanning electron microscope (Zeiss) equipped with a 3View2XP and OnPoint backscatter detector (Gatan). The volume was collected at 2 kV, with 6.8 nm pixels and 70 nm Z steps. Local gas injection (Deerinck et al., 2017) was set to 15% during imaging. The raster size was 10k x 15k and the Z dimension was 659 sections.

Semi-automated segmentation of DAB-labeled *Drosophila* olfactory receptor neuron

The DAB-labeled *Drosophila* ORN was segmented in a semi-automated fashion using the IMOD software to generate the 3D model. The IMOD command line ‘imodauto’ was used for the auto-segmentation by setting thresholds to isolate the labeled cellular structures of interest. Further information about the utilities of ‘imodauto’ can be found in the IMOD manual (http://bio3d.colorado.edu/imod/doc/man/imodauto.html). Auto-segmentation was followed by manual proofreading and reconstruction by two independent proofreaders. The proofreaders used elementary operations in IMOD, most commonly the ‘drawing tools’ to correct the contours generated by ‘imodauto’. Where ‘imodauto’ failed to be applied successfully, the proofreaders also used the ‘drawing tools’ to directly trace the outline of the labeled structure. The contours of ORNs generally do not vary markedly between adjacent sections. Therefore, alternate sections were traced for the reconstruction of some parts of the ORN dendrite.

Quantification of fluorescence intensity

To quantify GFP fluorescence intensity shown in Figure 2.4, maximum intensity Z-projections were generated using ImageJ (NIH). Average fluorescence intensity in the background was subtracted from the fluorescence intensity of each cell body measured. Only non-overlapping cell bodies were quantified. Kolmogorov-Smirnov Test was performed on http://www.physics.csbsju.edu/stats/KS-test.html and Mann-Whitney *U* Test was performed using SigmaPlot 13.0 (Systat Software, San Jose, CA).

Light and electron microscope volume registration

To target tdTomato-expressing cells in the mouse brain for SBEM imaging, the confocal volumes collected in the frozen-rehydrated specimen was registered with the microCT volume of the resin-embedded sample, using a software tool developed in our lab. The resin-embedded specimen was then mounted and trimmed for SBEM based on the microCT volume. A second microCT scan of the mounted specimen allowed for precise targeting of the cells of interest with the Gatan stage for SBEM. After the SBEM volume was collected, the confocal and SBEM volumes were registered using the landmark tool of Amira 6.3 (ThermoFisher, Waltham, MA). Heterochromatin structures revealed by DRAQ5 labeling and visible in the SBEM volume were used as landmark points for the registration.

Chapter 2, in part, is a reprint of the material as it appears in High-quality ultrastructural preservation using cryofixation for 3D electron microscopy of genetically labeled tissues 2018. Tsang, Tin Ki; Bushong, Eric A.; Boassa, Daniela; Hu, Junru; Romoli, Benedetto; Phan, Sabastien; Dulcis, Davide; Su, Chih-Ying; Ellisman, Mark H., eLife, 7, e35524, 2018. The dissertation author and Eric A. Bushong contributed equally to this paper as primary investigators and authors.

Table 2.1. Comparison of the advantages and limitations of different sample preparation methods for electron microscopy.
The CryoChem Method (CCM) combines the advantages of chemical fixation and cryofixation. With CCM, samples are fixed with high-pressure freezing and freeze-substitution to achieve quality ultrastructural preservation. This approach allows preservation of tissues with cuticle or cell wall and captures biological events with high temporal resolution. A rehydration step is introduced to enable fluorescence imaging, DAB labeling by genetically encoded EM tags and high-contrast *en bloc* heavy metal staining of the cryofixed sample. The high-contrast *en bloc* heavy metal staining permitted by CCM reduces the need for post-staining on sections, and makes CCM compatible with serial block-face scanning electron microscopy (SBEM). Common limitations of chemical fixation and cryofixation are denoted in red.

	Chemical fixation	Cryofixation	CryoChem
Fixation	Aldehyde fixatives (4 °C)	1) High-pressure freezing (-196 °C, ~2100 bar) 2) Freeze-substitution in organic solvents	1) High-pressure freezing (-196 °C, ~2100 bar) 2) Freeze-substitution in organic solvents
Ultrastructural preservation	Fair	Excellent	Excellent
Tissues with cuticle or cell wall	Incompatible	Compatible	Compatible
Temporal resolution of events captured	Low	High	High
Hydration state of the sample	Hydrated	Dehydrated after freeze-substitution	Hydrated after rehydration
Fluorescence imaging after fixation	Compatible	Generally incompatible	Compatible
DAB labeling by genetic EM tags	Compatible	Incompatible due to dehydration	Compatible due to rehydration
High-contrast *en bloc* heavy metal staining	Compatible	Limited	Compatible due to rehydration
Post-staining on sections	Optional	Often required	Optional
SBEM compatibility	Compatible	Incompatible	Compatible

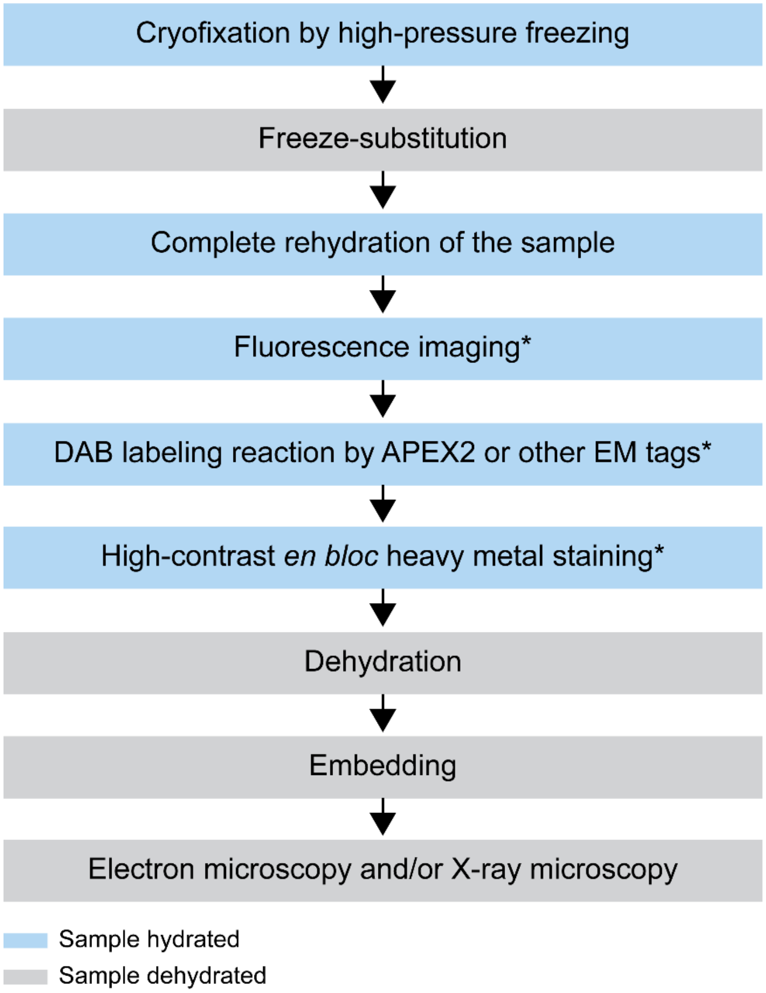

Figure 2.1. Flowchart of the CryoChem method.
After cryofixation by high-pressure freezing and freeze-substitution, cryofixed samples are rehydrated gradually. Rehydrated samples can then be imaged for fluorescence, subjected to DAB labeling reaction or *en bloc* stained with a substantial amount of heavy metals. The protocol is modular; the first three processes are the core steps of CCM and the starred steps are optional depending on the experimental design. The samples are then dehydrated for resin infiltration and embedding, followed by imaging with any EM technique of choice. Blue and grey denote hydrated and dehydrated states of the sample, respectively.

Figure 2.2. CryoChem Method offers high-quality ultrastructural preservation and sufficient *en bloc* staining for SBEM.

EM images were acquired to assess the morphology of CCM-processed tissues. (A-B) The quality of preservation was markedly improved in the CCM-processed *Drosophila* antenna compared to the chemically fixed counterpart. Pixel resolution of SBEM images (x,y): 6.5 nm. (A1 and B1) Unlike the CCM-processed antenna, the chemically fixed antenna showed signs of extraction (arrow) and disorganized membranes. ORN: olfactory receptor neuron; ML: microlamella. Scale bars: 1 µm. (A2 and B2) The microlamellae were well-preserved in the CCM-processed antenna, compared to the chemically fixed samples. Scale bars: 1 µm. (A3 and B3) In the enlarged views of the boxed regions, the microlamellae in the CCM-processed antenna appeared uniform in size and shape, unlike the chemically fixed ones which were distorted. Scale bars: 200 nm. (C-D) CCM enhanced the morphological preservation of aldehyde-perfused mouse brain. The initial dehydration in standard EM preparation took place on ice for 1 hour, but it occurred during freeze-substitution at -90 °C to -30 °C for over 5 days in CCM processing. (C1 and D1) The smoothness of membranes was improved by CCM processing. ST: synaptic terminal. Scale bars: 200 nm. Pixel resolution of TEM images (x,y): 1.92 nm. (C2 and D2) The preservation of nuclear envelopes was improved by CCM processing. N: nucleus. Scale bars: 500 nm. Pixel resolution (x,y): 2.88 nm. (C3 and D3) In the enlarged views of the boxed regions, the nuclear envelopes (NE; arrows) appeared smoother and the cytoplasmic density (asterisk) was increased with CCM processing. We note that the chromatin was more heavily stained in the CCM-processed specimen, likely due to the additional exposure to uranyl acetate during freeze-substitution. Scale bars: 100 nm. Pixel resolution (x,y): 1.14 nm.

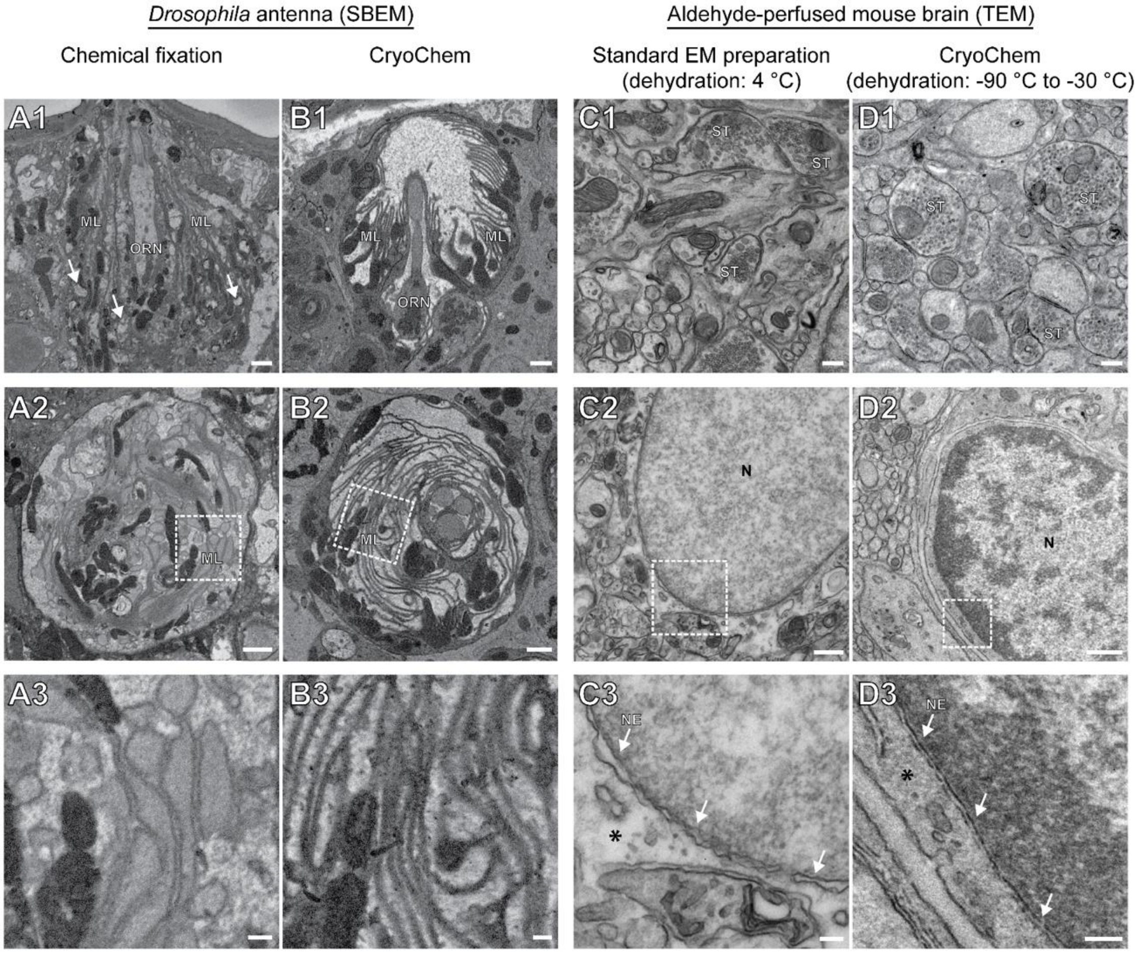
Drosophila antenna (SBEM)
Aldehyde-perfused mouse brain (TEM)
Chemical fixation
CryoChem
Standard EM preparation
(dehydration: 4 °C)
CryoChem
(dehydration: -90 °C to -30 °C)
A1
ML
ORN
ML
B1
ML
ML
ORN
C1
ST
ST
ST
D1
ST
ST
ST
A2
ML
B2
ML
C2
N
D2
N
A3
B3
C3
NE
*
D3
NE
*

Figure 2.3. CryoChem method enables DAB labeling by APEX2 in cryofixed tissues. In the CCM-processed cultured cells and *Drosophila* antennae, DAB labeling was observed in cells expressing APEX2. (A) Flowchart for DAB labeling of target structures expressing APEX2 in CCM-processed samples. In our experiments, the cultured cells were imaged with TEM and the *Drosophila* antennae were imaged with X-ray microscopy, followed by SBEM. (B) Mitochondria in HEK 293T cell transfected with Mito-APEX2 were labeled with DAB (bottom panel), in contrast to an untransfected control cell (top panel). Scale bars: 200 nm. Pixel resolution (x,y): 3.97 nm (top panel); 2.88 nm (bottom panel). (C) An APEX2-expressing olfactory receptor neuron (ORN) was labeled with DAB (arrow) in the *Drosophila* antenna (*10XUAS-myc-APEX2-Orco; Or47b-GAL4*). Asterisks denote ORNs without APEX2 expression. Scale bar: 500 nm. Pixel resolution of SBEM images (x,y): 6.5 nm. (D) A series of SBEM images showing the same DAB labeled *Drosophila* ORN (arrow) in different planes of section. Asterisks denote ORNs without APEX2 expression. The images were acquired using standard imaging methods without charge compensation by nitrogen gas injection (Deerinck et al., 2017). These images, together with the rest of the EM volume acquired using SBEM, enabled semi-automatic segmentation and 3D reconstruction of the labeled ORN (right panel). Scale bars: 500 nm for SBEM images, 2 µm for the 3D model of ORN. SBEM imaging parameters: Z step: 50 nm; Z dimension: 1200 sections; raster size: 12k x 9k; pixel size: 3.8 nm.

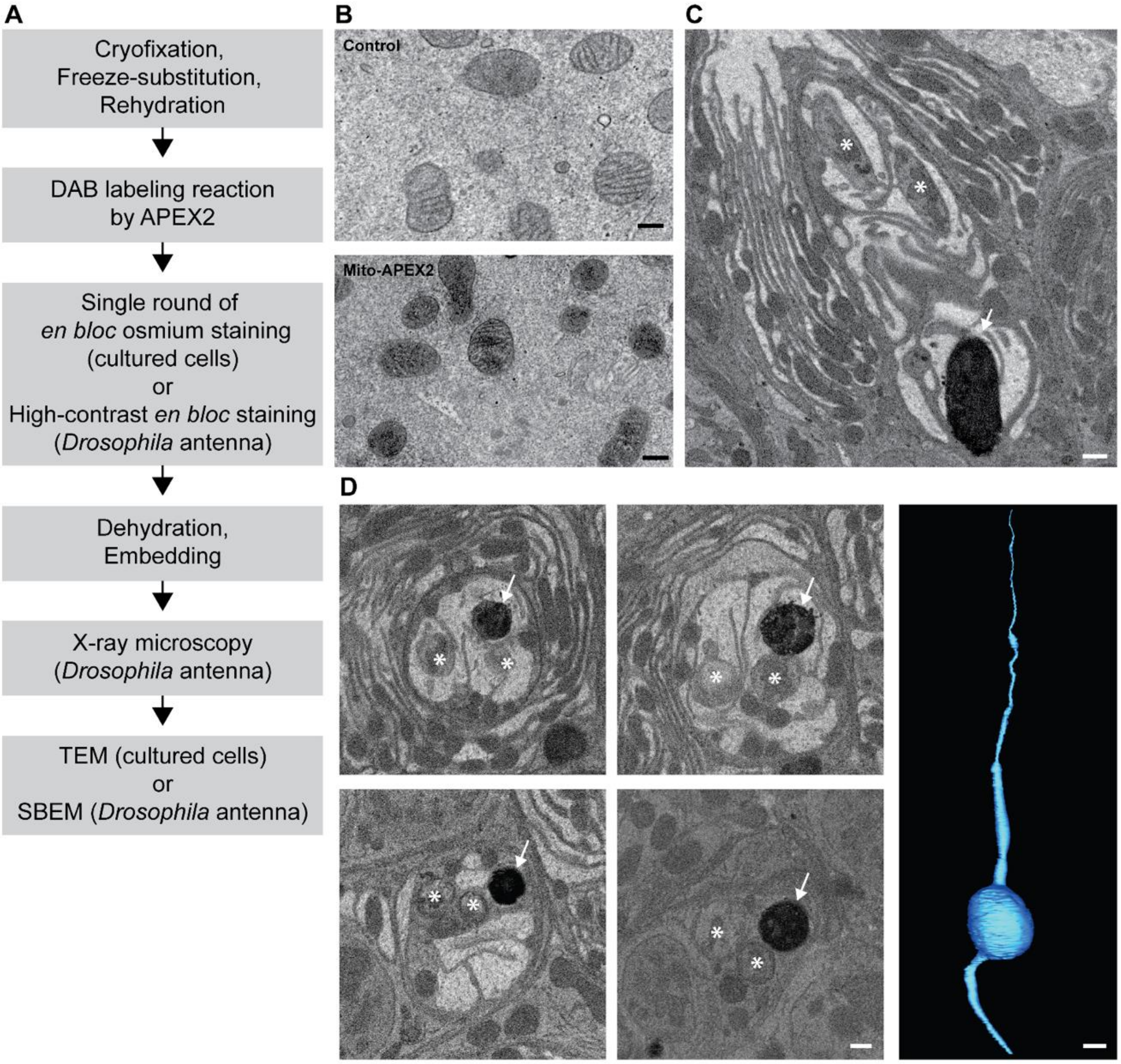
A
Cryofixation, Freeze-substitution, Rehydration
DAB labeling reaction by APEX2
Single round of *en bloc* osmium staining (cultured cells) or High-contrast *en bloc* staining (*Drosophila* antenna)
Dehydration, Embedding
X-ray microscopy (*Drosophila* antenna)
TEM (cultured cells) or SBEM (*Drosophila* antenna)
B
Control
Mito-APEX2
C
D

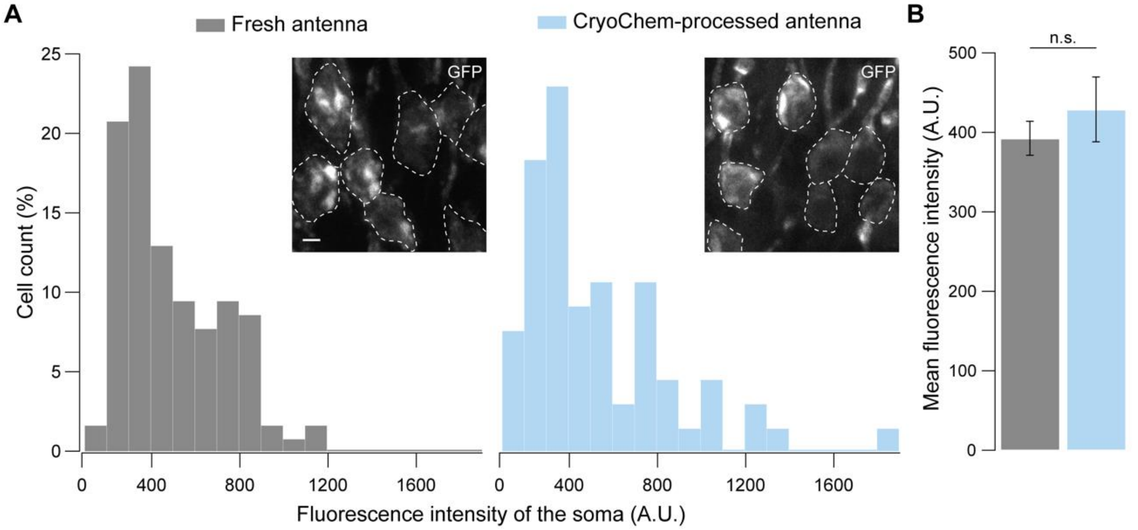

Figure 2.4. GFP fluorescence is well-preserved in CryoChem-processed samples. Confocal images were taken to quantify the level of GFP fluorescence in *Drosophila* ORNs. Antennae were collected from transgenic flies expressing GFP in a subset of ORNs. (A) GFP fluorescence intensity distributions of the ORN soma in the freshly-dissected, unfixed antennae (left panel) and the CCM-processed antennae (right panel) are not significantly different. *p*=0.810, Kolmogorov-Smirnov test. Insets show representative images, with ORN soma outlined. Scale bar: 2 µm. (B) Comparison of the average fluorescence intensities. GFP intensities are virtually identical between neurons in the unfixed antennae and the frozen-rehydrated antennae. n= 3 antennae, Error bars denote SEM, *p*=0.950, Mann-Whitney *U* Test.

Figure 2.5. 3D correlated light and electron microscopy (CLEM) in CCM-processed mouse brain. Mouse brain slices with fluorescently labeled neurons were processed with CCM, imaged with confocal microscopy, X-ray microscopy and SBEM for 3D CLEM. (A) Flowchart for performing 3D CLEM with CCM-processed samples. Similar to a typical CCM protocol, cryofixed samples are first freeze-substituted and rehydrated. The frozen-rehydrated sample is then stained with DRAQ5 to label DNA in the nuclei. Next, the region of interest (ROI) is identified using confocal microscopy based on fluorescent signals, while the DRAQ5 signals are also acquired to serve as fiducial markers. Subsequently, the sample is stained, dehydrated and embedded for X-ray microscopy and SBEM. Using the DRAQ5 signals as fiducial markers, the confocal volumes can be registered to the X-ray volume such that the ROI for SBEM can be identified. Once the SBEM volume is acquired, it can be registered to the confocal volumes based on the positions of the nuclei for 3D CLEM. (B) An example of the DRAQ5 fluorescence signals (left), the corresponding ROI in X-ray volume (middle) and the overlay (right). This image registration process facilitates ROI identification in SBEM. Scale bar: 20 µm. (C) DRAQ5 fluorescence labeling served as fiducial points for registering the confocal volume to the SBEM volume. Scale bar: 5 µm. (D) The cell body of a tdTomato-expressing neuron (left) was identified in the SBEM volume (middle) through CLEM (right). (E) Neuronal processes expressing tdTomato (left) were also identified in the SBEM volume (middle) through CLEM (right). Scale bars: 2 µm, for both (D) and (E). SBEM imaging parameters: Z step: 70 nm; Z dimension: 695 sections; raster size: 10k x 15k; pixel size: 6.8 nm.

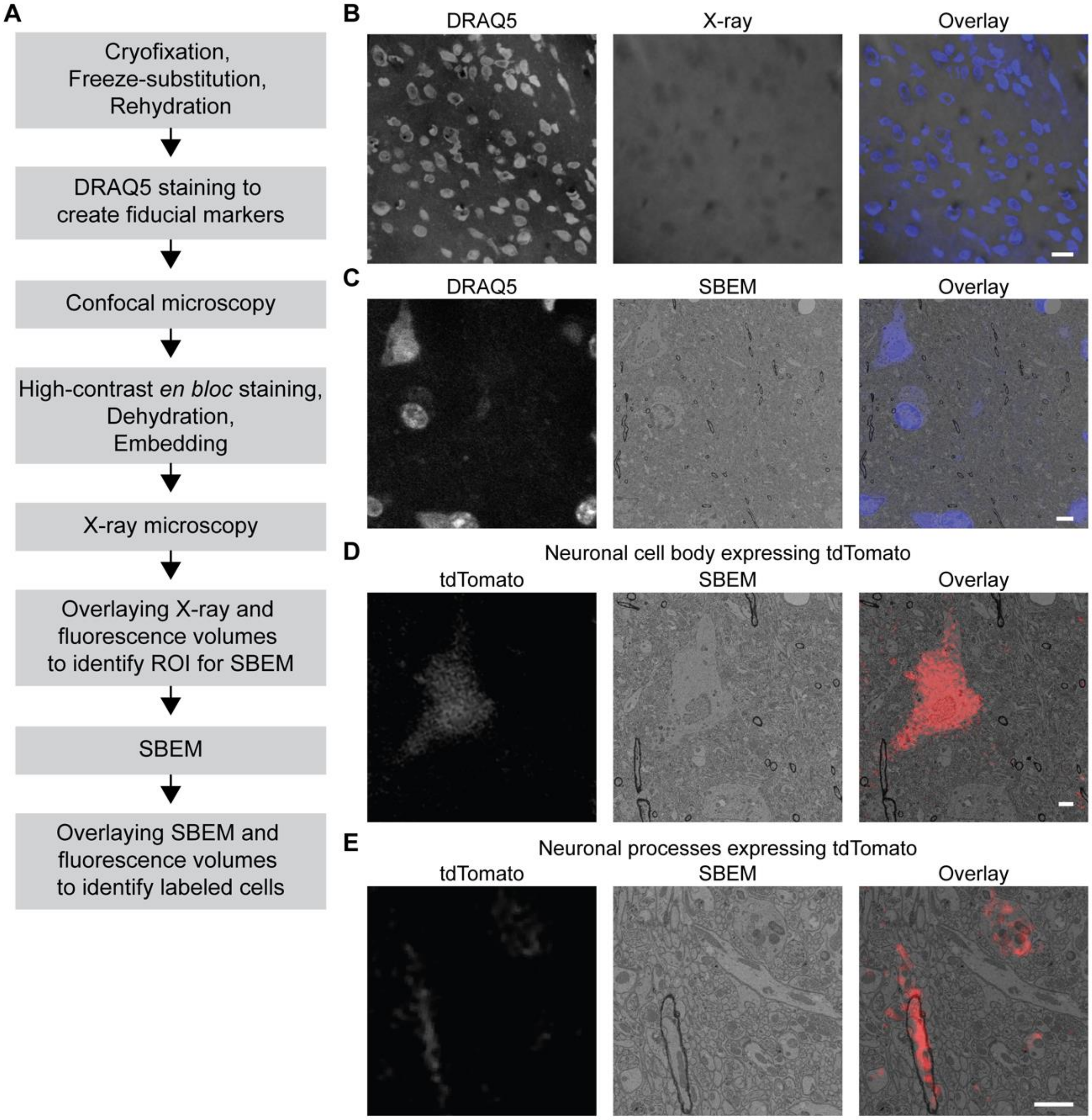
A
Cryofixation,
Freeze-substitution,
Rehydration
DRAQ5 staining to create fiducial markers
Confocal microscopy
High-contrast en bloc staining,
Dehydration,
Embedding
X-ray microscopy
Overlaying X-ray and fluorescence volumes to identify ROI for SBEM
SBEM
Overlaying SBEM and fluorescence volumes to identify labeled cells
B
DRAQ5
X-ray
Overlay
C
DRAQ5
SBEM
Overlay
D
Neuronal cell body expressing tdTomato
tdTomato
SBEM
Overlay
E
Neuronal processes expressing tdTomato
tdTomato
SBEM
Overlay

2.6 References

Briggman, K. L., & Bock, D. D. (2012). Volume electron microscopy for neuronal circuit reconstruction. Current Opinion in Neurobiology, *22*, 154–161.

Brown, E., Mantell, J., Carter, D., Tilly, G., & Verkade, P. (2009). Studying intracellular transport using high-pressure freezing and correlative light electron microscopy. Seminars in Cell and Developmental Biology, *20*, 910–919.

Bushong, E. A., Johnson, D. D., Kim, K.-Y., Terada, M., Hatori, M., Peltier, S. T., Panda, S., Merkle, A., Ellisman, M. H. (2015). X-Ray microscopy as an approach to increasing accuracy and efficiency of serial block-face imaging for correlated light and electron microscopy of biological specimens. Microscopy and Microanalysis, *21*, 231–238.

Dahl, R., & Staehelin, L. A. (1989). High-pressure freezing for the preservation of biological structure: Theory and practice. Journal of Electron Microscopy Technique, *13*, 165–174.

de Boer, P., Hoogenboom, J. P., & Giepmans, B. N. G. (2015). Correlated light and electron microscopy: Ultrastructure lights up! Nature Methods, *12*, 503–513.

Deerinck, T., Bushong, E., Lev-Ram, V., Shu, X., Tsien, R., & Ellisman, M. (2010). Enhancing serial block-face scanning electron microscopy to enable high resolution 3-D nanohistology of cells and tissues. Microscopy and Microanalysis, *16*, 1138–1139.

Deerinck, T. J., Shone, T. M., Bushong, E. A., Ramachandra, R., Peltier, S. T., & Ellisman, M. H. (2017). High-performance serial block-face SEM of nonconductive biological samples enabled by focal gas injection-based charge compensation. Journal of Microscopy, *270*, 142-149.

Denk, W., & Horstmann, H. (2004). Serial block-face scanning electron microscopy to reconstruct three-dimensional tissue nanostructure. PLoS Biology, *2*, e329.

Dhonukshe, P., Aniento, F., Hwang, I., Robinson, D. G., Mravec, J., Stierhof, Y. D., & Friml, J. (2007). Clathrin-mediated constitutive endocytosis of PIN auxin efflux carriers in Arabidopsis. Current Biology, *17*, 520–527.

Ding, R. (1993). Three-dimensional reconstruction and analysis of mitotic spindles from the yeast, Schizosaccharomyces pombe. The Journal of Cell Biology, *120*, 141–151.

Dobritsa, A. A, van der Goes van Naters, W., Warr, C. G., Steinbrecht, R. A., & Carlson, J. R. (2003). Integrating the molecular and cellular basis of odor coding in the Drosophila antenna. Neuron, *37*, 827–41.

Doroquez, D. B., Berciu, C., Anderson, J. R., Sengupta, P., & Nicastro, D. (2014). A high-resolution morphological and ultrastructural map of anterior sensory cilia and glia in Caenorhabditis elegans. eLife, *2014*, 1–35.

Ellisman, M. H., Deerinck, T. J., Kim, K. Y., Bushong, E. A., Phan, S., Ting, A. Y., & Boassa, D. Advances in molecular probe-based labeling tools and their application to multiscale multimodal correlated microscopies. Journal of Chemical Biology, *8*, 143-151.

Fishilevich, E., & Vosshall, L. B. (2005). Genetic and functional subdivision of the Drosophila antennal lobe. Current Biology, *15*, 1548–53.

Gaietta, G., Deerinck, T. J., Adams, S. R., Bouwer, J., Tour, O., Laird, D. W., Sosinsky, G. E., Tsien, R. Y., Ellisman, M. H. (2002). Multicolor and electron microscopic imaging of connexin trafficking. Science, *296*, 503–507.

Groth, A. C., Fish, M., Nusse, R., & Calos, M. P. (2004). Construction of transgenic Drosophila by using the site-specific integrase from phage ΦC31. Genetics, *166*, 1775–1782.

Hess, M. W., Müller, M., Debbage, P. L., Vetterlein, M., & Pavelka, M. (2000). Cryopreparation provides new insight into the effects of brefeldin A on the structure of the HepG2 Golgi apparatus. Journal of Structural Biology, *130*, 63–72.

Joesch, M., Mankus, D., Yamagata, M., Shahbazi, A., Schalek, R., Suissa-Peleg, A., Meister, M., Lichtman, J. W., Scheirer, W. J., Sanes, J. R. (2016). Reconstruction of genetically identified neurons imaged by serial-section electron microscopy. eLife, *5*, 1-13.

Kaeser, W., Koyro, H. -W, & Moor, H. (1989). Cryofixation of plant tissues without pretreatment. Journal of Microscopy, *154*, 279–288.

Kellenberger, E., Johansen, R., Maeder, M., Bohrmann, B., Stauffer, E., & Villiger, W. (1992). Artefacts and morphological changes during chemical fixation. Journal of Microscopy, *168*, 181–201.

Kelley, R. O., Dekker, R. A. F., & Bluemink, J. G. (1973). Ligand-mediated osmium binding: Its application in coating biological specimens for scanning electron microscopy. Journal of Ultrasructure Research, *45*, 254–258.

Kessler, M. A, Yang, M., Gollomp, K. L., Jin, H., & Iacovitti, L. (2003). The human tyrosine hydroxylase gene promoter. Molecular Brain Research, *112*, 8–23.

Kiss, J. Z., Giddings, T. H., Staehelin, L. A., & Sack, F. D. (1990). Comparison of the ultrastructure of conventionally fixed and high pressure frozen/freeze substituted root tips of Nicotiana and Arabidopsis. Protoplasma, *157*, 64–74.

Kolotuev, I., Schwab, Y., & Labouesse, M. (2010). A precise and rapid mapping protocol for correlative light and electron microscopy of small invertebrate organisms. Biology of the Cell, *102*, 121–132.

Korogod, N., Petersen, C. C. H., & Knott, G. W. (2015). Ultrastructural analysis of adult mouse neocortex comparing aldehyde perfusion with cryo fixation. eLife, *4*, 1–17.

Kremer, J. R., Mastronarde, D. N., & McIntosh, J. R. (1996). Computer visualization of three-dimensional image data using IMOD. Journal of Structural Biology, *116*, 71–76.

Kukulski, W., Schorb, M., Welsch, S., Picco, A., Kaksonen, M., & Briggs, J. A. G. (2011). Correlated fluorescence and 3D electron microscopy with high sensitivity and spatial precision. Journal of Cell Biology, *192*, 111–119.

Kushida, H. (1962). A study of cellular swelling and shrinkage during fixation, dehydration and embedding in various standard media. Journal of Electron Microscopy, *11*, 135–138.

Lam, S. S., Martell, J. D., Kamer, K. J., Deerinck, T. J., Ellisman, M. H., Mootha, V. K., & Ting, A. Y. (2015). Directed evolution of APEX2 for electron microscopy and proximity labeling. Nature Methods, *12*, 51–54.

Leapman, R. D. (2004). Novel techniques in electron microscopy. Current Opinion in Neurobiology, *14*, 591–598.

Markstein, M., Pitsouli, C., Villalta, C., Celniker, S. E., & Perrimon, N. (2008). Exploiting position effects and the gypsy retrovirus insulator to engineer precisely expressed transgenes. Nature Genetics, *40*, 476–483.

Martell, J. D., Deerinck, T. J., Sancak, Y., Poulos, T. L., Mootha, V. K., Sosinsky, G. E., … Ting, A. Y. (2012). Engineered ascorbate peroxidase as a genetically encoded reporter for electron microscopy. Nature Biotechnology, *30*, 1143–8.

McDonald, K. (1999). High-pressure freezing for preservation of high resolution fine structure and antigenicity for immunolabeling. In *Electron Microscopy Methods and Protocols* (Vol. 117, pp. 77–98). New Jersey: Humana Press.

McDonald, K. (2007). Cryopreparation methods for electron microscopy of selected model systems. *Methods in Cell Biology*.

McDonald, K. (2009). A review of high-pressure freezing preparation techniques for correlative light and electron microscopy of the same cells and tissues. Journal of Microscopy, *235*, 273–281.

Moor, H. (1987). Theory and practice of high pressure freezing. In R. A. Steinbrecht & K. Zierold (Eds.), *Cryotechniques in Biological Electron Microscopy* (pp. 175–191). Berlin, Heidelberg: Springer Berlin Heidelberg.

Müller-Reichert, T., Hohenberg, H., O'Toole, E. T., & Mcdonald, K. (2003). Cryoimmobilization and three-dimensional visualization of C. elegans ultrastructure. Journal of Microscopy, *212*, 71–80.

Ng, J., Browning, A., Lechner, L., Terada, M., Howard, G., Jefferis, G. S. X. E. (2016). Genetically targeted 3D visualisation of Drosophila neurons under electron microscopy and X-Ray microscopy using miniSOG. Scientific Reports, *6*, 38863.

Ngo, J. T., Adams, S. R., Deerinck, T. J., Boassa, D., Rodriguez-Rivera, F., Palida, S. F., Carolyn, R. B., Ellisman, M. H., Tsien, R. Y. (2016). Click-EM for imaging metabolically tagged nonprotein biomolecules. Nature Chemical Biology, *12*, 459–465.

Nixon, S. J., Webb, R. I., Floetenmeyer, M., Schieber, N., Lo, H. P., Parton, R. G. (2009). A single method for cryofixation and correlative light, electron microscopy and tomography of zebrafish embryos. Traffic, *10*, 131–136.

Ou, H. D., Phan, S., Deerinck, T. J., Thor, A., Ellisman, M. H., O'Shea, C. C. (2017). ChromEMT: Visualizing 3D chromatin structure and compaction in interphase and mitotic cells. Science, *357*, eaag0025.

Ripper, D., Schwarz, H., & Stierhof, Y.-D. (2008). Cryo-section immunolabelling of difficult to preserve specimens: advantages of cryofixation, freeze-substitution and rehydration. Biology of the Cell, *100*, 109–123.

Ryan, K., Lu, Z., Meinertzhagen, I. A. (2016). The CNS connectome of a tadpole larva of Ciona intestinalis (L.) highlights sidedness in the brain of a chordate sibling. eLife, *5*, 1–34.

Sabatini, D. D. (1963). Cytochemistry and electron microscopy: The preservation of cellular ultrastructure and enzymatic activity by aldehyde fixation. The Journal of Cell Biology, *17*, 19–58.

Schwarz, H., Humbel, B. (2009). Correlative light and electron microscopy. In A. Cavalier, D. Spehner, B. Humbel (Eds.), *Handbook of cryo-preparation methods for electron microscopy.* (pp. 537–565). CRC Press.

Shanbhag, S. R., Müller, B., Steinbrecht, R. A. (1999). Atlas of olfactory organs of Drosophila melanogaster 1. Types, external organization, innervation and distribution of olfactory sensilla. International Journal of Insect Morphology and Embryology, *28*, 377–397.

Shanbhag, S. R., Müller, B., Steinbrecht, R. A. (2000). Atlas of olfactory organs of Drosophila melanogaster 2. Internal organization and cellular architecture of olfactory sensilla. Arthropod Structure & Development, *29*, 211–229.

Shimoni, E., Müller, M., Mueller, M. (1998). On optimizing high-pressure freezing: from heat transfer theory to a new mircrobiopsy device. Journal of Microscopy, *192*, 236–247.

Shu, X., Lev-Ram, V., Deerinck, T. J., Qi, Y., Ramko, E. B., Davidson, M. W., Jin, Y., Ellisman, M. H., Tsien, R. Y. (2011). A genetically encoded tag for correlated light and electron microscopy of intact cells, tissues, and organisms. PLoS Biology, *9*, e1001041.

Sosinsky, G. E., Crum, J., Jones, Y. Z., Lanman, J., Smarr, B., Terada, M., Martone, M. E., Deerinck, T. J., Johnson, J. E., Ellisman, M. H. (2008). The combination of chemical fixation procedures with high pressure freezing and freeze substitution preserves highly labile tissue ultrastructure for electron tomography applications. Journal of Structural

Biology, *161*, 359–371.

Steinbrecht, R. A. (1980). Cryofixation without cryoprotectants. Freeze substitution and freeze etching of an insect olfactory receptor. Tissue and Cell, *12*, 73–100.

Steinbrecht, R. A., Müller, M. (1987). Freeze-substitution and freeze-drying. In R. A. Steinbrecht & K. Zierold (Eds.), *Cryotechniques in Biological Electron Microscopy* (pp. 149–172). Berlin, Heidelberg: Springer Berlin Heidelberg.

Stierhof, Y. D., & El Kasmi, F. (2010). Strategies to improve the antigenicity, ultrastructure preservation and visibility of trafficking compartments in Arabidopsis tissue. European Journal of Cell Biology, *89*, 285–297.

Szczesny, P. J., Walther, P., Müller, M. (1996). Light damage in rod outer segments: The effects of fixation on ultrastructural alterations. Current Eye Research, *15*, 807–814.

Takemura, S., Bharioke, A., Lu, Z., Nern, A., Vitaladevuni, S., Rivlin, P. K., … Chklovskii, D. B. (2013). A visual motion detection circuit suggested by Drosophila connectomics. Nature, *500*, 175–181.

Tapia, J. C., Kasthuri, N., Hayworth, K. J., Schalek, R., Lichtman, J. W., Smith, S. J., Buchanan, J. (2012). High-contrast en bloc staining of neuronal tissue for field emission scanning electron microscopy. Nature Protocols, *7*, 193–206.

van Donselaar, E., Posthuma, G., Zeuschner, D., Humbel, B. M., Slot, J. W. (2007). Immunogold labeling of cryosections from high-pressure frozen cells. Traffic, *8*, 471–485.

Wang, J.-W., Beck, E. S., & McCabe, B. D. (2012). A modular toolset for recombination transgenesis and neurogenetic analysis of Drosophila. PloS One, *7*, e42102.

Watanabe, S., Davis, M. W., & Jorgensen, E. M. (2014a). Flash-and-freeze electron microscopy: coupling optogenetics with high-pressure freezing. In U. V. Nägerl & A. Triller (Eds.), *Nanoscale Imaging of Synapses. Neuromethods* (pp. 43–57). New York, NY: Humana Press.

Watanabe, S., Liu, Q., Davis, M. W., Hollopeter, G., Thomas, N., Jorgensen, N. B., Jorgensen, E. M. (2013). Ultrafast endocytosis at Caenorhabditis elegans neuromuscular junctions. eLife, *2013*, 1–24.

Watanabe, S., Punge, A., Hollopeter, G., Willig, K. I., Hobson, R. J., Davis, M. W., Hell, S. W., Jorgensen, E. M. (2011). Protein localization in electron micrographs using fluorescence nanoscopy. Nature Methods, *8*, 80–84.

Watanabe, S., Rost, B. R., Camacho-Pérez, M., Davis, M. W., Söhl-Kielczynski, B., Rosenmund, C., Jorgensen, E. M. (2013). Ultrafast endocytosis at mouse hippocampal synapses. Nature, *504*, 242–247.

Watanabe, S., Trimbuch, T., Camacho-Pérez, M., Rost, B. R., Brokowski, B., Söhl-

Kielczynski, B., Felies, A., Davis, M. W., Rosenmund, C., Jorgensen, E. M. (2014b). Clathrin regenerates synaptic vesicles from endosomes. Nature, *515*, 228–233.

West, J. B., Fu, Z., Deerinck, T. J., Mackey, M. R., Obayashi, J. T., Ellisman, M. H. (2010). Structure-function studies of blood and air capillaries in chicken lung using 3D electron microscopy. Respiratory Physiology and Neurobiology, *170*, 202–209.

Williams, M. E., Wilke, S. A., Daggett, A., Davis, E., Otto, S., Ravi, D., Ripley, B., Bushong, E. A., Ellisman, M. H., Klein, G., Ghosh, A. (2011). Cadherin-9 regulates synapse-specific differentiation in the developing hippocampus. Neuron, *71*, 640–655.

Winey, M., Mamay, C. L., O'Toole, E. T., Mastronarde, D. N., Giddings, T. H., McDonald, K. L., McIntosh, J. R. (1995). Three-dimensional ultrastructural analysis of the Saccharomyces cerevisiae mitotic spindle. Journal of Cell Biology, *129*, 1601–1615.

Zheng, Z., Lauritzen, J. S., Perlman, E., Robinson, C. G., Nichols, M., Milkie, D., … Bock, D. D. (2017). A complete electron microscopy volume of the brain of adult Drosophila melanogaster. bioRxiv.

Chapter 3: Morphometric disparities between grouped olfactory receptor neurons that exhibit asymmetric ephaptic inhibition

3.1 Abstract

Olfactory receptor neurons (ORNs) housed in the same sensory hair in *Drosophila* can inhibit each other non-synaptically. In the larger project that this chapter belongs to, we provided experimental evidence that direct electrical interactions, or ephaptic interactions, are sufficient to mediate lateral inhibition between ORNs. Furthermore, our systematic electrophysiological survey showed that neighboring ORNs have different electrotonic properties in most sensilla, indicating that ephaptic interactions between these neurons are asymmetric. The focus of this chapter is to address the mechanism that underlies this asymmetry. Our 3D electron microscopic analysis of genetically identified ORNs reveals that the physically larger ORN in a pair corresponds to the dominant neuron in ephaptic interactions. This is in agreement with our electrical circuit model that takes into account the morphometric differences between compartmentalized ORNs. Together, our findings reveal the asymmetric nature of this circuit interaction, bringing functional insights into how information is processed in the first neurons of an insect olfactory circuit.

3.2 Introduction

Using *Drosophila*'s olfactory system, *Su et al.* showed that ORNs housed in the same sensillum can directly inhibit each other non-synaptically and this inhibition is likely mediated by ephaptic interactions (Su et al., 2012). Across many insect species, including *Drosophila*, olfactory receptor neurons (ORNs) grouped in individual sensilla are known to exhibit distinct and stereotypical extracellular spike amplitudes (de Bruyne et al., 2001a; Connell, 1985; Harraca et al., 2009; Kaissling, 1996; Lu et al., 2007; Su et al., 2009). The ORNs are named “A”, “B”, “C” or “D” based on their relative spike amplitudes in descending order (de Bruyne et al., 2001a; Su et al., 2009). Little is known about whether the stereotypical differences in spike amplitudes of the grouped ORNs indicate any functional differences of the neurons in the context of the non-synaptic lateral inhibition in the sensillum.

The research presented in this chapter is part of a larger study that addressed this question. The other primary author of the study, Ye Zhang, used single sensillum recording experiments to provide direct experimental support that ephaptic interaction is sufficient to drive lateral inhibition between grouped ORNs. In a systematic electrophysiological survey, she found that the majority of the “A” neurons can exert greater ephaptic influence onto their small-spike neighbors, indicating that ephaptic interactions are asymmetric in most sensilla. Specifically, she showed that most “A” neurons can cause a larger maximal reduction of the transepithelial potential, measured as the change in local field potential (ΔLFP), than their small-spike neighbors. She also demonstrated that most “A” neurons have a lower tendency to reduce their spike rates in response to a reduction of the transepithelial potential, as indicated by a smaller spike/LFP ratio, compared to the small-spike neighbors. Collectively, these results suggest that the “A” neurons have smaller input resistances than “B” neurons. Furthermore, using odorant receptor (OR) swapping and OR overexpression experiments, she showed that the smaller near-saturated LFP responses of the “B” ORNs do not arise from their specific OR identities nor a lower receptor density. Therefore, we hypothesize that the asymmetry of ephaptic interactions arises from the distinct electrotonic properties of the grouped ORNs due to their morphological differences. The current chapter tests this hypothesis.

Electron microscopy (EM) studies in a broad range of insect species showed that ORNs housed in the same olfactory sensillum indeed have different dendritic diameters (Gnatzy et al., 1984; Hallberg et al., 1994; Keil, 1984; Shanbhag et al., 1999, 2000;

Steinbrecht, 1970; Steinbrecht, 1973; Steinbrecht and Müller, 1976) and soma volumes (Gnatzy et al., 1984). The correlation between dendritic diameter and spike amplitude of ORNs has been demonstrated in the European corn borers, *Ostrinia nubilalis* (Hansson et al., 1994). When the researchers crossed two strains of European corn borers, the spike amplitudes of two neighboring pheromone-sensing ORNs in the F1 hybrids became more similar. Importantly, the dendritic diameters of those ORNs were also more alike in the hybrids. Therefore, this study provided evidence that spike amplitude and dendritic diameter are correlated and possibly determined genetically. Such correlations between spike amplitude and dendritic caliber of ORNs have also been observed in two other moth species, *Bombyx mori* and *Antheraea polyphemus* (Kaissling et al., 1978; Kochansky et al., 1975; Kumar and Keil, 1996).

Previously, the morphology of *Drosophila* ORNs has been characterized in two atlases using serial section transmission electron microscopy (TEM) (Shanbhag et al., 1999, 2000). Based on the size and morphological features, they identified four major morphological classes of sensilla on the *Drosophila* antenna: trichoid, basiconic, intermediate and coeloconic. The trichoid sensilla are the longest ones (~20 µm) on the antenna and they have a unique enlargement in the sensillum base, called the basal drum. The basiconic sensilla are approximately 10 µm long and house ORNs that have the highest number of dendritic branches. The lengths of the intermediate sensilla (12-15 µm) fall between the basiconic and the trichoid sensilla. The intermediate sensilla also house ORNs with branched outer dendrites, albeit with fewer branches. The coeloconic sensilla are the smallest (~5 µm) type on the antenna and their shape resembles short conical pegs. Although these two EM studies offered valuable morphological insights into the olfactory sensilla and ORNs, they did not provide the information necessary for testing our hypothesis. First, the researchers of these studies did not have the genetic tools to assign neuronal identity to the ORNs. Secondly, serial section TEM was so labor-intensive and time-consuming that they needed to discard over half of their sections to keep the workload manageable. Therefore, they were only able to obtain limited 2D morphometric measurements.

To test our hypothesis, we performed morphometric analysis of genetically identified ORNs using serial block-face scanning electron microscopy (SBEM) (Denk and Horstmann, 2004). We acquired image volumes of antennae processed using the CryoChem method (Tsang et al., 2018). Though SBEM has a lower (6-10 nm) resolution than TEM (subnanometer) (Briggman and Bock, 2012; Wanner et al., 2015), the automated nature of its sectioning and imaging procedures makes it more conducive to 3D EM analysis. In the majority of sensilla types examined, we found that the dominant "A" neurons are indeed physically larger than its neighbors. Using the morphometric data, we also revised the circuit model of the sensillum (Vermeulen and Rospars, 2004) to reflect the differences in electrotonic properties between the grouped ORNs. The circuit model was revised by a co-author, Jürgen Reingruber, with input from Chih-Ying Su, Ye Zhang and me. The revised circuit model showed that the asymmetric ephaptic interactions between grouped ORNs can be accounted for by their morphometric disparities. Together, our findings reveal the asymmetric nature of ephaptic interactions between ORNs and provide a biophysical underpinning of the functional asymmetry.

3.3 Results

3.3.1 Morphometric analysis of grouped ORNs

As previously stated, our electrophysiological analysis of grouped ORNs suggests that the large-spike “A” ORNs have smaller input resistances than their neighbors. *Drosophila* ORNs have four main structural sub-compartments: outer (sensory) dendrites, inner (non-sensory) dendrite, soma and axon. We reasoned that a larger surface area and volume of the dendrites and soma would collectively give rise to a smaller input resistance, resulting in the larger maximal LFP response that is characteristic of most “A” neurons. A smaller soma input resistance can also result in a lower spike tendency. Together, these factors can account for the smaller spike/LFP ratio of the “A” neurons. Therefore, we hypothesize that the dominant “A” ORNs are physically larger than their smaller-spike neighbors, with respect to the surface area and volume of their soma and dendrites. We note that in this study, the non-sensory inner dendrite is assumed to be a passive cable of low cytoplasmic resistance that connects the sensory outer dendrite with the soma of an ORN. Since the cytoplasmic resistance of a neuron is typically orders of magnitude less than the membrane resistances of its sensory dendrites and soma (Koch, 2004a; Rospars et al., 2003), the inner dendritic volume is considered as a minor factor in influencing the strength of ephaptic interaction.

To perform the morphometric analysis, we first developed an EM method, named CryoChem, that allows for faithful preservation of genetically labeled ORN structures for SBEM (Tsang et al., 2018). With OR-specific drivers, we expressed a genetic EM marker, APEX2 (enhanced ascorbate peroxidase 2) (Lam et al., 2015; Martell et al., 2012), in select ORNs to render them electron dense through diaminobenzidine (DAB) labeling. As a proof of principle, we first generated 3D reconstructions of at4A (Or47b>APEX2) and at4C (Or88a>APEX2) using SBEM data (Figure 3.1). We identified at4A and at4C as the largest and intermediate-sized neurons in the group of three ORNs, respectively (data not shown), and used this information to assign neuronal identity to the unlabeled ORNs. By comparing the soma and dendritic volumes of the labeled and unlabeled ORNs, our results suggest that DAB labeling does not alter these morphometric features of ORNs (Figure 3.1C).

3.3.2 Dominant “A” ORNs are physically bigger than their neighbors

Next, we expanded our morphometric analysis to a total of four sensilla types (ab3, ab4, at4, ac3II) that exhibited asymmetric ephaptic interactions. These sensilla types represent three of the four major morphological classes of sensilla on the *Drosophila* antenna: antennal basiconic (ab3 and ab4), trichoid (at4) and coeloconic (ac3II). Indeed, the dominant “A” ORNs in all four sensilla types have significantly larger soma volumes than their smaller-spike neighbors (Figure 3.2A-D). This morphometric disparity was observed in every pair of ORNs examined (Figure 3.2A-D). Next, we sought to determine the ORN soma surface area, a critical feature that determines the input resistance of the neuron. Our measurements showed that in ab4, ac3II and at4 sensilla types, the dominant “A” ORNs have significantly larger soma surface areas than their neighboring “B” neurons (Figure 3.2A-D). Though the soma surface areas of ab3A and ab3B ORNs are not statistically different (p=0.119, paired *t* test), this result could be due to the small sample size available in our EM dataset (Figure 3.2A). However, the outer dendritic surface area is also a key factor contributing to the overall input resistance of an ORN. Since the outer dendrites of the ab3 ORNs could not be reconstructed due to technical limitations (see below), we cannot exclude the possibility that a major difference between the ab3A and ab3B ORNs lies in the outer dendritic surface area. Another possibility, which is beyond the scope of this study, is that factors beyond morphology are important for driving asymmetrical inhibition in this pair of ORNs.

Our ability to directly measure the soma surface area from the volume EM data is crucial to the accuracy of this morphometric measurement. It is often assumed that the soma of a neuron is spherical and that the surface area of the soma can be derived from its volume based on this assumption. However, our 3D reconstructions of ORNs revealed that their somas are generally not spherical, as indicated by their sphericity (Figure 3.2A-E). Sphericity is defined as the ratio of the surface area of a sphere of the same volume to the actual surface area of an object (Wadell, 1935). The lower the sphericity, the further the soma deviates from a spherical shape (Figure 3.2A-E). Therefore, if the soma surface area is derived based on the assumption of a spherical object, it would not faithfully represent the actual measurement. This highlights one of the advantages of using volume EM instead of light microscopy to perform morphometric analysis, as light microscopy rarely provides sufficient resolution to accurately determine the surface area of a cellular structure.

Using the 3D reconstructions of the ORN dendrites, we determined that the inner dendritic volumes of the “A” ORNs are significantly larger than those of their small-spike neighbors (Figure 3.3A-D). Due to insufficient DAB labeling or image resolution, we could not accurately reconstruct the fine branches (<100 nm) of the sensory outer dendrites that are tightly packed in ab3 and ab4 sensilla. However, complete outer dendritic reconstruction was possible in the at4 and ac3II sensilla because ORNs housed in the trichoid and coeloconic sensilla have fewer and less complicated outer dendritic branches. Our analysis showed that the “A” ORNs in both sensilla types remain larger in terms of outer dendritic volume (Figure 3.3C and 3.3D). The outer dendritic surface areas of the

"A" ORNs in at4 sensilla are also significantly larger compared to that of the small-spike ORNs (Figure 3.3D). In every pair of ac3II ORNs we reconstructed, the outer dendritic surface areas of the "A" neurons are larger than those of the "B" neurons (Figure 3.3C). Though the differences in the outer dendritic surface areas are not statistically significant (Figure 3.3C), the significantly larger soma surface areas of the ac3IIA ORNs would still result in overall lower input resistances in the large-spike neurons.

To further test our hypothesis, we examined the ab5 ORNs, which exert approximately equal ephaptic influence onto each other (data not shown) and are thus predicted to possess similar morphometric attributes. Indeed, in ab5A and ab5B, we found that their soma and likely also their sensory outer dendrites are similar in size and surface area (Figure 3.2E and 3.3E). Interestingly, the inner dendritic volumes of the "A" ORNs are larger than that of the "B" ORNs (Figure 3.3E). However, the effect of this size disparity on the strength of ephaptic interactions is most likely minimal, as explained above. Together, our morphometric analysis shows that the majority of dominant "A" neurons are larger than their neighbors. The mean values (± standard errors of the mean) of the morphometric measurements made in this study are summarized in Table 3.1.

3.3.3 Novel morphological features of ORNs revealed by the 3D EM reconstructions

Beyond morphometric measurements, our SBEM survey also reveals novel morphological features of the ORNs. For example, we noticed an enlargement of the inner dendrites in every "A" ORN in all three basiconic sensilla types examined (Figure 3.4A). The enlargement is more pronounced in the large basiconic sensilla (ab3) than in the small basiconic sensilla (ab4 and ab5; see inner dendritic volume in Figure 3.3 and Figure 3.4A). This distinct feature of the ORNs in basiconic sensilla is consistent with the finding that the inner dendrites of ab5A were larger than that of ab5B ORNs, despite their otherwise similar sizes (Figure 3.3E). Our 3D reconstructions further revealed a noticeable bend (Figure 3.4B, upper panel) or a complete loop (Figure 3.4B, lower panel) of the outer dendrite at the sensillum base of ab4 sensilla. This bend was found in 50% (2/4) ab4A and 75% (3/4) ab4B ORNs reconstructed and the loop was observed in both ORNs in a separate ab4 sensillum.

The 3D reconstructions also enabled us to examine the outer dendritic branches of the ORNs in detail. In a published atlas of the *Drosophila* antenna EM structure, it was reported that the outer dendrites of ORNs in the coeloconic and trichoid sensilla only occasionally bifurcate near the sensillum tip (Shanbhag et al., 1999). Interestingly, our SBEM datasets of the ORNs revealed a more diverse branching pattern (Figure 3.5A and 3.5B). Amongst the 25% (1/4) ac3A and 75% (3/4) ac3B ORNs that have branched outer dendrites, one ac3B ORN has five branches and the rest of the branched dendrites have two branches (Figure 3.5A). On the other hand, the outer dendrites of 37.5% (3/8) at4A and 37.5% (3/8) at4C ORNs were bifurcated (Figure 3.5B). Unexpectedly, half of these branched outer dendrites bifurcated near the middle of the sensillum, while the rest did so at around the sensillum tip (Figure 3.5B).

We also observed novel branching patterns in the outer dendrites of basiconic sensilla. This finding contradicts the previous observation that the outer dendrites of basiconic sensilla only branched in a restricted region near the sensillum base (Shanbhag et al., 1999). Specifically, in ab5 sensilla, both of the reconstructed ab5A outer dendrites have seven branches and their neighboring ab5B ORNs have three or eleven branches (Figure 3.5C). In all of the ab5 ORNs that we reconstructed, the outer dendrites branched at various locations within the sensilla, including some near the sensillum tip (Figure 3.5C).

The published atlas may have missed the diversity of the outer dendritic branching patterns due to the fact that the researchers selectively discarded over half of the serial transmission electron microscopy sections to keep their workload reasonable (Shanbhag et al., 1999). Our ability to capture these unexpected branching patterns again highlights the power of using 3D EM analysis to study neuronal morphology. Taken together, these novel morphological observations of the inner and outer dendritic compartments demonstrate the diversity in ORN morphologies both between and within sensilla types. Studies to dissect the functional significance of these morphological features will likely be productive avenues of future research.

3.3.4 A revised circuit model of grouped ORNs

Finally, we used mathematical modeling to explain how the morphometric disparity between ORNs contributes to their asymmetric ephaptic interactions. The published electric circuit model of a sensillum assumes that neighboring ORNs have identical passive electrotonic properties (Vermeulen and Rospars, 2004). However, our morphometric analysis suggests otherwise. Therefore, we revised the circuit model to take into account that the input resistance of an ORN is inversely proportional to the surface area of the soma, and the maximal LFP response scales with the surface areas of the sensory dendrite and soma (Figure 3.6A). We focused on the surface areas instead of the volumes of the somas and sensory dendrites because the membrane resistance of a neuron is usually orders of magnitudes larger than its cytoplasmic resistance (Koch, 2004a; Rospars et al., 2003).

In the revised model, the ORN-specific parameters are the odorant sensitivity and the surface areas of soma and sensory dendrite. For the remaining modeling parameters, such as the resting membrane potential and membrane resistivity, identical values were assumed for all ORNs. First, we evaluated our model by simultaneously fitting the LFP responses of the ORNs housed in the ac3II, ab3, ab4 and ab5 sensilla, for which the functional and morphometric data are both available (Figure 3.2 and 3.3, Table 3.1; electrophysiology data not shown), using the *Data2dynamics* framework with a nonlinear least-squares optimization algorithm (Raue et al., 2013, 2015). The fitted dosage curves indicate that the revised circuit model well describes the experimental data (Figure 3.6B1). They also confirm that the larger sizes of the “A” neurons result in higher maximal LFP responses, as evidenced in the fittings of the ac3II, ab3 and ab4 ORNs but not the ab5 ORNs, which are of similar sizes (Figure 3.6B1).

Next we used the model to predict the transmembrane potential of an ORN (V_m) upon activation by a private odorant, corresponding to the fittings shown in Figure 3.6B1. The smaller sizes of the “B” neurons translate into a larger input resistance, thereby allowing for a greater increase in the somatic transmembrane potential of the “B” ORNs in the ac3II, ab3 and ab4 but not ab5 sensilla (Figure 3.6B2). The model also predicts the relationship between ORN depolarization (ΔV_m) and LFP responses in ac3 and ab5 sensilla (Figure 3.6B3). Given that the peak spike response of an ORN is a function of ΔV_m (Nagel and Wilson, 2011), the smaller ΔV_m/LFP slopes of the “A” neurons predicted by the model are consistent with their smaller spike/LFP ratios determined in our electrophysiology experiments (data not shown). Due to the lack of outer dendritic measurements in ab3 and ab4 sensilla (Figure 3.3A and 3.3B), the ΔV_m/LFP slopes are constrained by the experimentally determined spike/LFP ratios. However, incorporating the fitted ΔV_m/LFP slopes enabled us to use the model to predict the sensory dendritic surface areas of ORNs in ab3 and ab4 sensilla. The surface areas of both ab3A and ab4A are predicted to be larger than those of their respective neighbors (Figure 3.6C).

In our model, the differences in the morphometric features and odorant sensitivities are the two parameters that can lead to asymmetric ephaptic interactions between grouped ORNs. To highlight the impact of only the morphometric attributes, we simulated ORN responses in a hypothetical situation where both ORNs in the ab4 sensillum express the same odorant receptor, Or56a. Even with identical odorant sensitivity for both ab4A and ab4B, the larger size of ab4A is sufficient to yield a higher maximal LFP response and a smaller increase in the transmembrane potential (Figure 3.6D). This simulated result generated by the revised circuit model argues for a key role of neuronal size in determining the strength of ephaptic interactions in a sensillum. Given that the odor receptor density and identity do not seem to be key contributors of the asymmetry in the ephaptic interactions (electrophysiology data not shown), the findings from our model strongly suggest that the difference in neuronal size is driving the asymmetry *in vivo*.

3.4 Discussion

We have investigated the mechanistic nature and functional characteristics of lateral inhibition between compartmentalized ORNs in a sensillum. We showed that ephaptic interaction is sufficient to drive lateral inhibition between electrically coupled ORNs housed in the same sensillum. Furthermore, ephaptic interactions between neighboring ORNs are predominantly asymmetric. Strikingly, the sizes of compartmentalized ORNs are similarly distinct; the majority of the dominant “A” neurons are larger than the small-spiked neighbors. In a revised electric circuit model that takes into account the morphometric differences between grouped ORNs, we provided the theoretical basis for arguing that the neuronal size is a key factor contributing to the asymmetry of ephaptic interactions in a sensillum.

3.4.1 Asymmetric interaction in other ephaptic environments

The relationship between neuronal size and the strength of ephaptic interactions determined in this study could help predict the relative strength of circuit interactions in other ephaptic environments. As in *D. melanogaster*, ORNs in many other insect species are compartmentalized in sensillum environments that favor ephaptic interactions (Gnatzy et al., 1984; Hallberg et al., 1994; Hansson et al., 1994; Keil, 1984; Lu et al., 2007; Steinbrecht and Müller, 1976). Interestingly, ORNs in insects such as silk moth, corn borer, bed bug and mosquito, are also reported to exhibit markedly differing sizes (Gnatzy et al., 1984; Hallberg et al., 1994; Hansson et al., 1994; Keil, 1984; Lu et al., 2007; Steinbrecht and Müller, 1976), indicative of asymmetric ephaptic interactions in other insect olfactory sensilla. Such size disparities have also been reported in insect gustatory receptor neurons (GRNs), temperature-sensing neurons and humidity-sensing neurons that are compartmentalized in sensilla (Foelix et al., 1989; Shanbhag et al., 1995, 2001; Steinbrecht, 1989), suggesting that asymmetric ephaptic interactions between primary sensory neurons could be common in many sensory modalities of insects. In the central nervous system (CNS), asymmetric ephaptic interactions have been reported in classic studies of the fish Mauthner cell, between neurons of markedly different sizes (Faber and Korn, 1989). The findings of this study suggest that asymmetric neuronal interactions may be a common feature in other ephaptic environments in the CNS that are populated by neurons of disparate sizes, such as the Purkinje cells and basket cells in the cerebellum (Korn and Axelrad, 1980).

3.4.2 Asymmetric interaction between primary sensory neurons

Local lateral inhibition is a hallmark of sensory processing, allowing comparison of adjoining inputs (Kaas, 1997). In addition to fly olfaction (Su et al., 2012), direct lateral inhibition between adjacent sensory neurons has also been observed in the color photoreceptors of the fruit fly, dragonfly, butterfly, locust, and honeybee (Horridge et al., 1983; Matič, 1983; Menzel and Blakers, 1976; Schnaitmann et al., 2018; Shaw, 1975; Yang and Osorio, 1991) and in the GRNs of the bumblebees (Miriyala et al., 2018).

In fly vision, R7 and R8 photoreceptors of the same ommatidium mutually inhibit each other by means of direct inhibition, mediated by reciprocal synaptic connections between the photoreceptors, as well as indirect inhibition, involving other neuronal inputs (Schnaitmann et al., 2018). Interestingly, the mutual inhibition between R7 and R8 is also asymmetric. R8 can inhibit R7 by either the direct or indirect mechanism. In contrast, for R7 to inhibit R8, both the direct and indirect mechanisms are required (Schnaitmann et al., 2018). The asymmetry may arise from the unequal numbers of reciprocal synapses; R8 forms 20-31 synapses onto R7, whereas R7 only forms 0-2 synapses onto R8 in each medulla column (Longden, 2018; Takemura et al., 2015).

Another example of asymmetric interaction between sensory neurons has been reported in the GRNs housed in the bumblebee galea sensilla. Enabled by gap junction-mediated inhibitory coupling, the spike activity of one GRN (GRN1) strongly depends on inputs from its neighbor (GRN2), but the activity of GRN2 only weakly depends on GRN1. Such interaction allows burst spiking and slow adaptation in GRN1, likely important for feeding regulation (Miriyala et al., 2018; Mittal et al., 2018). Although the precise mechanisms differ, asymmetric lateral inhibition between adjacent primary sensory neurons may represent a conserved feature whereby sensory inputs are unequally processed at the periphery before being transmitted to higher brain centers.

3.5 Materials and methods

***Drosophila* stocks**

Flies were raised on standard cornmeal medium at 25°C and in an incubator with a 12-hr light/dark cycle. For the SBEM (*UAS-APEX2*) experiments, 6-8 day old females were used. The genotypes of the flies used for SBEM experiments were: (ab3) *Or22a-GAL4* (Bloomington #9951)*;10XUAS-mCD8GFP-APEX2* (Tsang et al., 2018)*,* (ab4) *Or56a-GAL4* (Bloomington #23896)*;10XUAS-cmyc-APEX2-Orco* (Tsang et al., 2018), (ab5) *Or47a-GAL4* (Bloomington #9981)*;10XUAS-cmyc-APEX2-Orco*, (at4) *Or47b-GAL4* (Bloomington #9984)*;10XUAS-cmyc-APEX2-Orco* and *Or88a-GAL4* (Bloomington #23294)*;10XUAS-cmyc-APEX2-Orco*, (ac3II) *Ir75c-GAL4* (Prieto-Godino et al., 2017)*;10XUAS-cmyc-APEX2-Orco*.

Sample preparation for SBEM

Target expression of APEX2 in ORNs for SBEM was performed as described (Tsang et al., 2018). Briefly, transgenic *Drosophila* lines (*10xUAS-myc-APEX2-Orco* or *10xUAS-mCD8GF-APEX2*) were generated to facilitate the dendritic membrane targeting of APEX2 (Tsang et al., 2018). Expression of APEX2 in select ORNs was driven by OrX-GAL4 drivers. Six-to eight-days-old female flies were cold anesthetized prior to the dissection of their antennae. With a sharp glass microelectrode, a hole was poked in the antenna to facilitate solution exchange. The antennae were then immediately processed with the CryoChem method (Tsang et al., 2018), which involves cryofixation by high-pressure freezing, freeze-substitution, rehydration, DAB labeling reaction, *en bloc* heavy metal staining, dehydration and resin infiltration.

Microcomputed X-ray tomography was performed on resin-embedded specimens using a Versa 510 X-ray microscope (Zeiss) to determine DAB-labeled region of interest. Next, the specimens were mounted on aluminum pins with conductive silver epoxy (Ted Pella) and sputter coated with gold-palladium for SBEM imaging. The ab3, ab4, ac3II, at4 datasets were collected with a Gemini SEM (Zeiss) equipped with a 3View block-face unit (Gatan); the ab5 dataset was collected with a Merlin scanning electron microscope (Zeiss) equipped with a 3View2XP and OnPoint backscatter detector (Gatan).

Segmentation of DAB-labeled *Drosophila* ORNs

The DAB-labeled *Drosophila* ORN was segmented in a semi-automated fashion using the IMOD software (Kremer et al., 1996) to generate a 3D model as described previously (Tsang et al., 2018). The IMOD command line ‘imodauto’ was used for the auto-segmentation by setting thresholds to isolate the labeled neuron of interest. Auto-segmentation was followed by manual proofreading and correction of errors by two independent proofreaders. The neighboring, unlabeled ORN was manually segmented using the same software. Due to insufficient DAB-labeling or image resolution, the fine outer dendritic branches of most basiconic ORNs could not be reliably identified for segmentation.

Morphometric analysis

The 3D model of each ORN was first separated into cell body, inner dendrite and outer (sensory) dendrite models. The inner and outer dendrites were separated at the cilium base, a notably constricted dendritic region (Shanbhag et al., 2000). The volume measurements of ORNs were then obtained with the “imodinfo” function in IMOD based on the 3D models.

The lengths of most inner and outer dendrites were determined by first converting the 3D models into binary image files using the IMOD command “imodmop”. Then the skeletons of the 3D images were extracted using the Skeletonize3D (https://imagej.net/Skeletonize3D) plugin in Fiji (NIH). The lengths of the resulting skeletons were obtained by the Fiji “Analyze Skeleton” function. For the ab3A, ab4A and ab5A ORNs, which exhibit significant dendritic enlargements (Figure 3.4A), their inner dendritic lengths were determined by first visually identifying the center point in every ninth contour of the 3D models (300~400 nm z-step), then manually measuring and summing the distances between those points. For comparison, the inner dendritic lengths of the ab3B, ab4B and ab5B ORNs were determined in the same way.

The outer dendrites of ORNs were assumed to be cylindrical and their surface areas were calculated based on the measured volumes and lengths accordingly. The surface areas of cell bodies were measured with the “imodinfo” function in IMOD.

Statistics

All data presented as mean ± SEM were analyzed using SigmaPlot 13.0 (https://systatsoftware.com/products/sigmaplot/). The unpaired two-tailed t-test was performed in Figure 3.1 for single variable comparison between two groups. The paired two-tailed t-test was performed in Figure 3.2 and 3.3 for the morphological comparison between grouped ORNs. Data are presented as mean ± SEM $p < 0.05$ was considered to be statistically significant and is presented as * $p < 0.05$, ** $p < 0.01$, or *** $p < 0.001$.

Chapter 3, in part, has been submitted for publication of the material as it may appear in Asymmetric ephaptic interactions in the initial stage of olfactory processing, 2017. Zhang, Ye; Tsang, Tin Ki; Bushong, Eric A.; Chu, Li-An; Chiang, Ann-Shyn; Ellisman, Mark H.; Reingruber, Jürgen; Su, Chih-Ying, Neuron, 2017. The dissertation author and Ye Zhang contributed equally as primary investigators and authors of this material.

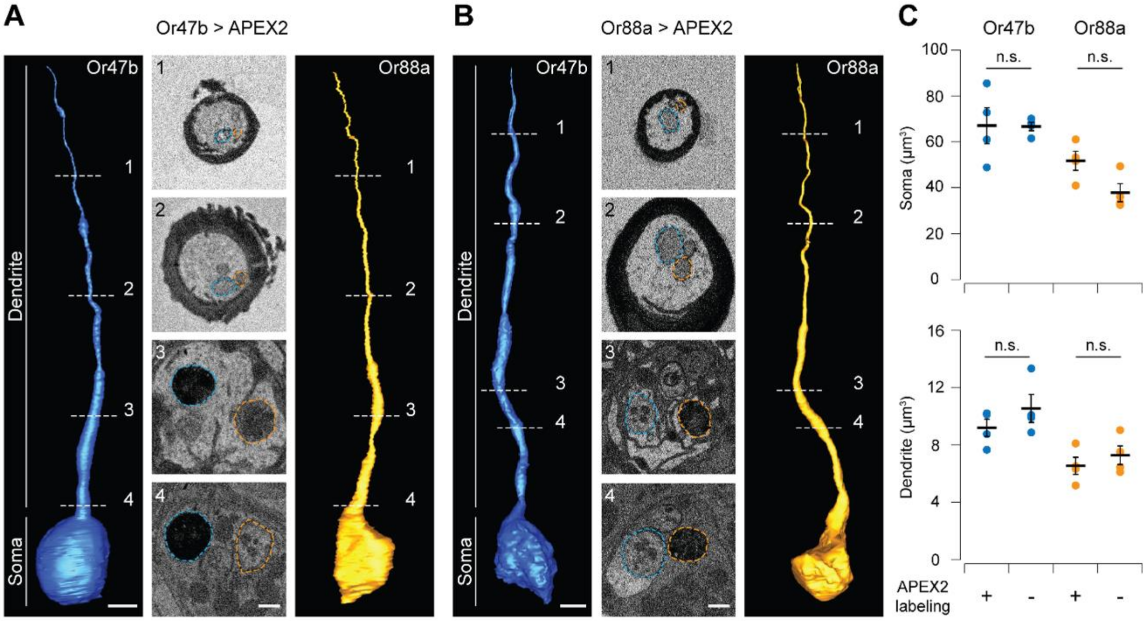

Figure 3.1. DAB labeling does not influence the volume measurements of ORNs. (A-B) 3D reconstruction of the Or47b (blue) and Or88a ORNs (orange) based on the SBEM volumes generated from Or47b>APEX2 and Or88a>APEX2 antenna, respectively. (A) Or47b ORNs expressing APEX2 were labeled with DAB. Sample SBEM images are shown in the middle panel. Dotted lines outline the Or47b ORN (blue) and its intermediate-sized neighbor (orange). (B) Or88a ORNs expressing APEX2 were labeled with DAB. In the sample SBEM images, dotted lines outline the Or88a ORN (orange) and its largest-sized neighbor (blue). Scale bars: 2 µm for 3D models, 500 nm for SBEM images. (C) The soma and dendritic volumes of the Or47b and Or88a ORNs, mean ± s.e.m. n=4 pairs of ORNs. APEX2-labeled vs. unlabeled Or47b soma, p=0.725; Or88a soma, p=0.224; Or47b dendrite, p=0.274; Or88a dendrite, p=0.167, *t* test.

Figure 3.2. Morphometric analysis of the soma of grouped ORNs.
(A-E) Volume, sphericity and surface area measurements of the soma of the paired ORNs in five sensillum types. (Left) Sample 3D reconstruction based on SBEM images. “A” neurons in blue and “B” or “C” neurons in orange. Arrows indicate the cilium base, a constricted region separating the inner and outer dendrites. Scale bars: 2 µm. Lines connect measurements from paired ORNs, mean ± s.e.m. n=4-5 for all except for at4, n=8. *p<0.05, **p<0.01, ***p<0.001; soma volume of ab5A vs. ab5B, p=0.601; sphericity of ac3IIA vs. ac3IIB, p=0.391; soma surface area of ab3A vs. ab3B, p=0.119, paired *t* test. See Table S3.1 for numerical morphometric data.

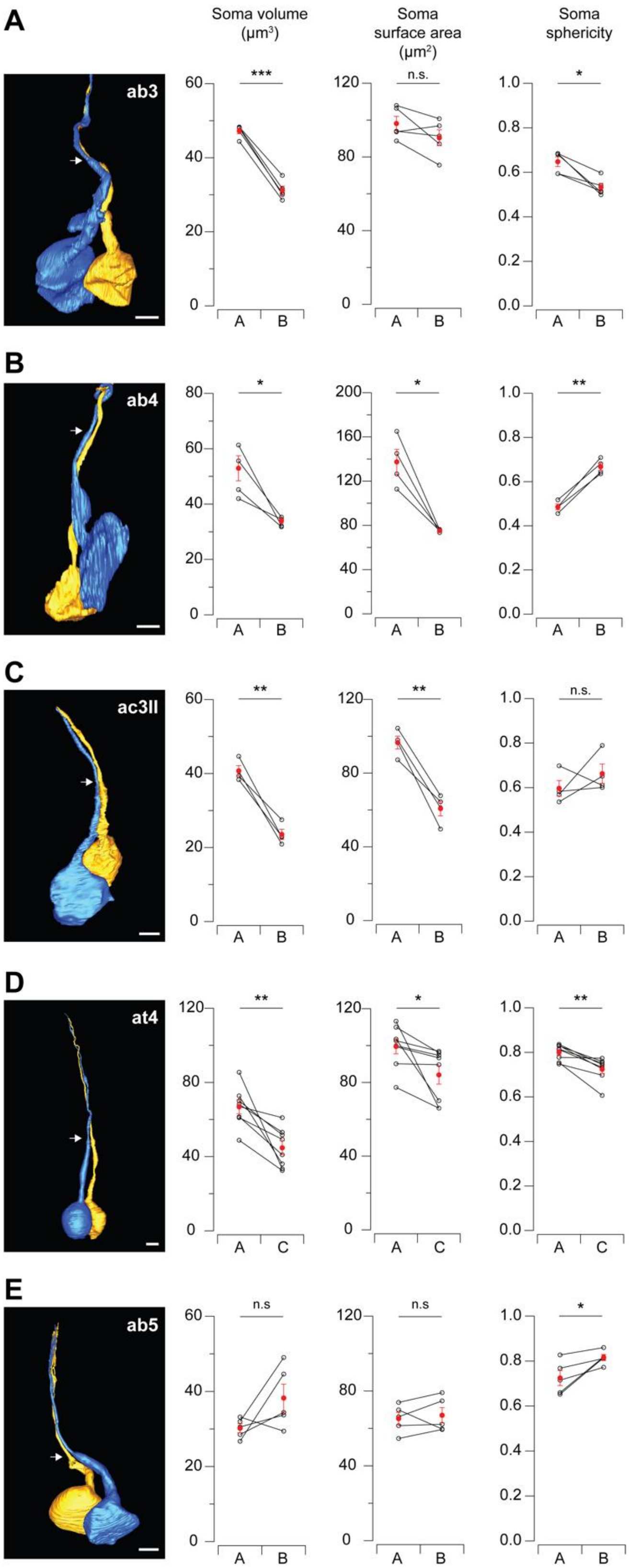
A
B
C
D
E
Soma volume (μm³)
Soma surface area (μm²)
Soma sphericity
ab3
ab4
ac3II
at4
ab5
***
n.s.
*
**
n.s
A
B
C
0
20
40
60
80
120
160
200
0.0
0.2
0.4
0.6
0.8
1.0

Figure 3.3. Morphometric analysis of the inner and outer dendrites of grouped ORNs. (A-E) Volume measurements of the inner and outer dendrites, and the outer dendritic surface areas of the paired ORNs in five sensillum types. (Left) Sample 3D reconstruction based on SBEM images. "A" neurons in blue and "B" or "C" neurons in orange. Arrows indicate the cilium base, a constricted region separating the inner and outer dendrites. Due to technical limitations, the outer dendrites of most basiconic sensilla could not be completely reconstructed. Scale bars: 2 µm. Lines connect measurements from paired ORNs, mean ± s.e.m. $n=4$-5 for all except for at4, $n=8$. *$p<0.05$, **$p<0.01$, ***$p<0.001$; outer dendrite surface area of ac3IIA vs. ac3IIB, $p=0.194$, paired t test. Error bars and statistics are unavailable for the ab5 outer dendrites as only two data points were obtained. See Table S3.1 for numerical morphometric data.

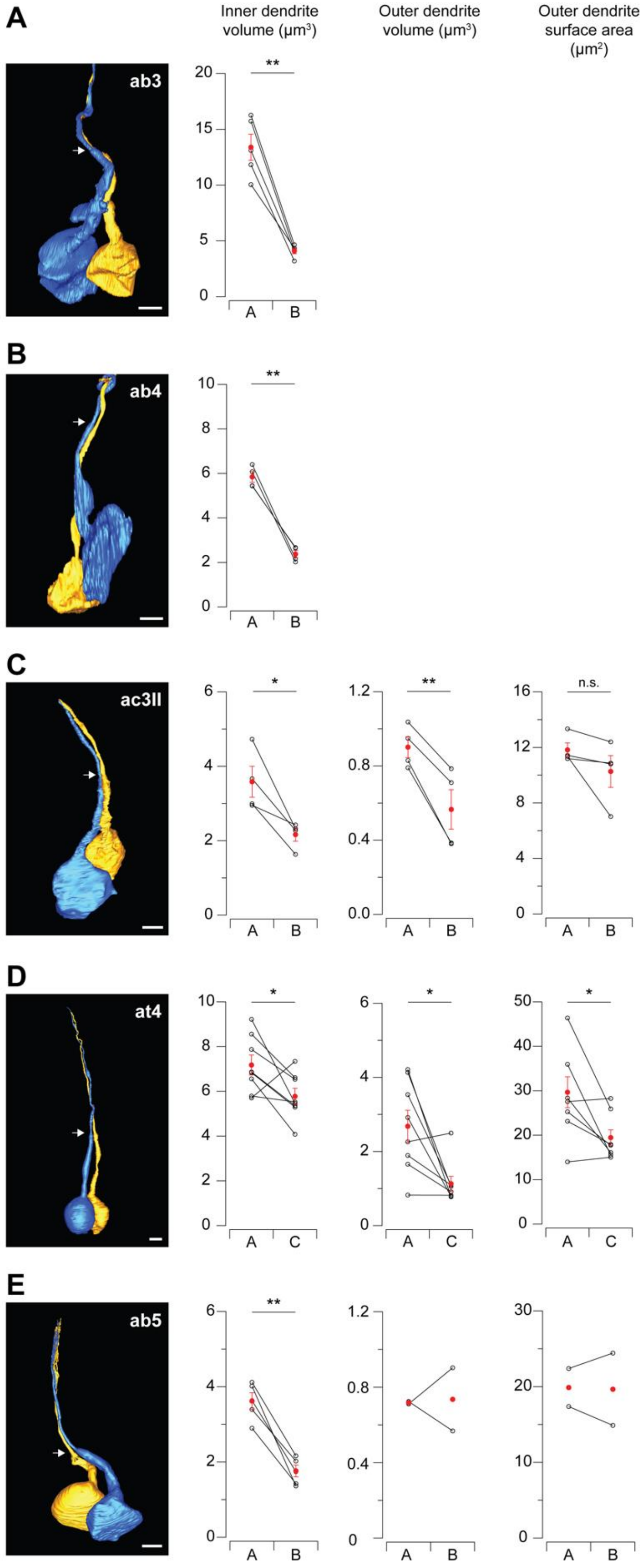
A
Inner dendrite volume (µm³)
Outer dendrite volume (µm³)
Outer dendrite surface area (µm²)
ab3
**
20
15
10
5
0
A
B
B
ab4
**
10
8
6
4
2
0
A
B
C
ac3II
*
6
4
2
0
A
B
**
1.2
0.8
0.4
0.0
A
B
n.s.
16
12
8
4
0
A
B
D
at4
*
10
8
6
4
2
0
A
C
*
6
4
2
0
A
C
*
50
40
30
20
10
0
A
C
E
ab5
**
6
4
2
0
A
B
1.2
0.8
0.4
0
A
B
30
20
10
0
A
B

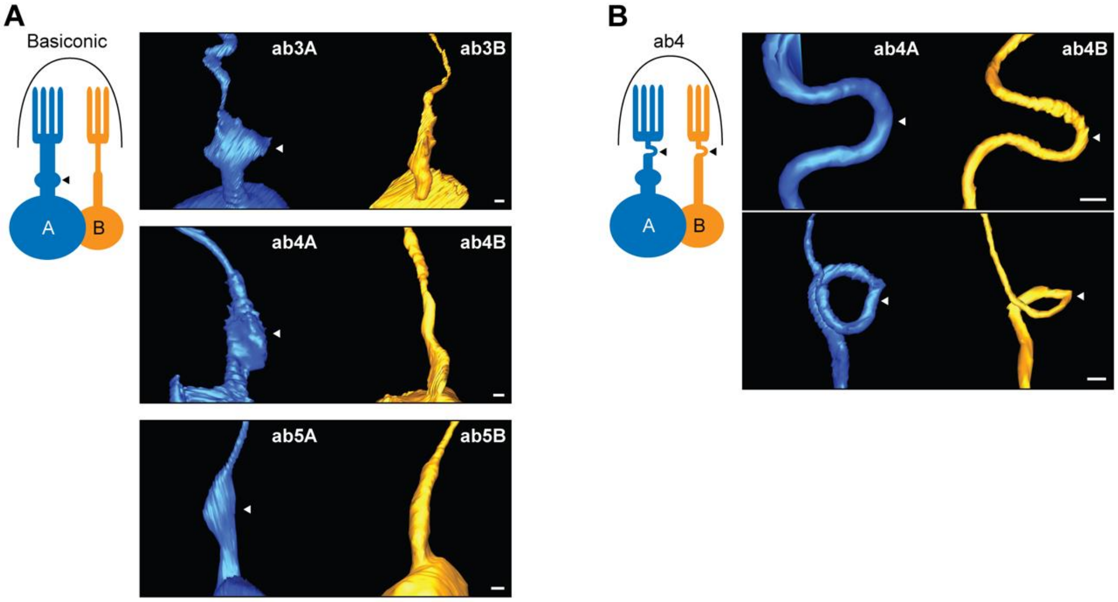

Figure 3.4. Novel morphological features of ORNs revealed by 3D reconstructions. (A) An enlargement of the inner dendrite (arrow head) was observed in the “A” ORNs in all three types of basiconic sensilla characterized. (B) At the sensillum base, a bend or loop (arrow head) was observed in the unbranched outer dendrite of ab4 ORN. Scale bars: 500 nm.

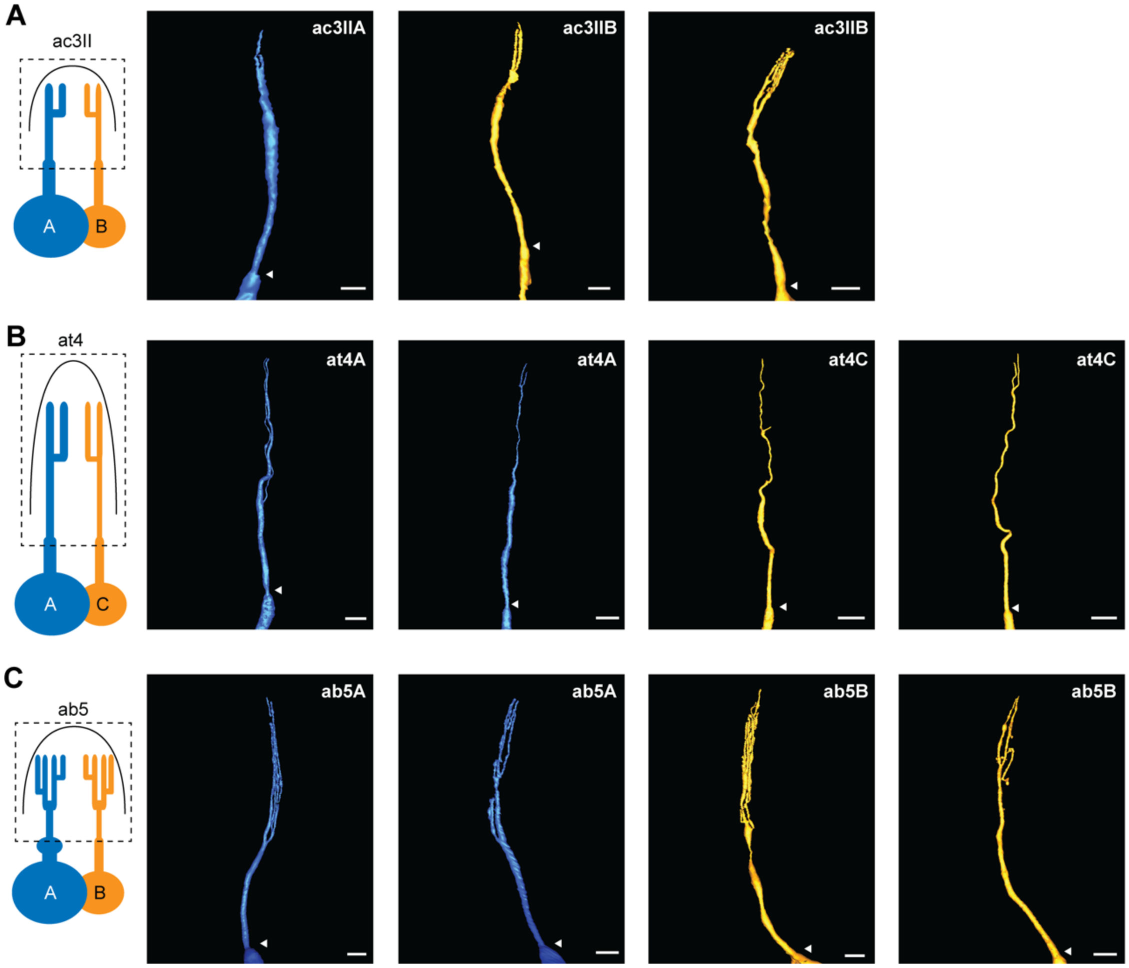

Figure 3.5. 3D reconstructions of ORNs revealed the diverse morphology of outer dendritic branches. Examples of ORN outer dendrites in (A) ac3II, (B) at4, and (C) ab5 sensilla. Dotted lines denote the general region of the ORNs that are highlighted in the 3D reconstructions on the right. Arrow heads indicate the cilium base, a constricted region separating the inner and outer dendrites. Scale bars in (A) and (C): 1 µm; scale bars in (B) 2 µm.

Figure 3.6. A revised electric circuit model for compartmentalized ORNs.
(A) Passive electric circuit model of a sensillum consisting of an auxiliary cell (gray rectangle) and two ORNs. Compared to the existing model, the revised model does not assume identical electrotonic properties between grouped ORNs. (B) Fitting and simulation according to the revised model. (B1) Simultaneous fitting of the LFP responses of the ORNs housed in the ac3II, ab3, ab4 and ab5 sensilla. All paired ORNs have distinct morphometric features with the exception of the ab5 ORNs. Identical parameters were used for all ORNs, except for the morphometric parameters and odorant sensitivity, which are ORN-specific and determined based on the experimental data whenever available. Each curve describes the dose-response relationship of an ORN when activated by a private odorant. Empty circles indicate measured LFP responses. Odorant concentrations are plotted logarithmically on the x-axis. (B2) Simulation of the transmembrane potential of an ORN (V_m) upon activation by a private odorant. (B3) Simulation (ac3II and ab5) and fitting (ab3 and ab4) of the depolarization of an ORN (ΔV_m) in relation to its LFP response. (C) Morphometric parameters. Measured input parameters are shown in black, and fitted values in blue. (D) Simulation of the LFP responses and transmembrane potential changes of the ab4 ORNs, assuming that the paired ORNs express the same odorant receptor, Or56a. Except for ab4A odorant sensitivity, all fitting parameters are as in (B1) for ab4. Blue: large-spike “A” ORN. Orange: small-spike “B” ORN.

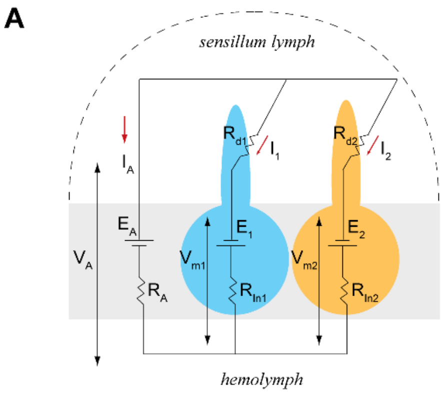

Parameter	Description
E_A	Battery simulating the potential generated by the auxiliary cells
R_A	Input resistance of the auxiliary cells
I_A	Current through the auxiliary cells
E_1 & E_2	Battery simulating the transmembrane ionic gradients across the soma of the ORNs
R_{In1} & R_{In2}	Input resistance of the soma of the ORNs
R_{d1} & R_{d2}	Input resistances of the sensory dendrites, which are odorant stimulation dependent
V_A	Transepithelium potential
V_{m1} & V_{m2}	Transmembrane potentials of the ORNs
I_1 & I_2	Current through ORNs

Changes in V_A due to odorant stimulation of ORN1 or ORN2 are measured as ΔLFP.

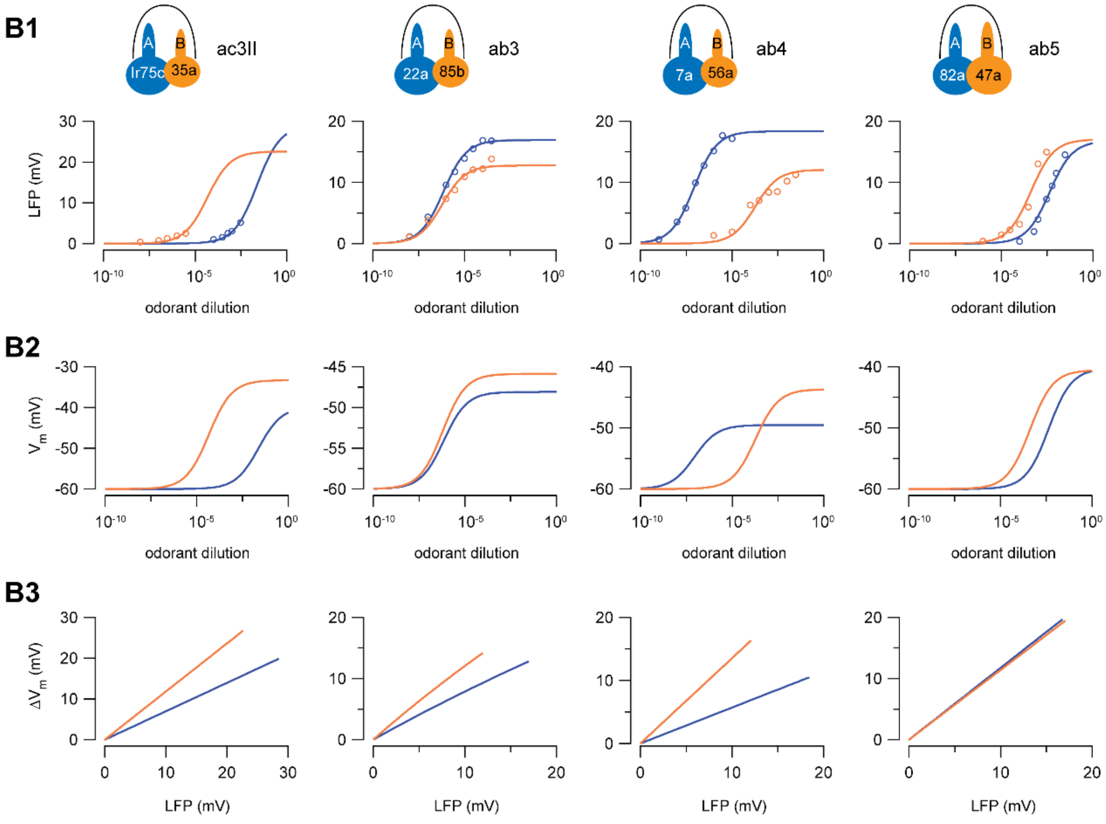

C

		surface area (μm²)	
		soma	sensory dendrite
ac3II	A	96	12
	B	60	10
ab3	A	98	47
	B	90	11
ab4	A	137	37
	B	75	20
ab5	A	65	20
	B	67	20

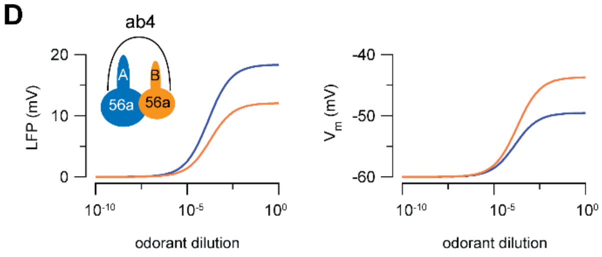

Table 3.1. Morphometric measurements of grouped ORNs.

The two at4 datasets were acquired independently based on the identity of APEX2-labeled ORN, as indicated by the asterisks. The # symbol denotes the outer dendritic lengths that measure the distances between the cilium bases and the tips of the longest dendritic branch. See Materials and methods for details on the quantifications. n=4-5 per sensillum type.

ORN type	Soma volume (μm^3)	Soma sphericity	Soma surface area (μm^2)	Inner dendrite volume (μm^3)	Inner dendrite length (μm)	Outer dendrite volume (μm^3)	Outer dendrite length$^{\#}$ (μm)	Outer dendrite length (includes all branches) (μm)	Derived outer dendrite surface area (μm^2)
ab3A	47.2 ± 0.7	0.65 ± 0.02	98.1 ± 3.8	13.4 ± 1.2	12.7 ± 0.9	n.a.	n.a.	n.a.	n.a.
ab3B	31.2 ± 1.3	0.53 ± 0.02	90.3 ± 4.4	4.1 ± 0.2	11.0 ± 1.0	n.a.	n.a.	n.a.	n.a.
ab4A	51.0 ± 4.5	0.49 ± 0.01	137.4 ± 11.3	5.8 ± 0.2	7.5 ± 1.2	n.a.	n.a.	n.a.	n.a.
ab4B	33.4 ± 0.9	0.67 ± 0.02	75.3 ± 0.7	2.4 ± 0.2	9.0 ± 0.9	n.a.	n.a.	n.a.	n.a.
ab5A	30.2 ± 1.2	0.73 ± 0.03	65.2 ± 3.3	3.6 ± 0.2	5.2 ± 0.4	0.7 ± 0.0	17.0 ± 0.4	44.5 ± 11.5	19.9 ± 2.5
ab5B	38.2 ± 3.7	0.82 ± 0.01	67.0 ± 4.1	1.7 ± 0.2	4.1 ± 0.4	0.7 ± 0.2	17.8 ± 1.2	41.7 ± 10.8	19.7 ± 4.8
ac3IIA	40.7 ± 1.4	0.60 ± 0.04	96.5 ± 3.6	3.6 ± 0.4	12.7 ± 1.3	0.9 ± 0.1	11.5 ± 0.4	12.3 ± 0.7	11.8 ± 0.5
ac3IIB	23.7 ± 1.4	0.66 ± 0.04	60.7 ± 3.9	2.2 ± 0.2	13.8 ± 1.7	0.6 ± 0.1	12.3 ± 1.0	15.7 ± 3.0	10.3 ± 1.1
at4A*	67.0 ± 7.9	0.83 ± 0.01	96.0 ± 7.8	7.5 ± 0.4	15.5 ± 1.5	1.7 ± 0.3	24.0 ± 1.8	24.3 ± 1.9	22.5 ± 3.0
at4C	37.8 ± 3.9	0.75 ± 0.01	73.0 ± 5.6	6.0 ± 0.4	17.1 ± 2.1	1.3 ± 0.4	24.4 ± 1.4	24.4 ± 1.4	19.7 ± 2.9
at4A	66.7 ± 1.8	0.77 ± 0.02	103.0 ± 2.4	6.8 ± 0.8	12.9 ± 1.9	3.7 ± 0.3	23.1 ± 0.9	30.0 ± 6.1	36.8 ± 3.7
at4C*	51.7 ± 4.1	0.70 ± 0.04	95.3 ± 0.8	5.6 ± 0.7	15.3 ± 2.2	0.9 ± 0.1	25.5 ± 0.7	31.6 ± 5.6	19.1 ± 2.3

3.6 References

de Bruyne, M., Foster, K., Carlson, J.R. (2001a). Odor coding in the Drosophila antenna. Neuron *30*, 537–552.

Briggman, K.L., Bock, D.D. (2012). Volume electron microscopy for neuronal circuit reconstruction. Curr. Opin. Neurobiol. *22*, 154–161.

Connell, R.J.O. (1985). Responses to pheromone blends in insect olfactory receptor neurons. J. Comp. Physiol. A *156*, 747–761.

Denk, W., Horstmann, H. (2004). Serial block-face scanning electron microscopy to reconstruct three-dimensional tissue nanostructure. PLoS Biol. *2*, e329.

Faber, D.S., Korn, H. (1989). Electrical field effects: their relevance in central neural networks. Physiol. Rev. *69*, 821–863.

Foelix, R., Stocker, R., Steinbrecht, R. (1989). Fine structure of a sensory organ in the arista of Drosophila melanogaster and some other dipterans. Cell Tissue Res. *258*, 277–287.

Gnatzy, W., Mohren, W., Steinbrecht, R.A. (1984). Pheromone receptors in Bombyx mori and Antheraea pernyi II. Morphometric analysis. Cell Tissue Res. *235*, 35–42.

Hallberg, E., Hansson, B.S., Steinbrecht, R. a (1994). Morphological characteristics of antennal sensilla in the European cornborer Ostrinia nubilalis (Lepidoptera: Pyralidae). Tissue Cell *26*, 489–502.

Hansson, B.S., Hallberg, E., Löfstedt, C., Steinbrecht, R. a (1994). Correlation between dendrite diameter and action potential amplitude in sex pheromone specific receptor neurons in male Ostrinia nubilalis (Lepidoptera: Pyralidae). Tissue Cell *26*, 503–512.

Harraca, V., Ignell, R., Löfstedt, C., Ryne, C. (2009). Characterization of the antennal olfactory system of the bed bug (Cimex lectularius). Chem. Senses *35*, 195–204.

Horridge, G.A., Marčelja, L., Jahnke, R., Matič, T. (1983). Single electrode studies on the retina of the butterfly Papilio. J. Comp. Physiol. A *150*, 271–294.

Kaas, J.H. (1997). Topographic maps are fundamental to sensory processing. Brain Res. Bull. *44*, 107–112.

Kaissling, K. (1996). Peripheral mechanisms of pheromone reception in Moths. Chem. Senses *21*, 257–268.

Kaissling, K.E., Kasang, G., Bestmann, H.J., Stransky, W., Vostrowsky, O. (1978). A new pheromone of the silkworm moth Bombyx mori - Sensory pathway and behavioral effect. Naturwissenschaften *65*, 382–384.

Keil, T.A. (1984). Reconstruction and morphometry of silkmoth olfactory hairs: A comparative study of sensilla trichodea on the antennae of male Anteraea polyphemus and Anteraea pernyi (Insecta, Lepidoptera). Zoomorphology *104*, 147–156.

Koch, C. (2004a). Biophysics of computation: information processing in single neurons (Oxford university press).

Koch, C. (2004b). Biophysics of Computation (Oxford University Press).

Kochansky, J., Tette, J., Taschenberg, E.F., Cardé, R.T., Kaissling, K.E., Roelofs, W.L. (1975). Sex pheromone of the moth, Antheraea polyphemus. J. Insect Physiol. *21*, 1977–1983.

Korn, H., Axelrad, H. (1980). Electrical inhibition of Purkinje cells in the cerebellum of the rat. Proc. Natl. Acad. Sci. U. S. A. *77*, 6244–6247.

Kremer, J.R., Mastronarde, D.N., McIntosh, J.R. (1996). Computer visualization of three-dimensional image data using IMOD. J. Struct. Biol. *116*, 71–76.

Kumar, G.L., Keil, T. a. (1996). Pheromone stimulation induces cytoskeletal changes in olfactory dendrites of male silkmoths (Lepidoptera, Saturniidae, Bombycidae). Naturwissenschaften *83*, 476–478.

Lam, S.S., Martell, J.D., Kamer, K.J., Deerinck, T.J., Ellisman, M.H., Mootha, V.K., Ting, A.Y. (2015). Directed evolution of APEX2 for electron microscopy and proximity labeling. Nat. Methods *12*, 51–54.

Longden, K.D. (2018). Colour vision: A fresh view of lateral inhibition in Drosophila. Curr. Biol. *28*, R308–R311.

Lu, T., Qiu, Y.T., Wang, G., Kwon, J.Y., Rutzler, M., Kwon, H.W., Pitts, R.J., van Loon, J.J. a, Takken, W., Carlson, J.R., Zwiebel, L. J. (2007). Odor Coding in the Maxillary Palp of the Malaria Vector Mosquito Anopheles gambiae. Curr. Biol. *17*, 1533–1544.

Martell, J.D., Deerinck, T.J., Sancak, Y., Poulos, T.L., Mootha, V.K., Sosinsky, G.E., Ellisman, M.H., Ting, A.Y. (2012). Engineered ascorbate peroxidase as a genetically encoded reporter for electron microscopy. Nat. Biotechnol. *30*, 1143–1148.

Matič, T. (1983). Electrical inhibition in the retina of the butterfly Papilio. J. Comp. Physiol. A *152*, 169–182.

Menzel, R., Blakers, M. (1976). Comparative colour receptors in the bee eye-morphology and spectral sensitivity. J. Comp. Physiol. A *108*, 11–33.

Miriyala, A., Kessler, S., Rind, F.C., Wright, G.A. (2018). Burst firing in bee gustatory neurons prevents adaptation. Curr. Biol. *28*, 1585–1594.e3.

Mittal, A.M., Singh, S.S., Gupta, N. (2018). Sensory coding: Neurons that wire together fire longer. Curr. Biol. *28*, R608–R610.

Nagel, K.I., Wilson, R.I. (2011). Biophysical mechanisms underlying olfactory receptor neuron dynamics. Nat. Neurosci. *14*, 208–216.

Prieto-Godino, L.L., Rytz, R., Cruchet, S., Bargeton, B., Abuin, L., Silbering, A.F., Ruta, V., Dal Peraro, M., Benton, R. (2017). Evolution of acid-sensing olfactory circuits in Drosophilids. Neuron *93*, 661–676.e6.

Raue, A., Schilling, M., Bachmann, J., Matteson, A., Schelke, M., Kaschek, D., Hug, S., Kreutz, C., Harms, B.D., Theis, F.J., et al. (2013). Lessons learned from quantitative dynamical modeling in systems biology. PLoS One *8*.

Raue, A., Steiert, B., Schelker, M., Kreutz, C., Maiwald, T., Hass, H., Vanlier, J., Tönsing, C., Adlung, L., Engesser, R., et al. (2015). Data2Dynamics: A modeling environment tailored to parameter estimation in dynamical systems. Bioinformatics *31*, 3558–3560.

Rospars, J.-P., Lánský, P., Duchamp, A., Duchamp-Viret, P. (2003). Relation between stimulus and response in frog olfactory receptor neurons in vivo. Eur. J. Neurosci. *18*, 1135–1154.

Schnaitmann, C., Abraham, E., Oberhauser, V., Thestrup, T., Griesbeck, O., Reiff, D.F. (2018). Color processing in the early visual system of Drosophila. 318–330.

Shanbhag, S.R., Singh, K., Singh, R.N. (1995). Fine structure and primary sensory projections of sensilla located in the sacculus of the antenna of Drosophila melanogaster. 237–249.

Shanbhag, S.R., Müller, B., Steinbrecht, R.A. (1999). Atlas of olfactory organs of Drosophila melanogaster 1. Types, external organization, innervation and distribution of olfactory sensilla. Int. J. Insect Morphol. Embryol. *28*, 377–397.

Shanbhag, S.R., Müller, B., Steinbrecht, R.A. (2000). Atlas of olfactory organs of Drosophila melanogaster 2. Internal organization and cellular architecture of olfactory sensilla. Arthropod Struct. Dev. *29*, 211–229.

Shanbhag, S.R., Park, S.K., Pikielny, C.W., Steinbrecht, R.A. (2001). Gustatory organs of Drosophila melanogaster: Fine structure and expression of the putative odorant-binding protein PBPRP2. Cell Tissue Res. *304*, 423–437.

Shaw, S.R. (1975). Retinal resistance barriers and electrical lateral inhibition. Nature *255*, 480–482.

Steinbrecht, R.A. (1970). Zur morphometrie der antenne des seidenspinners, Bombyx mori L.: Zahl und Verteilung der Riechsensillen (Insecta, Lepidoptera). Zeitschrift Für Morphol. Der Tiere *68*, 93–126.

Steinbrecht, R.A. (1973). Der Feinbau olfaktorischer Sensillen des Seidenspinners (Insecta, Lepidoptera). Zeitschrift Für Zellforsch. Und Mikroskopische Anat. *139*, 533-565.

Steinbrecht, R.A. (1989). The fine structure of thermo-/hygrosensitive sensilla in the silkmoth Bombyx mori: Receptor membrane substructure and sensory cell contacts. Cell Tissue Res. *255*, 49–57.

Steinbrecht, R. a, Müller, B. (1976). Fine structure of the antennal receptors of the bed bug, Cimex lectularius L. Tissue Cell *8*, 615–636.

Steinbrecht, R.A., Verhmtensphysiologie, N. (1973). Der Feinbau olfaktorischer Sensillen des Seidenspinners (Insecta, Lepidoptera). Zeitschrift Für Zellforsch. Und Mikroskopische Anat. *139*, 533–565.

Su, C.-Y., Menuz, K., Carlson, J.R. (2009). Olfactory perception: receptors, cells, and circuits. Cell *139*, 45–59.

Su, C.-Y., Menuz, K., Reisert, J., Carlson, J.R. (2012). Non-synaptic inhibition between grouped neurons in an olfactory circuit. Nature *492*, 66–71.

Takemura, S., Xu, C.S., Lu, Z., Rivlin, P.K., Parag, T., Olbris, D.J., Plaza, S., Zhao, T., Katz, W.T., Umayam, L., et al. (2015). Synaptic circuits and their variations within different columns in the visual system of *Drosophila*. Proc. Natl. Acad. Sci. *112*, 13711–13716.

Tsang, T.K., Bushong, E.A., Boassa, D., Hu, J., Romoli, B., Phan, S., Dulcis, D., Su, C.-Y., Ellisman, M.H. (2018). High-quality ultrastructural preservation using cryofixation for 3D electron microscopy of genetically labeled tissues. eLife *7*, e35524.

Vermeulen, A., Rospars, J.-P. (2004). Why are insect olfactory receptor neurons grouped into sensilla? The teachings of a model investigating the effects of the electrical interaction between neurons on the transepithelial potential and the neuronal transmembrane potential. Eur. Biophys. J. *33*, 633–643.

Wadell, H. (1935). Volume , Shape , and Roundness of Quartz. J. Geol. *43*, 250–280.

Xu, Y., Fan, W., Qian, M.C. (2007). Characterization of aroma compounds in apple cider using solvent-assisted flavor evaporation and headspace solid-phase microextraction. J. Agric. Food Chem. *55*, 3051–3057.

Wanner, A.A., Kirschmann, M.A., Genoud, C. (2015). Challenges of microtome-based serial block-face scanning electron microscopy in neuroscience. J. Microsc. *259*, 137–142.

Yang, E.C., Osorio, D. (1991). Spectral sensitivities of photoreceptors and lamina monopolar cells in the dragonfly, Hemicordulia tau. J. Comp. Physiol. A *169*, 663–669.

Appendix 1: Discovery of two types of ORNs each innervating two distinct peripheral environments

Results and Discussion

An unexpected heterogeneity of ORN grouping was revealed by the morphological characterization of the large-spiked neuron in the at4 sensillum. We discovered that this type of ORN (at4A), which expresses the odorant receptor Or47b, is housed not only in the characterized at4 sensilla with three neurons (Couto et al., 2005), but also in another type of trichoid sensilla that houses only two neurons (Fig. 4.1). A previous electron microscopy study documented three morphological types of trichoid sensilla, each housing one (T1), two (T2) or three (T3, or at4) ORNs (Shanbhag et al., 1999). While the molecular identities of ORNs housed in the T1 and T3 sensilla have been described (Couto et al., 2005), the ORNs housed in the T2 sensilla were initially misidentified and have since remained unknown (Couto et al., 2005; Lin and Potter, 2015). The discovery of the identity of one of the ORNs housed in the T2 sensilla is enabled by our EM approach, as genetic labeling of the Or47b ORNs with APEX2 is required to conclusively demonstrate this heterogeneity of ORN grouping.

Next, we identified the neighboring neuron in the Or47b-positive T2 sensillum. It was reported that Or47b ORN is housed with the Or88a and Or65a ORNs in the T3 sensilla (Couto et al., 2005). Preliminary data suggest there is a subset of trichoid sensilla that house neurons that respond to stimuli for only Or47b and Or88a but not for Or65a (data from Ye Zhang, not shown). Therefore, we hypothesized that Or88a ORN is the partner of Or47b ORN in the T2 sensillum. We tested this hypothesis by generating an SBEM dataset which labeled Or88a ORNs with APEX2/DAB (Chapter 3) and determined that Or88a ORNs indeed is also housed in the T2 sensilla. Of the four T2 sensilla observed in the Or47b labeled SBEM dataset, all contained the Or47b ORN; of the two T2 sensilla observed in the Or88a labeled dataset, both contained the Or88a ORN. Therefore, the EM data suggest that all the T2 sensilla house the Or47b and Or88a ORNs.

The heterogeneity of the ORN grouping implies that the Or47b and Or88a ORNs have different partners for ephaptic interactions in the T2 vs T3 sensilla. The distinct peripheral environments could lead to differences in odor computation between the two populations of Or47b and Or88a ORNs. Interestingly, subcompartments were reported in the glomerulus, VA1lm, which is innervated by Or47b ORNs (Laissue et al., 1999). Therefore, we hypothesized that the brain distinguishes odor information received from the two types of Or47b neurons by spatially segregating their axonal innervations in the antennal lobe. Specifically, we hypothesized that the Or47b ORNs in the T2 and T3 sensilla innervate distinct regions of the VA1lm glomerulus. To test this hypothesis, we generated transgenic flies in which only one Or47b ORN was labeled with the V5 epitope through random, low-frequency FLP recombinations. Preliminary data suggest that there is an individual Or47b ORN which predominately innervates the lateral region of the VA1lm glomerulus (Fig. 4.2, n=1). However, the frequency of generating flies with the desired genotype was too low (often <1/30), which made it difficult to obtain a large sample size.

Future Directions

Instead of using low-frequency FLP recombinations to generate a fly in which only one Or47b ORN is labeled, one could trace the axonal projections of individual Or47b ORNs by performing dye fill experiments in Or65a>Channelrhodopsin2 flies. Since the only difference between the T2 and T3 sensilla is the inclusion of the Or65a ORN in the T3 sensilla, one could use the presence of a light-activated Channelrhodopsin2 response to distinguish between them.

In the antennal lobe, olfactory receptor neurons synapses onto projection neurons (PNs) that propagate the odor information into two higher brain regions: the mushroom body and the lateral horn. We hypothesized that some PNs selectively innervate the lateral or medial compartment of the VA1lm glomerulus, such that the odor information detected by the two populations of Or47b ORNs is propagated differently in the brain. One could collaborate with Dr. Gregory Jefferis' lab to address this question by reconstructing PNs in his lab's *Drosophila* brain connectome data set. If the anatomy of the T2 and T3 Or47b circuits is different, then it will be the first example showing that ORNs expressing the same odorant receptor can project to distinctive regions in the central brain. Importantly, those findings in *Drosophila* olfaction have the potential to demonstrate the impact of peripheral environment on sensory information processing in the central circuits.

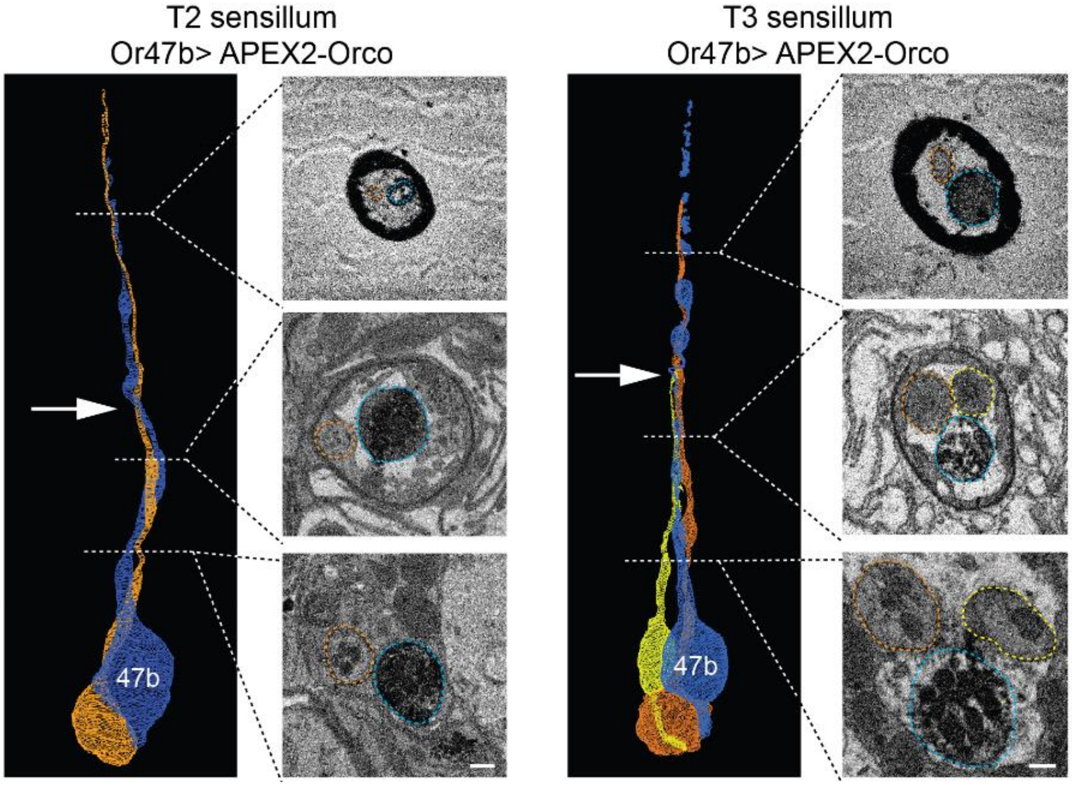

Figure 4.1. 3D reconstruction of the ORNs housed in T2 and T3 sensilla based on Or47b-labeled SBEM images (right panels). Or47b neurons are labeled by APEX2 reaction. Arrows indicate the cilium base, a structure that separates the inner and outer dendrites. Scale bar = 2 µm.

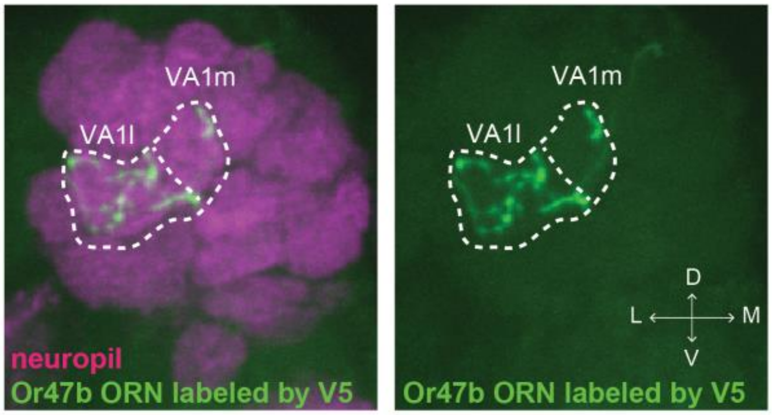

Figure 4.2. An individual Or47b ORN innervating the lateral region of VA1lm glomerulus (VA1l). A single Or47b ORN was labeled with the V5 epitope using random, low-frequency FLP recombination. Dotted lines indicate the VA1lm glomerulus and the potential partition that separates the lateral and the medial subcompartments.

References

Couto, A., Alenius, M., Dickson, B.J. (2005). Molecular, anatomical, and functional organization of the Drosophila olfactory system. Curr. Biol. *15*, 1535–1547.

Laissue, P.P., Reiter, C., Hiesinger, P.R., Halter, S., Fischbach, K.F., Stocker, R.F. (1999). Three-dimensional reconstruction of the antennal lobe in Drosophila melanogaster. J. Comp. Neurol. *405*, 543–552.

Lin, C.C., Potter, C.J. (2015). Re-classification of Drosophila melanogaster trichoid and intermediate sensilla using fluorescence-guided single sensillum recording. PLoS One *10*, 1–14.

Shanbhag, S.R., Müller, B., Steinbrecht, R.A. (1999). Atlas of olfactory organs of Drosophila melanogaster 1. Types, external organization, innervation and distribution of olfactory sensilla. Int. J. Insect Morphol. Embryol. *28*, 377–397.

Appendix 2: Lateral excitation between grouped olfactory receptor neurons in *Drosophila*

Results and Discussion

While lateral inhibition is observed in a sensillum when both olfactory receptor neurons (ORNs) are activated (Su et al. 2012), preliminary data from our lab shows that strong activation of one ORN moderately, yet significantly, activates its neighbor (data from Chih-Ying Su, not shown). This neuronal activation is independent of synaptic transmission and is likely mediated by ephaptic excitation (Ramón and Moore, 1978).

ORNs are not coupled via gap junctions

It is formally possible that lateral excitation between ORNs in a sensillum is mediated via gap junctions. We tested this possibility in a dye-fill experiment, an assay commonly used to assess gap junction communication between neurons (Phelan et al., 1996). This experiment was performed with the help of Varoth Lilascharoen. We did not observe any Lucifer yellow dye (molecular weight 457.2442 g/mol) transfer between ORNs (Figure 5.1), suggesting that ORNs are not electrically coupled *via* gap junctions (Bohrmann and Haas-Assenbaum, 1993; Phelan et al., 1996). This result is consistent with our earlier observation with a cross-correlation analysis that neighboring ORNs do not spike synchronously (Su et al., 2012). Furthermore, our results also agree with earlier electron microscopy studies in which no gap junctions were observed between neighboring *Drosophila* ORNs (Shanbhag et al., 1999, 2000). Together, these findings strongly argue that ORNs do not functionally interact with one another via gap junctions. Considering that ORNs also do not synapse onto each other and that the sensillum environment favors ephaptic interactions, lateral excitation in a sensillum is most likely mediated by ephaptic excitation.

Lateral excitation is bidirectional in a sensillum

Our preliminary data show that strong activation of “B” ORNs elicits clear excitatory spike responses in the neighboring “A” neuron (data from Chih-Ying Su, not shown). It is unknown whether lateral excitation, like ephaptic inhibition, is bidirectional. But given the likely electrical nature of this lateral excitation, we hypothesized that it would indeed be bidirectional. Testing this hypothesis was challenging because high frequency firing of the larger-spiked “A” neuron often occludes spike activity of the “B” neuron and thus hampers the observation of A-to-B lateral excitation. To overcome this obstacle, we used antennal calcium imaging to detect the lateral excitation of the small-spiked ORNs. We generated transgenic flies that express GCaMP6m (Chen et al., 2013) in small-spiked ab1C neurons. Strong activation of the large-spiked ab1A and ab1B neurons excites ab1C (Figure 5.2A). Lateral excitation of ab1C was not affected in mutant flies lacking the odorant receptor (Gr63a) of ab1C (Figure 5.2B), indicating that the excitation is not caused by direct activation of the receptor. If lateral excitation of ab1C depends on the activation ab1A and ab1B, then it should be abolished in an Orco mutant, which lacks a co-receptor required for the response of ab1A and ab1B, but not ab1C (Larsson et al., 2004). As expected, silencing the activity of ab1A and ab1B ORNs abolished the ab1C excitation (Figure 5.2C). Taken together, our results support the notion that lateral excitation is indeed bidirectional.

Lateral excitation in a sensillum modulates behavior

For many insect species, the strongest behavioral attraction to pheromones is not elicited by the attractive components alone, but rather by the cognate pheromone blends, which contain mainly attractive compounds and a low concentration of antagonistic compounds that activate neighboring ORNs in the same sensillum (Connell, 1985; Cossé et al., 1998; Kaissling, 1996; Kaissling et al., 1978; Nikonov and Leal, 2002). The question arises: why does weak activation of the aversive ORN enhance the behavioral attraction towards the pheromone blend? Lateral excitation in a sensillum may offer an explanation for this longstanding paradox.

Curiously, a survey of the literature suggests that in general, large-spiked ORNs mediate attraction while the small-spiked neighbor mediates opposing behavior (see Chapter 1; Chen et al., unpublished data). This type of neuronal arrangement may represent a common organizing principle for many ORNs across insect species. Given that strong activation of the larger-spiked ORNs significantly excites its smaller-spiked neighbor in *Drosophila* (Figure 5.2), we hypothesize that lateral excitation of the adjacent antagonistic circuit may reduce the impact of activating the attractive, larger-spiked ORNs.

We tested this hypothesis by examining the ab1A/B-ab1C ORN pair as the valence of their behavioral outputs have been characterized (Faucher et al., 2006, 2013; Semmelback and Wang, 2009; Suh et al., 2004). Due to lateral excitation, strong activation of ab1A and ab1B by high concentrations of apple cider vinegar could activate the ab1C aversive circuit. As a result, this lateral excitation could reduce the overall attractiveness of apple cider vinegar at high concentrations (Figure 5.3). Similar to the report in a previous study (Suh et al., 2004), we observed robust aversion to carbon dioxide even at a low concentration (0.07%; Figure 5.3C). This confirms that weak activation of ab1C ORN is sufficient to elicit strong aversive behavior in flies (Suh et al., 2004). Therefore, we reasoned that silencing the ab1C synapse with tetanus toxin (TNT, Figure 5.3B) should abolish the behavioral effects of ab1C lateral excitation and enhance the flies' attraction to high concentrations of apple cider vinegar. In our preliminary T-maze assay, we found that using TNT to block synaptic transmission of ab1C indeed enhanced the behavioral attraction to a high concentration of apple cider vinegar, compared to the responses of the control flies. (Figure 5.3C). Together, our results provide evidence that lateral excitation in a sensillum can modulate behavior and that lateral excitation could offer an explanation to the low effectiveness of pure pheromone compounds.

Future directions

Characterize the bi-directionality and generality of lateral excitation

One should extend this study to other ORNs and sensillum types in order to determine the generality and bi-directionality of lateral excitation. B-to-A lateral excitation can be determined by single sensillum recording. Excitation in the A-to-B direction can be examined using calcium imaging, as described above. In order to better understand the precise relationship between the activity of the large-spiked ORNs and the calcium response in the passively activated small-spiked ORNs, one can also perform simultaneous calcium imaging and single sensillum recording (see Figure 5.4 for an example of the simultaneous recording in an ab1 sensillum).

Determine the impact of lateral excitation on odor-guided behavior

One is encouraged to continue the investigation of the impact of lateral excitation on behavior. One could start by following up on our preliminary experiments in the ab1A/B-ab1C ORN pair (Figure 5.3). To verify that the enhanced attraction indeed resulted from ab1C synaptic silencing, one could perform experiments with the following fly lines and conditions. It is important to use flies that are backcrossed to the same genetic background to ensure fair comparison between the different genotypes.

1) *UAS-TNT/+* or *Gr21a-Gal4/+ or Or42b mutant, Gr21a-GAL4 or Or92b mutant, UAS-TNT* (controls)*;*

2) *Gr63a mutant* (ab1C olfactory receptor mutant);

3) *Gr21a-Gal4, UAS-TNT* (ab1C synaptic silencing);

4) *Or42b mutant, Gr21a-GAL4; Or92b mutant, UAS-TNT* (ab1C synaptic silencing in ab1A&B receptors mutant background)

The results from our preliminary T-maze assay showed that apple cider vinegar at a high concentration was not attractive to the control flies, but the attraction was markedly enhanced in the ab1C>TNT flies (line #3, Figure 5.3). We reason that this enhanced attraction observed in the ab1C>TNT flies would remain unchanged in Gr63a mutant flies (line #3) as ab1C ORNs do not directly respond to apple cider vinegar, while the attraction will be abolished in the Or42b and Or92b mutant background where ab1A and ab1B are not functional (line #4).

In addition, we reason that silencing the ab1C synapse should not affect the flies' attraction to odorants not detected by ab1A and ab1B. Therefore, one could perform the T-maze experiments proposed above with another attractive odorant that specifically activate ac1A, ammonia (Min et al., 2013). If our hypothesis is correct, silencing the ab1C ORNs would not affect the animals' attraction to ammonia.

In a reciprocal experiment, one could silence synaptic transmission from ab1A and ab1B ORNs (*Orco-Gal4, UAS-TNT)*. In this case, the ab1A and ab1B neurons will still be able to respond to apple cider vinegar and elicit lateral excitation in ab1C, but would be prevented from activating the downstream attraction circuits in the brain. Therefore, we expect that these flies would reveal the isolated effects of lateral excitation of the ab1C aversion circuit and avoid high concentrations of apple cider vinegar.

Together, these experiments would help one to understand why a pure attractive odorant is sometimes not as appealing as a blend of odorants that contains both attractive and aversive compounds which act on grouped ORNs (Connell, 1985; Faucher et al., 2013; Kaissling, 1996; Linn et al., 2986; Nikonov and Leal, 2002).

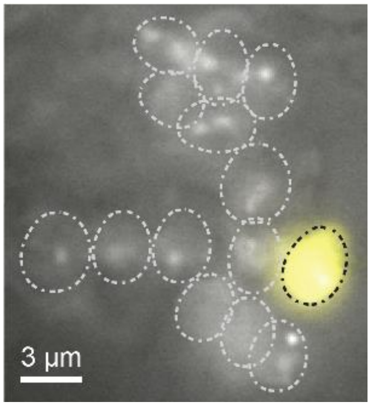

Figure 5.1. ORNs are not coupled with one another via gap junctions. Dye-fill experiment. One ORN was filled with Lucifer yellow. No dye transfer was observed between ORNs 20 min after dye filling (n=3). ORNs were identified (dash line) based on RFP labeling (*Orco>RFP*).

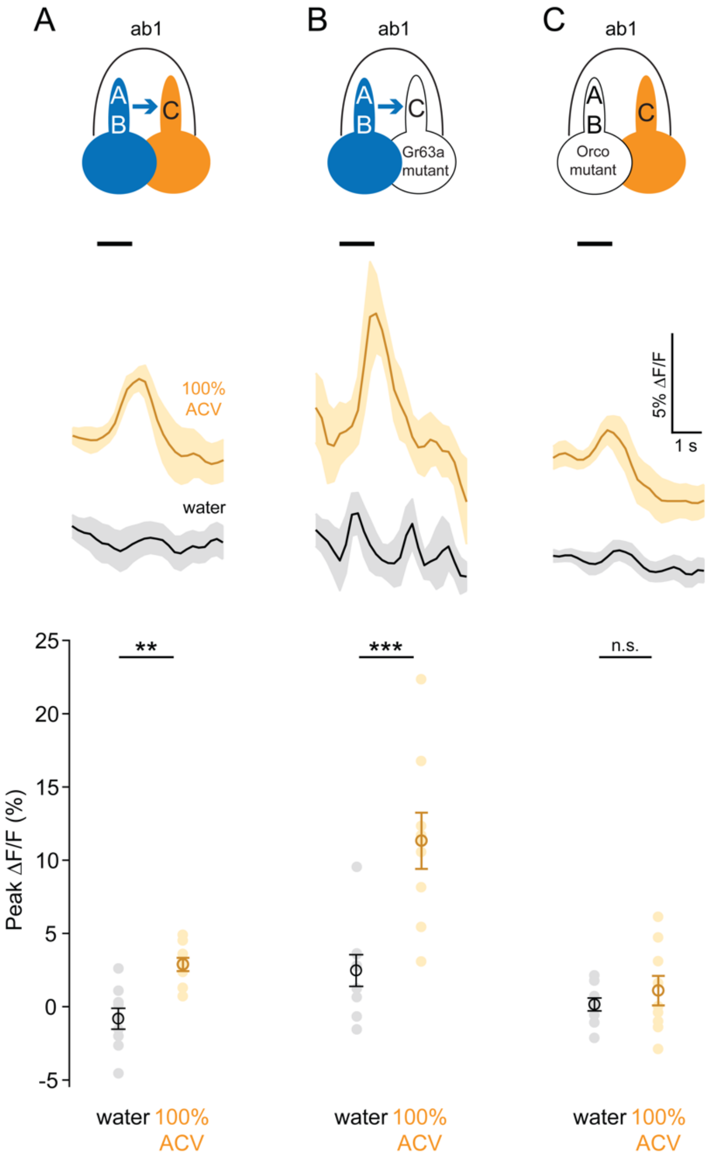

Figure 5.2. Lateral excitation of a small-spike ORN due to the activation of its large-spike neighbor. (A) Strong activation of ab1A and ab1B elicits a calcium response in ab1C. (B) Removing the odorant receptor (Gr63a) of ab1C did not abolish the lateral excitation. (C) Lateral excitation of ab1C is absent when ab1A and ab1B are silenced in Orco mutant. Middle panel: solid lines represent the mean responses and the shaded areas represent s.e.m.. The black bars indicate the period of odor stimulation. Bottom panel plots the mean ± s.e.m. of the calcium responses. n=9, parallel experiments. $^{**}p<0.01$; $^{***}p<0.001$; water vs. 100% ACV in the Orco mutant, $p=0.231$, *t* test.

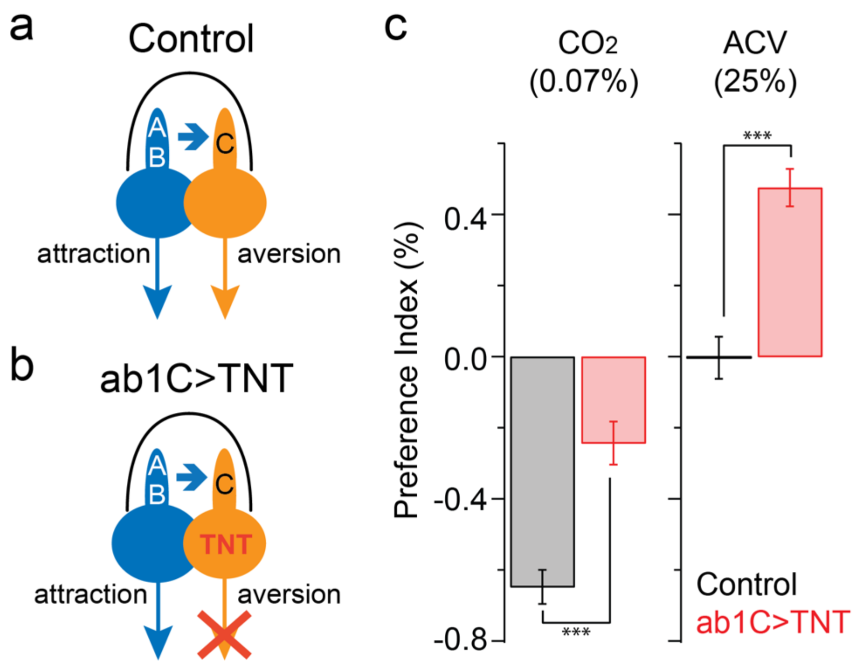

Figure 5.3. Lateral excitation modulates behavior. (A) ab1A and ab1B mediate attraction to apple cider vinegar (ACV); ab1C mediates aversion to CO_2. (B) Blocking ab1C synaptic transmission by tetanus toxin (TNT). (C) Transgenic flies expressing TNT in the ab1C ORNs hardly avoided CO_2 (left) and exhibited markedly stronger attraction to vinegar. *** $p<0.001$, *t*-test, n=9-10, parallel experiments.

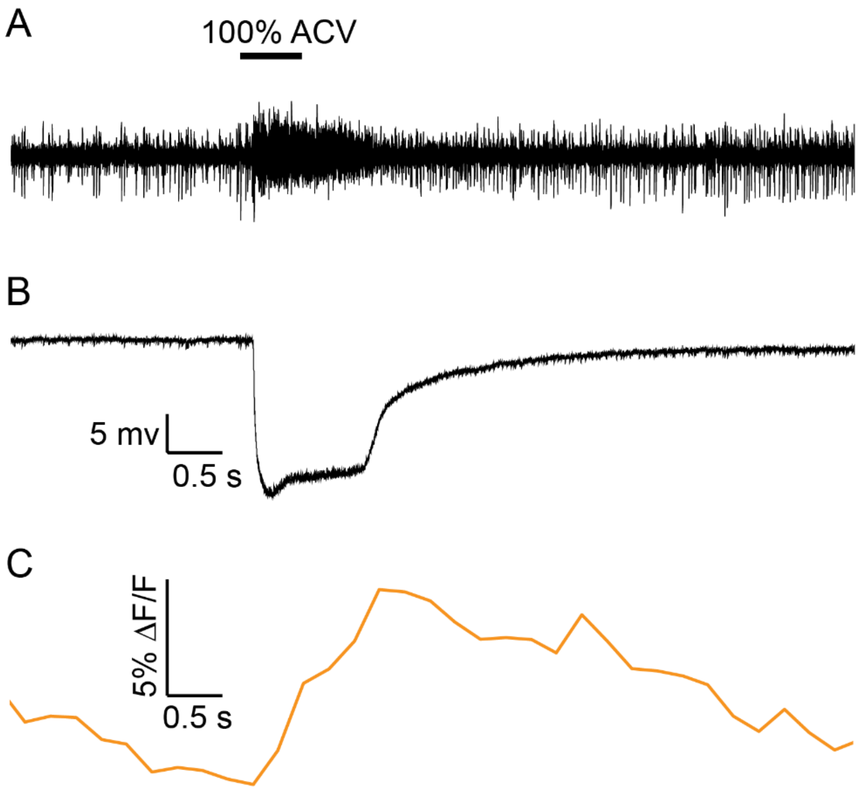

Figure 5.4 Simultaneous calcium imaging and single sensillum recording in an ab1 sensillum. (A) The spike, (B) the local field potential, and (C) the ab1C ORN calclium responses were simultaneously recorded in an ab1 sensillum of a Gr21a>GCaMP6m fly. The black bar at the top of panel (A) indicates the stimulus (100% apple cider vinegar (ACV)) time point and duration and it applies to all three panels.

References

Bohrmann, J., Haas-Assenbaum, A., (1993). Gap junctions in ovarian follicles of Drosophila melanogaster: inhibition and promotion of dye-coupling between oocyte and follicle cells. Cell Tissue Res. *273*, 163-173.

Chen, T.-W., Wardill, T.J., Sun, Y., Pulver, S.R., Renninger, S.L., Baohan, A., Schreiter, E.R., Kerr, R. a, Orger, M.B., Jayaraman, V., et al. (2013). Ultrasensitive fluorescent proteins for imaging neuronal activity. Nature *499*, 295–300.

Connell, R.J.O. (1985). Responses to pheromone blends in insect olfactory receptor neurons. J. Comp. Physiol. A *156*, 747–761.

Cossé, a. a., Todd, J.L., Baker, T.C. (1998). Neurons discovered in male Helicoverpa zea antennae that correlate with pheromone-mediated attraction and interspecific antagonism. J. Comp. Physiol. - A Sensory, Neural, Behav. Physiol. *182*, 585–594.

Faucher, C., Forstreuter, M., Hilker, M., de Bruyne, M. (2006). Behavioral responses of Drosophila to biogenic levels of carbon dioxide depend on life-stage, sex and olfactory context. J. Exp. Biol. *209*, 2739–2748.

Faucher, C.P., Hilker, M., de Bruyne, M. (2013). Interactions of carbon dioxide and food odours in Drosophila: Olfactory hedonics and sensory neuron properties. PLoS One *8*, e56361.

Kaissling, K. (1996). Peripheral mechanisms of pheromone reception in Moths. Chem. Senses *21*, 257–268.

Kaissling, K.E., Kasang, G., Bestmann, H.J., Stransky, W., Vostrowsky, O. (1978). A new pheromone of the silkworm moth Bombyx mori - Sensory pathway and behavioral effect. Naturwissenschaften *65*, 382–384.

Larsson, M.C., Domingos, A.I., Jones, W.D., Chiappe, M.E., Amrein, H., Vosshall, L.B. (2004). Or83b encodes a broadly expressed odorant receptor essential for Drosophila olfaction. Neuron *43*, 703–714.

Linn, C.E., Campbell, M.G., Roelofs, W.L. (1986). Male moth sensitivity to multicomponent pheromones: Critical role of female-released blend in determining the functional role of components and active space of the pheromone. J. Chem. Ecol. *12*, 659–668.

Min, S., Ai, M., Shin, S. a, Suh, G.S.B. (2013). Dedicated olfactory neurons mediating attraction behavior to ammonia and amines in Drosophila. Proc. Natl. Acad. Sci. *110*, E1321-9.

Nikonov, A. a, Leal, W.S. (2002). Peripheral coding of sex pheromone and a behavioral antagonist in the Japanese beetle, Popillia japonica. J. Chem. Ecol. *28*, 1075–1089.

Phelan, P., Nakagawa, M., Wilkin, M.B., Moffat, K.G., O'Kane, C.J., Davies, J.A., Bacon, J.P. (1996). Mutations in shaking-B prevent electrical synapse formation in the Drosophila giant fiber system. J. Neurosci. *16*, 1101–1113.

Ramón, F., Moore, J.W. (1978). Ephaptic transmission in squid giant axons. Am. J. Physiol. *234*, C162–C169.

Semmelhack, J.L., Wang, J.W. (2009). Select Drosophila glomeruli mediate innate olfactory attraction and aversion. Nature *459*, 218–223.

Shanbhag, S.R., Müller, B., Steinbrecht, R.A. (1999). Atlas of olfactory organs of Drosophila melanogaster 1. Types, external organization, innervation and distribution of olfactory sensilla. Int. J. Insect Morphol. Embryol. *28*, 377–397.

Shanbhag, S.R., Müller, B., Steinbrecht, R.A. (2000). Atlas of olfactory organs of Drosophila melanogaster 2. Internal organization and cellular architecture of olfactory sensilla. Arthropod Struct. Dev. *29*, 211–229.

Su, C.-Y., Menuz, K., Reisert, J., Carlson, J.R. (2012). Non-synaptic inhibition between grouped neurons in an olfactory circuit. Nature *492*, 66–71.

Suh, G.S.B., Wong, A.M., Hergarden, A.C., Wang, J.W., Simon, A.F., Benzer, S., Axel, R., Anderson, D.J. (2004). A single population of olfactory sensory neurons mediates an innate avoidance behaviour in Drosophila. Nature *431*, 854–859.